Title
Li Oxide Deposit Formation and Impacts in Non-aqueous Li-air Battery

Permalink
https://escholarship.org/uc/item/7jm6n74c

Author
Yuan, Hao

Publication Date
2018

Peer reviewed|Thesis/dissertation

UNIVERSITY OF CALIFORNIA,
IRVINE

Li Oxide Deposit Formation and Impacts in Non-aqueous Li-air Battery

DISSERTATION

submitted in partial satisfaction of the requirements
for the degree of

DOCTOR OF PHILOSOPHY

in Mechanical and Aerospace Engineering

by

Hao Yuan

Dissertation Committee:
Professor Yun Wang, Chair
Professor Feng Liu
Associate Professor Manuel Gamero-Castaño

2018

DEDICATION

To my parents and friends, who encouraged me to pursue my dreams and finish my dissertation.

TABLE OF CONTENTS

Page

LIST OF FIGURES v
LIST OF TABLES vii
NOMECLATURE viii
ACKNOWLEDGMENTS x
CURRICULUM VITAE xi
ABSTRACT OF THE DISSERTATION xiii
CHAPTER 1: Introduction 1
  1.1 Motivation and Background 1
  1.2 Structure of The Thesis 7
Chapter 2: Discharge Oxide Storage Capacity and Voltage Loss Modeling 9
  2.1 Introduction 9
  2.2 The Damköhler Number 13
  2.3 Oxygen Transport 19
  2.4 Surface Coverage Mode 24
  2.5 Discharge Voltage Loss 26
  2.6 Charge Capacity 40
  2.7 Energy Capacity 44
  2.8 Summary 46
Chapter 3: Surface Coverage Model: Experimental Validation 48
  3.1 Introduction 48
  3.2 Experimental 50
  3.3 Film-Resistor Model 53
  3.4 Surface Coverage Model 55
  3.5 Comparison of Model Prediction and Experiment Data 57
  3.6 Summary 67
Chapter 4: Spatial Variations of Discharge Oxides 69
  4.1 Introduction 69
  4.2 Experimental 72
  4.3 Analysis of Spatial Variation 75
  4.4 Morphology of Li Oxides 76
  4.5 Model Prediction and Experimental Validation 80

4.6 Summary 83
Chapter 5: Conclusions and Future Works 84
5.1 Conclusion.. 84
5.2 Future work 86
BLIOGRAPHY.. 88

LIST OF FIGURES

Page

Figure 1: The gravimetric energy densities (Wh/kg) for various types of rechargeable batteries compared to gasoline. (Girishkumar et al., 2010)........ 2

Figure 2: Schematic of a Li-air and its discharging operation with Li_2O_2 as an example of discharge product. (Yuan & Wang, 2015)........ 4

Figure 3: Oxygen profiles in an air cathode under different Da and β........ 22

Figure 4: Oxygen profile in an air cathode under β=0.5 and two levels of the Li oxide volume fraction........ 23

Figure 5: Typical growth modes of the oxide precipitate film in air cathodes: a.) the inward cylindrical-film growth mode; b.) the outward spherical-film growth mode; c.) the planar-film growth mode; d.) the outward cylindrical-film mode; e.) the inward spherical-film mode; f.) the SEM image of precipitate on highly ordered pyrolytic graphite (HOPG) at 10 $\mu A/cm2$ for 1M LiTriflate in DOL:DME (1:1 w/w)........ 25

Figure 6: Comparison of the model prediction with experimental data (Zhang & Read, 2011). (Wang et al., 2015)........ 29

Figure 7: Comparison of the model prediction with experimental data (Sahapatsombut et al., 2014). (Wang et al., 2015)........ 29

Figure 8: Comparison of the predicted voltage with the experimental data (Albertus el al., 2011). The experiment was operated on Li-air battery using a PVDF/super P/NMP air cathode........ 31

Figure 9: $\Delta\eta a$ and $\Delta\eta d$ as a function of the precipitate volume fraction for the current densities in the validation of Figure 8. ηa arises from electrode passivation and surface reduction. Δηd is caused by oxygen transport clogging........ 32

Figure 10: Comparison of $smax$ from Eq. [34], $smax, a$ from Eq. [35], and $smax, d$ from Eq. [36] as a function of the surface coverage factor. Regime #1 is defined for $smax, a \geq smax, d$. Regime #2 is defined for $smax, d > smax, a$. The maximum error is 6.88%........ 34

Figure 11: Comparison of $smax$, $smax, a$, and $smax, d$ under τd of 2.5. Regime #1 is defined for $smax, a \geq smax, d$. Regime #2 is defined for $smax, d > smax, a$. The maximum error is 7.63%........ 35

Figure 12: $smax$ as a function of τa under β of 0.5, τd of 1.5, $V0$ of 2.75 V and $Vcut$ of 2.0 V........ 37

Figure 13: $smax$ as a function of τd under β of 0.5, τa of 2.5, $V0$ of 2.75 V and $Vcut$ of 2.0 V........ 38

Figure 14: $smax$ as a function of Da under β of 0.5, τd of 1.5, τa of 2.5, $V0$ of 2.75 V and $Vcut$ of 2.0 V........ 40

Figure 15: Comparison between the predicted and experimental capacities. Battery information are listed in Table 6........ 42

Figure 16: Comparison between the predicted and experimental capacities. The details of the cells are shown in Table 7........ 43

Figure 17: Two energy losses as a function of s in Eq. [48] in the validation of Figure 8. The solid line represents $u0$ as a reference. The ua arises from electrode passivation and surface reduction. Δud is caused by oxygen transport clogging........ 45

Figure 18: (a) Carbon cloth cathode; (b) Fiber morphology; and (c) Experimental setup for the Li-air battery. (Wang et al., 2017) 51
Figure 19: Thin film growth mode of precipitates on: 1.) cylindrical fiber; and 2.) planar surface 54
Figure 20: Discharge voltage evolution of Li-air battery and comparison with model predictions. The film-resistor model's prediction considerably deviates from the experimental data under the two low currents, which is not plotted in the figure 58
Figure 21: Numerically Predicted $\Delta\eta O2$ in Eq. [57] for the three current densities. 59
Figure 22: SEM images and XRD analysis of the cathode with discharge precipitate under 0.03 $mA/cm2$ 60
Figure 23: Film formation of discharge precipitate under 0.03 $mA/cm2$.......... 61
Figure 24: Large aggregate formation of discharge precipitate under 0.03 $mA/cm2$ 62
Figure 25: Small aggregate formation of discharge precipitate under 0.03 $mA/cm2$ 63
Figure 26: Film and toroid formation of discharge precipitate under 0.06 $mA/cm2$ 66
Figure 27: Film formation of discharge precipitate under 0.1 $mA/cm2$.......... 67
Figure 28: (a) Carbon cloth cathode, (b) three-layered cathode, (c) experimental setup for the Li-air battery, and (d) the discharge voltage under 0.01 $mA/cm2$. 73
Figure 29: SEM images of precipitates at the layer 1 surface on the air side. 77
Figure 30: SEM images of the thin film of precipitates at the fiber surface at the layer 1 surface on the air side. 78
Figure 31: SEM images of the precipitates at the layer 1-2 interface. 79
Figure 32: SEM images of the precipitates at the layer 3-separator interface. 79
Figure 33: Spatial variation of the oxygen content predicted by Eq. [58] in (a). Compare Eq. [59] with the exact solution. 81
Figure 34: Spatial variation of the local reaction rate predicted by Eq.[62] with β=0 in (a) and β=0.5 in (b). The exact solution is also shown in (b). 81
Figure 35: Spatial variation of reaction rate: comparison between experimental data and model prediction for $\beta = 0$.......... 82
Figure 36: Spatial variation of reaction rate: comparison between experimental data and model prediction for $\beta = 0.5$.......... 82

LIST OF TABLES

Page

Table 1. Ionic conductivity for various electrolytes. (Wang & Cho, 2013) 15
Table 2. Oxygen diffusivity in nonaqueous electrolytes. (Wang & Cho, 2015) 20
Table 3. Physical, electrochemical, and model parameters. 28
Table 4. Physical properties and model parameters. (Albertus el al., 2011; Yuan & Wang, 2015) 30
Table 5. MacMullin number (NM) of a system consisting of a dispersed non-conducting phase in a conductive medium. (Wang et al., 2013; Martínez et al., 2009)... 38
Table 6. Battery cell information. (Mirzaeian & Hall, 2009; Ren et al., 2011; Younesi et al., 2011) 41
Table 7. Battery cell information. 42
Table 8. Experimental and modeling parameters. 52

NOMECLATURE

a	factor of effective catalyst area per unit volume when oxide precipitate is present
a_o	factor of catalyst surface area factor per unit volume
C	molar concentration of species k, mol/m^3
D	species diffusivity, m^2/s
Da	Damköhler number
F	Faraday’s constant, 96,487 C/mol
I	current density, A/cm^2
i	superficial current density, A/cm^2
j	transfer current density, A/cm^3
M	molecular weight, kg/mol
Q	charge capacity, C/m^2
R	universal gas constant, 8.134 $J/mol \cdot K$; Ohmic resistance, $m\Omega \cdot cm^2$
r_c	dimension of carbon particle
s	volume fraction of insoluble product
t	time, s
T	temperature, K
u_x	velocity, m/s
u	energy capacity per area, J/m^2
V	Voltage, V

Greek

α	overpotential ratio
β	transfer coefficient

ρ	density, kg/m^3
ϕ	phase potential, V
κ	ionic conductivity, S/m
ε	porosity or volume fraction
η	surface overpotential, V
τ	tortuosity/coverage coefficient
δ	thickness, m

Superscripts and Subscripts

a	surface coverage
c	cathode
d	diffusion
e	electrolyte
eff	effective value
o	reference value; initial value

ACKNOWLEDGMENTS

Firstly, I would like to express my sincere gratitude to my advisor Prof. Yun Wang for the continuous support of my Ph.D. study and related research, for his patience, motivation, and immense knowledge. His guidance helped me in all the time of research and writing of this thesis. I could not have imagined having a better advisor and mentor for my Ph.D. study.

Besides my advisor, I would like to thank the rest of my thesis committee: Professor Feng Liu and Associate Professor Manuel Gamero-Castaño for their insightful comments and encouragement, but also for the hard question which incented me to widen my research from various perspectives.

I thank my labmates for the stimulating discussions, for the sleepless nights we were working together before deadlines, and for all the fun we have had in these years.

Last but not the least, I would like to thank my parents for supporting me spiritually throughout writing this thesis and my life in general.

Financial support was provided by the University of California, Irvine, the National Science Foundation (CBET-1336873) on this study.

CURRICULUM VITAE

Hao Yuan

Education

2018	Doctor of Philosophy in Mechanical and Aerospace, University of California, Irvine Irvine, CA, U.S.
2014	M.S. Mechanical Engineering, University of Southern California Los Angeles, CA, U.S.
2012	Bachelor of Engineering, Beihang University Beijing, China

Publication

"Analysis of Li-Air Battery: Voltage Loss due to Insoluble Discharge Formation"
H. Yuan and Y. Wang
Paper No. FUELCELL2015-49434, pp. V001T02A004; 5 pages

"Discharge Oxide Storage Capacity and Voltage Loss In Li-Air Battery"
Y. Wang, Z. Wang, H. Yuan, and T. Li
Electrochimica Acta 180 (2015) 382–393

"Experimental and computational investigation of confined laser-induced breakdown spectroscopy"
Y. Wang, H. Yuan, Y. Fu, and Z. Wang
Spectrochimica Acta Part B 126 (2016) 44–52

"Discharge Precipitate's Impact in Li-Air Battery: Comparison of Experiment and Model Predictions"
Y. Wang and H. Yuan
Journal of The Electrochemical Society, 164 (9) A2283-A2289 (2017)

Papers are prepared but not published yet:

H. Yuan, Y. Wang, and J. Read, "Voltage and Capacity Loss of Li-Air Battery due to Insoluble Product Formation", Applied Energy, under review.

H. Yuan, B. Seo, and Y. Wang, "Spatial Variations of Reaction Rate and Discharge Precipitate in Li-air Batteries", Journal of The Electrochemical Society, to be submitted.

B. Seo, H. Yuan, and Y. Wang, “Dual-layer Cathode Design for Li-air Batteries”, in preparation.

ABSTRACT OF THE DISSERTATION

Li Oxide Deposit Formation and Impacts in Non-aqueous Li-air Battery

By

Hao Yuan

Doctor of Philosophy in Mechanical and Aerospace Engineering

University of California, Irvine, 2018

Professor Yun Wang, Chair

Lithium oxygen battery has the potential to outdo the best battery system on the market due to its high theoretical specific energy of 11,400 Wh/kg (Li) which is comparable to that of gasolines. However, their practical implementation is still facing challenges, including low cyclic performance, high charging voltage, insoluble discharge product formation, and electrolyte degradation. Air cathodes, where oxygen reacts with Li ions and electrons to produce insoluble discharge oxides, are often considered as the most challenging component in nonaqueous Li-air batteries. To understand the voltage loss mechanisms in air cathodes due to insoluble discharge oxides, a mathematical model is developed, which incorporates the major thermodynamic, transport, and kinetic processes, and comprehensive analysis is conducted. Experiment is also designed and conducted for the model formulation and validation. Li battery components were fabricated, then assembled in an argon filled glove box. Electrochemical testing was conducted on the experimental Li air battery by using the PARSTAT MC Multichannel Potentiostat. An X-ray Diffraction, scanning electron microscope, and high-precision mass scale were employed to determine the composition, morphology, and spatial variation of Li oxide products. Through the model analysis, it is found that the electric passivation and oxygen transport blockage caused by the Li oxides precipitates reduce the battery voltage and energy capacity. The first stage of voltage drop is dominated by the electrode passivation and surface loss, while the latter stage of voltage drop is dominated by the oxygen blockage. In addition, several morphologies of oxides are identified in the cathode structure under various current densities, thus the proposed surface coverage model is superior to the traditional film-resistor approach. Further, it is found there exists spatial variations in discharge Li oxides in terms of mass and morphology, and experimental data show a good agreement with the theoretical analysis in term of the spatial variation of the Li oxides mass. The Da number is identified as a major parameter governing the spatial variation.

CHAPTER 1: Introduction

1.1 Motivation and Background

For the modern society, the demand for energy is huge, and is increasing continuously. The International Energy Agency (IEA) report (2014) showed that mankind's total energy consumption was 13,371 Mtoe, around 156 PWh, for the year of 2012. And it was predicted that the total consumption would be roughly increased to 17,500 Mtoe, around 204 PWh, in the year of 2035. In 2012, the fossil fuel, such as oil, coal and natural gas, represent 81% of the world's total primary energy source. They account for 99.5% of the total CO_2 emission, 31,734 Mt, which is one of the greenhouse gases that allows radiative forcing and contributes to global warming.

To fight against the fossil fuels' depletion and emission problem, various renewable resources, such as biomass, wind, solar, geothermal, and hydroelectric energy have been developed. However, their power production intrinsically depends on weather and location, so they are always combined with the grid energy storage system to improve their performance. Numerous energy storage methods including mechanical, chemical, thermal and magnetic ways have been explored and developed. Compared with other methods, electrochemical batteries are one of the best choices for electrical energy storage, which are extensively used to power today's mobile world (Gao & Yang, 2010). Electrochemical batteries are considered to be efficient, simple, and reliable. They convert electrical energy directly into chemical energy by reversible electrochemical oxidation–reduction reactions energy and vice versa. In addition, portable electronic equipment and devices (Lee et al. 2011) have been developing at a rapid pace, and this progress demands ever-increasing energy and power density in power sources. Although dominating the consumer electronics markets for popular portable devices, the common lithium batteries are facing challenges in sustainable electrified road transport. (Jung et al., 2012) The development of advanced, high-energy lithium batteries is essential in the rapid establishment of the electric car market. Figure 1 shows the gravimetric energy densities (Wh/kg) for different types of rechargeable batteries compared to gasoline (Girishkumar et al. ,2010). Owing to its exceptionally high energy potentiality which provides over 5 times durations of equal mass Li-ion battery, the lithium–air battery can be a promising candidate for fulfilling this role. In addition, another major advantage of the Li-air battery is its high specific energy, which measures the amount of energy storage capability per unit weight. Theoretically, the oxidation of 1 kg lithium metal releases 11,680 Wh/kg rivaling that of gasoline (Girishkumar et al., 2010).

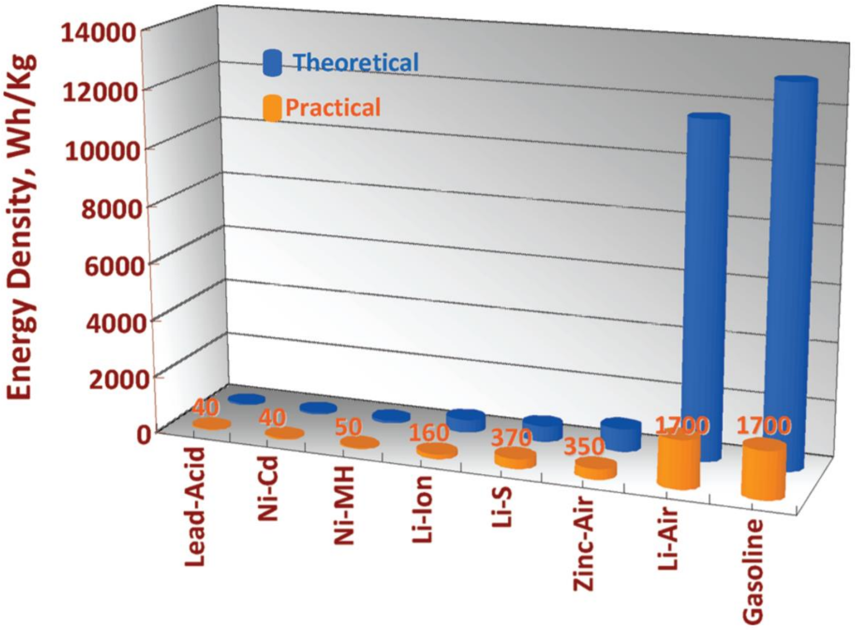

Figure 1: The gravimetric energy densities (Wh/kg) for various types of rechargeable batteries compared to gasoline. (Girishkumar et al., 2010)

Typically, the Li-air battery are divided into two types according to the electrolyte: an aqueous electrolyte and an organic electrolyte, naming non-aqueous. Compared with the aqueous battery, the non-aqueous battery has been proved that the reduction products can be reversed into the original reagents and is advantageous for the technology offering potentials of rechargeability, comparatively long cycling life, and high energy efficiency (Wen et al., 2015). Moreover, the theoretical energy density of a non-aqueous Li-air battery system is higher than that of an aqueous Li-air battery system because of the water or acid being involved in the reactions in the aqueous system (Liu et al., 2015). Due to the above benefits, we will focus on non-aqueous battery in this work.

Ideally, Li-air battery works until exhausting oxygen or metal Li. In practice, its capacity is much less than the theoretical value. A major limitation arises from the air cathode, where insoluble discharge products, such as lithium oxide and lithium peroxide, accumulate at the reaction site in the porous structure. The deposit will eventually shut down discharge operation because of electrode passivation and oxygen transport polarization (Wang & Cho, 2013). To simplify analysis, the specific capacity of Li-air batteries is mostly expressed on the base of carbon weight rather than that of Li metal.

Figure 2 shows the schematic of a Li-air battery and its operation. A Li–air battery is composed of a Li metal anode, an air electrode, and a separator soaked in lithium-ion-conducting electrolyte. During the operation, Li ions and electrons are produced in the anode as Li is oxidized during discharge. The lithium ions migrate via the electrolyte to the cathode, where they combine with oxygen and electrons to form Li oxide compounds, i.e. Li peroxide. Electric work is produced when electrons travel through external circuit. In an inverse operation, i.e. charging, where external potential applies to Li-air battery, Li ions will be plated in the anode and oxygen will be generated in the cathode.

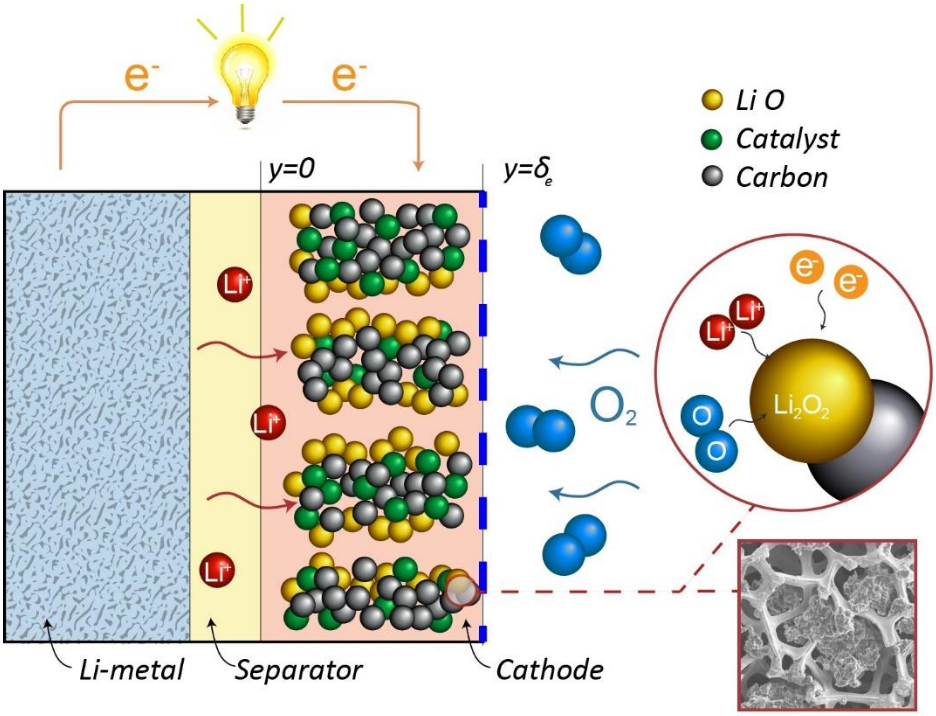

Figure 2: Schematic of a Li-air and its discharging operation with Li_2O_2 as an example of discharge product. (Yuan & Wang, 2015)

In air cathodes, the pore networks provide path ways for transporting Li ions and oxygen through electrolyte, while the carbon structure conducts electrons. At the reaction surface where all the reactants are accessible, Li oxide composites, such as Li peroxide and Li oxide, are produced as discharge product, which are usually insoluble in non-aqueous electrolyte, thus their presence block the pathway for reactive species (Li ion and oxygen) (Cheng & Chen, 2012). Li oxide composites are generally low in electrical conductivity, thus their coverage over the reaction surface limits electron access to the reaction surface, causing electrode passivation. The above effects arising from Li oxide deposit will eventually prevent any cathode reaction activity even when excess Li and external oxygen are available, and thus will shorten the cell discharging capability. It can be seen that the energy storage capacity of Li–air batteries is strongly limited by the air cathode, which is one of the most important components in a Li–air battery.

In modeling and analysis, Yuan et al. (2015) discussed multiphase phenomena, solid product generation, and morphology growth in Li-air battery's cathodes. They developed multi-dimensional model with phase change to study significant volume changes in the Li metal anode and within the porous cathode. They indicated that it was necessary to take account of microscopic surface passivation and pore clogging simultaneously in the continuum models for clarifying the effects on the transfer phenomena and even the sudden death phenomenon. Yoo et al. (2014) developed a mathematical model to study the volume change in Li-air battery. Their numerical study showed how the effective reaction area as well as the volume available for electrolyte changes during operation and indicated that the cell voltage cannot be maintained constant because of reduction of effective reaction area. Viswanathan et al. (2011) investigated the electrical conductivity in Li_2O_2 by theoretical analysis and experiment. They pointed out that the sudden death is related to a critical thickness of Li peroxide deposit. Sahapatsombut et al. (2014) and Sandhu et al. (2007) showed that the low solubility and diffusivity of oxygen would reduce the oxygen concentration at the reaction sites, limiting the Li-air batteries power density. Wang et al. (2013) emphasized on the discussion of the nanomaterial and its practical implementation. For cathode, they implied that specific surface area, conductivity, chemical and electrochemical stability under operating process, and reactivity with electrolytes are all important design factors. Williford et al. (2009) showed that a dual-pore system could improve the battery performance through fully using the porous structure of the air cathode by simulation results. Some works indicated that internal ohmic loss, e.g. in the separator and solid electrolyte, would further reduce power density (Inaguma & Nakashima, 2013; Ghamouss et al., 2012; Puech et al., 2012). Chen et al. (2014) investigated the performance of Li-air batteries with carbon nanotube and carbon nanofiber cathodes. They found that the discharge capacity is mainly limited by the combination of oxygen diffusion and electrical resistance of the discharge precipitate at the reaction surface. A mathematical model for the discharge of Li-air batteries was also developed to describe the effects of the finite conductivity of the deposit layer in the cathode. Christensen et al. (2012) investigated the deposit product resistivity in the cathode and related it to the ohmic loss. Nemanick (2014) investigated the electrochemistry of non-aqueous Li-oxygen batteries on both reduction and oxidation using carbon black and single-walled nanotube (SWNT) microcavity electrodes, showing that the oxygen reduction reaction (ORR) produces two electrochemically distinct Li_2O_2 species that can be differentiated by their behavior on charge. They pointed out controlling the ratio of Li_2O_2 species can effectively reduce the overpotential on charge transfer. Yuasa et al. (2013) investigated the discharge/charge performance of Li-air batteries using the carbon-supported $LaMn_{0.6}Fe_{0.4}O_3$ nanoparticle as the cathode catalyst. They revealed that oxygen diffusion into the air electrode strongly affects to the discharge capacity of Li-air cells. Andrei et al. (2010) proposed a physics-based model for Li-air batteries, showing the specific capacity is mainly limited by the oxygen diffusion length. They also discussed various approaches to increase the specific capacity and the energy density of Li-air batteries.

Despite the above efforts in Li-air battery modeling, a complete model to analyze, design and optimize the battery is lacked at current stage. Most of them are exploring electrochemistry or simple models following the Li-ion battery formulation. In addition, the present electrode passivation submodel is questionable given different morphologies were observed by many studies. Theoretical analysis is absent at current. The fundamental numbers that govern the cathode performance such as the reaction spatial variation are unclear to a large degree. The motivation of this PhD dissertation research work is to address these issues, including 1.) experimental work to formulate a new surface coverage model for Li oxides' impact; 2.) theoretical analysis on the oxygen and reaction spatial variations; 3.) distinguishing the voltage losses from the electrode passivation and oxygen blockage; and 4.) an experimental study to validate the reaction spatial variation in the cathode.

1.2 Structure of The Thesis

The thesis consists of the below major chapters: Chapter 2 will present a modeling analysis on nonaqueous Li-air batteries to obtain theoretical solutions for the losses of the output voltage, discharge capacity, and energy capacity caused by insoluble precipitates. The two main voltage losses due to insoluble discharge precipitates, i.e. increased oxygen transport resistance and electrode passivation/surface loss, are distinguished and compared. Approximate solutions are obtained to estimate the discharge voltage, the maximum volume fraction of insoluble precipitates, charge capacity, and energy capacity. Chapter 3 will compare the predictions of two models, namely the film-resistor model and surface coverage model, with experimental data to study voltage loss and elucidate the precipitate morphology's impacts in Li-air battery discharge operation. Chapter 4 will present a study on the spatial variation of the local ORR reaction rate in the cathode in Li-air batteries both theoretically and experimentally. In experiment, the three-layer cathode was designed, and the morphology and mass of Li oxides were characterized using

SEM and a high-resolution scale, respectively. Chapter 5 will summarize the major results and make conclusions. The future works to continue the topic of study are recommended for the following researchers.

Chapter 2: Discharge Oxide Storage Capacity and Voltage Loss Modeling

This chapter presents an analysis of air cathodes where oxygen reacts with Li ions and electrons with discharge oxide stored in their pore structure. Air cathodes are often considered as the most challenging component in nonaqueous Li-air batteries. In non-aqueous electrolytes, discharge oxides are usually insoluble and hence precipitate at local reaction site, raising the oxygen transport resistance in the pore network. Due to their low electric conductivity, their presence causes electrode passivation. The objectives of this chapter are to investigate the air cathode's performance through analyzing oxygen transport, modeling electrode passivation, and evaluating the transport polarization raised by discharge oxide precipitate.

2.1 Introduction

Li-air batteries hold a great promise for high specific energy storage. Bruce et al. (2012) reported a theoretical value of 3,505 Wh/kg using non-aqueous electrolytes, which is comparable to those of direct methanol fuel cells (DMFC) (5,524 Wh/kg) and gasoline engine (11,860 Wh/kg). Figure 2 shows the schematic of a Li-air battery and its discharge operation. During discharge, lithium is oxidized in the anode to produce lithium ions and electrons: electrons are conducted via an external circuit to produce electric work, while lithium ions are transported across electrolyte to react with oxygen and electrons in the cathode. During charging, lithium metal is plated out in the anode, and O_2 is released in the cathode.

Air cathodes are often considered as the most challenging component in nonaqueous Lithium-air batteries. In cathodes, oxygen is reduced to produce Li composites during discharge, e.g. lithium oxides:

$$\begin{aligned} \mathrm{Li}^+ + \mathrm{e}^- + \mathrm{O}_2 + * &\rightarrow \mathrm{LiO}_2^* \\ \mathrm{Li}^+ + \mathrm{e}^- + \mathrm{LiO}_2^* &\rightarrow \mathrm{Li}_2\mathrm{O}_2^* \end{aligned} \qquad [1]$$

where "*" denotes a surface site on the reaction surface or oxides in which the growth proceeds. Air cathode contributes a major voltage loss because of the sluggish reaction kinetics and oxygen transport. In addition, oxide products are usually insoluble in non-aqueous electrolytes, causing pore-network clogging. Li oxide composites are low in electric conductivity, thus their presence on the reaction surface resists electron's access to reaction sites, causing electrode passivation. As discharging proceeds, oxide precipitate accumulates in the pore networks and on the reaction surface, increasing both oxygen and electron transport resistances, and consequently voltage loss.

The first non-aqueous rechargeable Li-air batteries were reported by Abraham and Jiang (1996). Since then, the technology has received a fast-growing interest of research to explore electrochemical reaction mechanisms, electrode structures, and electrolyte and catalyst materials (Gao et al., 2012; Laoire et al., 2009; Li et al., 2011; Debart et al., 2007; Lu et al., 2010; Lu et al., 2011). Mirzaeian and Hall (2009) studied the impacts of porosity, pore structure, morphology of carbon and surface area of carbon in air cathodes on the battery's specific capacity. Pore structure was adjusted by controlling the molar ratio of resorcinol to catalyst and the pyrolysis and activation temperatures. They found that the battery performance changes with the morphology of carbon, the pore volume, pore size, and surface area of carbon. Yang et al. (2009) used mesocellular carbon foam as the cathode. They fabricated carbon samples containing bimodal mesopores with a narrow pore size distribution through nanocasting technique; and showed the samples yielded about 40% capacity increase compared with commercial carbon black. Mitchell et al. (2011) used hollow carbon fibers of 30 nm diameters grown on ceramic porous substrate in air cathodes and achieved a high specific capacity under low carbon loading. They also indicated Li oxides grew as nodules on the fibers and developed into toroids during discharge. Griffith et al. (2015) observed Li oxides form typical 'toroidal' particles under low discharge rates and take needle-like shapes under the high rates, instead of the nano-sheets or compact films. They indicated Li_2O_2 grows by a locally mass-transfer-limited nucleation and growth mechanism. Xiao et al. (2010) investigated the effects of carbon microstructure and loading on battery performance. They found that the cathode capacity increased with the carbon source's mesopore volume, and that the pore size's uniformity played an important role in battery performance. Zhang et al. (2010) employed galvanostatic discharge, polarization, and AC-impedance techniques to study Li-air battery, showing that the discharge performance is determined mainly by air cathode, instead of Li anode. Viswanathan et al. (2011) employed a reversible redox couple to investigate the deposit film resistance and adopted a metal-insulator-metal charge transport model to predict the electrical conductivity of a Li_2O_2 film. They showed "sudden death" in the charge transport when the film thickness is around 5 to 10 nm.

In modeling and analysis, Franc and Xue (2013) discussed the carbon-based electrode models from the atomistic to continuum approaches, and briefly introduced a new theory to study the impact of the electrode's carbon structure on battery's cyclability. Andrei et al. (2010) discussed several approaches to improve the battery's energy density. They concluded that it is more efficient to use non-uniform catalyst, which enhances the reaction at the separator–cathode interface, than to use uniform catalyst. They also discussed energy density improvement through solvents with high oxygen solubility/diffusivity and partly wetted electrodes. Albertus et al. (2011) proposed a physics-based model accounting for oxide precipitates. They developed a film growth model over a spherical carbon particle; and proposed an electric resistance formula for the oxide film. Following the Li-ion battery approach, a 1-D Li-air battery model was developed and validated with experimental data. Sandhu et al. (2007) developed a diffusion-limited model assuming a cylindrical pore morphology, and presented the transient concentration profiles of the dissolved oxygen in the electrolyte using numerical iterative methods. Battery capacities were predicted and compared with literature experimental results. Nanda et al. (2012) reported a three-dimensional spatial distribution of lithium products using neutron tomographic imaging. They observed a higher concentration of lithium oxides near the edge of electrode; and a relatively uniform distribution in the center area. Similar phenomena were also reported by Wang and Cho (2015), who developed a multi-dimensional model based on the conservation law of Li^+, oxygen, and charges, in conjunction of the electrochemical reaction kinetics. They showed non-uniform distribution in the reaction rate is more remarkable under higher current and explained the sluggish oxygen transport is the primary cause. They also analyzed the oxygen content variation in the supply channel, indicating it is determined by a dimensionless number and thin channels is desirable to achieve high energy density without sacrificing oxygen supply. Wang (2012) pointed out that lithium oxide precipitation is similar to water freezing in PEM fuel cells under sub-freezing condition, and explained the similarity between ice formation within PEM fuel cells (Mishler el al., 2012; Wang el al., 2010) and oxide precipitate in Li-air batteries. A coverage model was developed to account for oxide precipitate’s effects, and validated against the experimental data for planar electrodes. Wang and Cho (2013) further extended the fuel cell knowledge to Li-air battery by developing the formula of the voltage losses due to electrode passivation and oxygen transport resistance, respectively, raised by oxide precipitate. Their analysis indicated that the electrode passivation contributes the major voltage loss at the beginning of discharge, while the oxygen resistance can be significant near the “sudden death”.

Though a great deal of effort was made in Li-air battery development, most were focused on the aspects of material development and electrochemistry exploration. Theoretical analysis is largely lacked at current stage, particularly those that can be directly applied for battery design and optimization. In this chapter, we investigate the air cathode performance through evaluating the spatial variation of important cathode quantities, analyzing oxygen profiles, modeling electrode passivation through surface coverage, and formulating oxygen transport polarization. Oxygen profiles are analytically obtained under various conditions, along with the oxygen transport polarization. A formula is derived to examine the effects of a few important parameters on the capability of storing Li oxides in air cathodes.

2.2 The Damköhler Number

During operation, the energy conversion inefficiency gives rise to thermal energy release and consequent temperature gradient. Temperature has profound effects on Li-air battery operation as it determines the capability of overcoming the activation barrier of a reaction. The principle mechanisms for waste heat generation include the reversible and irreversible heats of the electrochemical reactions, and ohmic heat. The reversible and irreversible sources are released at the reaction interface during energy conversion, whereas the ohmic heating arises from the resistance to the electric current flow and ion movement. The upper bound of temperature variation can be evaluated by (Wang, 2007):

$$\Delta T = \frac{I(E' - V_{cell})\delta}{2k^{eff}} \quad [2]$$

where E' is defined as $-\frac{\Delta \bar{h}}{2F}$ and represents the EMF (electromotive force) that all the energy from the Li-oxygen reaction, the 'calorific value', heating value, or enthalpy of formation, were transformed into electrical energy. Giving 1.0 $W/m \cdot K$, 2.5 V, and 1 mA/cm^2 will yield ΔT around 0.01 ℃. Under a higher current of 0.1 A/cm^2, ΔT will be around 1 ℃.

In discharging, Li$^+$, oxygen, and electrons are consumed in the cathode. The primary driving forces for the reactant supply are the gradients of their concentrations (for Li$^+$ and oxygen) and electric phase potentials (for ions and electrons). Assuming diffusion and migration dominate Li$^+$ transport, and diffusion is the major driving force for oxygen transport, their spatial variations can be evaluated by:

$$\frac{\Delta C_e}{C_{e,0}} = \frac{(1 - t_+^0)I}{2F} \frac{\delta}{C_{e,0} D_{Ce}^{eff}} \quad and \quad \frac{\Delta C_{O2}}{C_{O2,\delta}} = \frac{I}{8F} \frac{\delta}{C_{O2,\delta} D_{O2}^{eff}} \quad [3]$$

where $C_{e,0}$ and $C_{O2,\delta}$ are the concentrations of Li$^+$ and oxygen at y=0 and y=δ (see Figure 2), respectively, and the transference number of Li$^+$, t_+^0, represents the fraction of the current carried by species Li$^+$. The values of t_+^0 for a few electrolytes are summarized Wang and Cho (2015). The effective oxygen diffusivity will be affected by the insoluble precipitates which will hamper oxygen transport. As the oxygen is transported via the pore network, insoluble precipitates will narrow the passage in the pore structure, reducing the effective oxygen diffusivity. Assuming no porous structure in the precipitates, the effective oxygen diffusivity can be modified following the Bruggeman correlation (Wang, 2007):

$$D_{Ce}^{eff} = \varepsilon^{\tau_d} D_{Ce}^{0} \ \ and \ \ D_{O2}^{eff} = \varepsilon^{\tau_d} D_{O2}^{0} \qquad [4]$$

Another popular correlation is also applicable:

$$D_{eff} = \frac{\varepsilon}{\tau} D \qquad [5]$$

For Eq. [4], the tortuosity factor is determined by the pore network (Tjaden et al., 2016):

$$\tau_d = \begin{cases} 1.5 & (spheres) \\ 2 & (cylinders) \end{cases} \qquad [6]$$

For fibrous paper and cloth, the tortuosity can be 3.0 and 1.1, respectively (Wang et al., 2007). The electrolyte phase potential variation can be evaluated by Ohm's law:

$$\Delta\Phi^{(e)} = \frac{I\delta}{2k^{eff}} \qquad [7]$$

The variation is around 0.001 V under k^{eff} of 1 S/m, 1 mA/cm^2 and δ of 0.1 mm. It can be considerable using low-conductivity electrolytes. Table 1 lists the ionic conductivity for a number of typical electrolytes.

Table 1. Ionic conductivity for various electrolytes. (Wang & Cho, 2013)

Electrolyte	Ionic conductivity	Remarks	Reference
PVA (Poly Vinyl Alcohol)	$10^{-8} \sim 10^{-4}$ S/cm	PVA complexed with lithium triflate system	Every et al., 1998
PC / γ-BL (propylenecarbonate / γ-butyrolactone)	1.7×10^{-3} S/cm	60P(ECH-EO):15PC:10γ-BL:15LiClO$_4$ @ 363K	Nithya el al., 2012
DMF / γ-BL (dimethylformamide / γ-butyrolactone)	2.8×10^{-3} S/cm	60P(ECH-EO):15DMF:10γ-BL:15LiClO$_4$ @ 363K	

PVA(15)–PMMA(10)–LiBF4(8)– EC(67)	9.0377× 10^{-3} S/cm	@373K	Rajendran el al., 2004
PVA(15)–PMMA(10)–LiBF4(8)– PC(67)	2.4855× 10^{-3} S/cm		
PVA(15)–PMMA(10)–LiBF4(8)– DEC(67)	0.2022× 10^{-3} S/cm		
PVA(15)–PMMA(10)–LiBF4(8)– GBL(67)	1.1523× 10^{-3} S/cm		
PVDF- HFP	2×10^{-3} S/cm		Abraham et al., 1983
PVC / PMMA	1.4× 10^{-3} S/cm	@ room temperature	Rhoo el al., 1997
PAN(21)–PEO(2)–$LiCF_3SO_3$ (8)–PC(27.7)–EC(41.3)	1.713 × 10^{-3} S/cm	@373K	Rajendran el al., 2000
PAN(21)–PEO(5)–$LiCF_3SO_3$ (8)–PC(24.7)–EC(41.3)	8.492 × 10^{-3} S/cm		
PAN(21)–PEO(10)–$LiCF_3SO_3$ (8)–PC(27.7)–EC(33.3)	80.950 × 10^{-3} S/cm		
PAN(21)–PEO(15)–$LiCF_3SO_3$ (8)–PC(24.7)–EC(31.3)	23.880× 10^{-3} S/cm		
EC(38) –PC(33) – PAN(21) – $LiClO_4$(8)	3.5 × 10^{-3} S/cm	@323K	Abraham & Alamgir, 1990
EC(42) –PC(36) – PAN(15) – $LiCF_3SO_3$(7)	2.2 × 10^{-3} S/cm		
EC(62) –PC(13) – PAN(16) – PEGDA(1) – $LiClO_4$(8)	3.0 × 10^{-3} S/cm		
EC(68) –PC(15) – PEGDA(3) – $LiClO_4$(14)	8.0 × 10^{-3} S/cm		
EC(35) –PC(31) – PVP(24) – $LiCF_3SO_3$ (10)	1.0 × 10^{-3} S/cm		
EC–$LiClO_4$	10^{-8} ~10^{-7}S/cm	[EC]/[$LiClO_4$] = 0.5 @ 298K	Watanabe el al., 1983
	10^{-6}S/cm	[EC]/[$LiClO_4$] = 1.0 @ 298K	

	10^{-5} ~10^{-4} S/cm	[EC]/[$LiClO_4$] = 2.0 @ 298K	
PEO(22.7) – PAN(17.4) – PrC(7.3) –EC(8.5) – $LiClO_4$(4.3)	0.37×10^{-3} S/cm	HSPE @ 303K	Munichandraiah et al., 1998
PEO(22.7) – PrC(13.3) – $LiClO_4$(1.2)	0.84×10^{-3} S/cm	PEO + PrC @ 303K	
PAN(23.2) – PrC(24.5) – EC(28.4) – $LiClO_4$(3.0)	1.34×10^{-3} S/cm	PAN + PrC + EC @ 303K	
PC-DME	10^{-3} S/cm	(1:1 by wt.) plasticized P(LiOEG$_n$B) n=3, 5, 9	Xu & Angell, 2003
	12×10^{-3} S/cm	(1:1 by vol.) 1M $LiClO_4$ @ 293K	Schalkwijk & Scrosati, 2002
	14×10^{-3} S/cm	(1:1 by vol.) 1M $LiPF_6$ @ 293K	
EC-DMC	8×10^{-3} S/cm	(1:1 by vol.) 1M $LiClO_4$ @ 293K	
	10×10^{-3} S/cm	(1:1 by vol.) 1M $LiPF_6$ @ 293K	
	11.7×10^{-3} S/cm	(1:1 by mol) 1M $LiPF_6$@ 303K	Birke et al., 1996
	< 10^{-3} S/cm	(1:2 by wt.) plasticized P(LiOEG$_n$B) n=3	Xu & Angell, 2003
DME	5.52×10^{-3} S/cm	1mol LiF + 1mol $(C_6F_5)_3B$ in DME	Sun el al., 1998
	7.43×10^{-3} S/cm	1mol CF_3CO_2Li + 1mol $(C_6F_5)_3B$ in DME	
	5.52×10^{-3} S/cm	1mol $C_2F_5CO_2Li$ + 1mol $(C_6F_5)_3B$ in DME	

A Damköhler (*Da*) number can be defined based on oxygen diffusivity (Wang, 2007):

$$Da = \frac{I}{8F}\frac{\delta}{C_{O2,\delta}D_{O2}^{eff}} = \frac{Reaction\ rate}{Mass\ transport\ rate} \qquad [8]$$

With this definition, one can rewrite the above formula of variations as below:

$$\frac{\Delta C_{O2}}{C_{O2,\delta}} = \frac{\Delta\Phi^{(e)}}{4FC_{O2,\delta}\frac{D_{O2}}{\kappa}}Da,$$

$$\frac{\Delta C_e}{C_{e,0}} = 4(1-t_+^0)\frac{C_{O2,\delta}D_{O2}}{C_{e,0}D_{Ce}}\ Da, \qquad [9]$$

$$and\ \Delta T = 4F(E' - V_{cell})\frac{D_{O2}^{eff}}{k^{eff}}C_{O2,\delta}Da$$

Da is around 0.04 for 0.1 mA/cm^2 or 1 A/m^2, δ of 0.1 mm, ε of 0.75, τ_d of 1.5, D_{O2} of 10^{-9} m^2/s and $C_{O2,\delta}$ of 5 mol/m^3 (5 mM). This Da will yield an oxygen concentration variation of ~4%. For other quantities such as T and $\Phi^{(e)}$, their variations are also small under Da of ~0.04 and common conditions, such as k^{eff} of ~1 $W/m \cdot K$ and κ of ~0.001 S/cm.

In air cathodes, the actual electrochemical reaction kinetics and paths of the oxygen reduction reaction (ORR) are complex, involving a number of reaction steps and intermediates. For the ORR in dimethyl sulfoxide (DMSO)/$LiPF_6$ electrolytes, the following steps were suggested (O'Laoire, 2010):

$$\begin{gathered} Step\ 1\text{: } \mathrm{O_2 + Li^+ + e^- = LiO_2} \\ Step\ 2\text{: } \mathrm{2LiO_2 = Li_2O_2 + O_2}\ (chemical) \\ Step\ 3\text{: } LiO_2 + Li^+ + e^- = Li_2O_2 \\ Step\ 4\text{: } Li_2O_2 + 2Li^+ + 2e^- = 2Li_2O \end{gathered} \qquad [10]$$

For the sake of simplification, a one-step reaction is assumed with the discharge reaction rate approximated by the Tafel equation:

$$j_c = -ai_c = -ai_{0,c}^{ref}C_{O2}^{1-\beta}C_e^{1-\beta}\exp\left(-\frac{1-\beta}{RT}F\eta\right) \qquad [11]$$

where a represents the surface-to-volume ratio, determined by the electrode roughness. The surface overpotential η is determined by the local phase potentials and equilibrium potential U_0:

$$\eta = \Phi^{(s)} - \Phi^{(e)} - U_0 \qquad [12]$$

The above considers no precipitates deposited at the reaction surface. For a sufficiently small Da, the spatial variations of temperature, phase potentials, oxygen concentration, and C_e are negligibly small, thus the exchange current density j_c can be treated uniform across the entire thickness of the air cathode.

2.3 Oxygen Transport

In air cathodes, liquid electrolyte occupies the pore network. Oxygen is dissolved in the electrolyte at the electrolyte-gas interface, and then transported to the reaction surface for consumption during discharge. The 1-D transport equation is written as follow (Wang, 2007):

$$\frac{\partial \varepsilon C_{O2}}{\partial t} + \frac{\partial u C_{O2}}{\partial x} = \frac{\partial}{\partial x}(D_{O2}^{eff} \frac{\partial C_{O2}}{\partial x}) + \frac{j_c}{4F} \qquad [13]$$

In common operation, the mass consumption by the electrochemical reactions is negligibly small for promoting any considerable mass flow. Thus, the convection term can be neglected. Time constant analysis (Wang & Cho, 2013) indicated that the transient term can be neglected, comparing with the single discharge timescale. One will then reach the below equation:

$$\frac{d}{dy}\left(D_{O2}^{eff} \frac{dC_{O2}}{dy}\right) = k C_{O2}^{1-\beta}$$

$$k = \frac{a i_{0,c}^{ref} C_e^{1-\beta}}{4F} \exp\left(-\frac{1-\beta}{RT} F\eta\right) \qquad [14]$$

The boundary conditions are written as:

$$\frac{dC_{O2}(0)}{dy} = 0$$

$$C_{O2}(\delta) = C_{O2,\delta} \qquad [15]$$

Oxygen diffusivity in liquid electrolytes can be evaluated using a hydrodynamic model, which assumes that the resistance of solute molecule movement arises from the viscous force, similar to the particle movement in viscous fluids. In a dilute liquid, the hydrodynamic approach results in the famous Stokes–Einstein equation:

$$D_{O2} = \frac{k_B T}{6\pi r \mu} \qquad [16]$$

where k_B is the Boltzmann's constant, r the oxygen molecular radius, and μ the electrolyte viscosity. Using the Stokes-Einstein equation, the oxygen diffusivity ranges from 10^{-11} to 10^{-8} m^2/s. Table 2 summarizes the oxygen diffusivity in a few electrolytes.

Table 2. Oxygen diffusivity in nonaqueous electrolytes. (Wang & Cho, 2015)

Oxygen diffusivity	Electrolyte	Reference
7.0 x 10^{-6} cm^2/s	1M $LiPF_6$ in PC:DME (1:1)	Read et al., 2003
4.0 – 4.5 x 10^{-5} cm^2/s	CCl_4	Wu et al., 1997
5.1 – 5.5 x 10^{-5} cm^2/s	CS_2	Wu et al., 1997
2.9 – 3.4 x 10^{-5} cm^2/s	$C_2H_4CL_2$	Wu et al., 1997
1.3 – 1.7 x 10^{-5} cm^2/s	CH_2CL_2	Wu et al., 1997
9.75 x 10^{-6} cm^2/s	0.1M $TBAPF_6$ in DMSO	O’Laoire et al., 2010
2.45 x 10^{-5} cm^2/s	0.1M $TBAPF_6$ in MeCN	O’Laoire et al., 2010
1.67 x 10^{-5} cm^2/s	0.1M $LiPF_6$ in DMSO	O’Laoire et al., 2010
4.64 x 10^{-6} cm^2/s	0.1 M $LiPF_6$ in MeCN	O’Laoire et al., 2010
1.22 x 10^{-5} cm^2/s	0.1M $LiPF_6$ in DME	O’Laoire et al., 2010
3.88 x 10^{-6} cm^2/s	0.1M $TBAPF_6$ in DME	O’Laoire et al., 2010
2.17 x 10^{-6} cm^2/s	0.1M $LiPF_6$ in TEGDME	O’Laoire et al., 2010
4 x 10^{-5} cm^2/s	1M Li^+ in DME	Lu et al., 2011
9 x 10^{-6} cm^2/s	1M Li^+ in PC:DME(1:2)	Lu et al., 2011
2.2 x 10^{-6} cm^2/s	1M $L{:}i^+$ in PC	Lu et al., 2011
2.2 x 10^{-5} cm^2/s	0.1M $TBAClO_4$	Laoire et al., 2009
2.1 x 10^{-5} cm^2/s	0.1M $TBAPF_6$	Laoire et al., 2009

For general cases, the above problem of oxygen transport is written in the dimensionless form as:

$$\frac{d}{d\bar{y}}\left(\frac{d\bar{C}_{O2}}{d\bar{y}}\right) = 2Da * \bar{C}_{O2}^{\,1-\beta} \qquad [17]$$

where a more general Damköhler (Da) number is defined as

$$Da = \frac{k\delta^2}{2D_{O2}^{eff}\ C_{O2,0}^{\beta}} = \frac{reaction\ rate}{mass\ transport\ rate} \tag{18}$$

Boundary conditions are set as:

$$\frac{d\bar{C}_{\ O2}(0)}{d\bar{y}} = 0$$
$$\bar{C}_{\ O2}(1) = 1 \tag{19}$$

For $\beta = 0$ and 1, one can solve directly the problem:

$$\beta = 1{:}\ \bar{C}_{O2} = 1 - Da(1 - \bar{y}^2)$$
$$\beta = 0{:}\ \bar{C}_{O2} = \frac{\cosh(\sqrt{2Da}\bar{y})}{\cosh(\sqrt{2Da})} \tag{20}$$

For the case of β=0.5, which was adopted by a few studies (Albertus et al., 2011; Wang, 2012), the problem is nonlinear and can be solved through numerical iterative methods. In addition, using perturbation analysis, one can define a small parameter ε=Da , and write the solution in the form of a formal power series or perturbation series ($\bar{C}_{O2} = \sum_{n=0}^{\infty} a_n \varepsilon^n$), and solve a_0 and a_1 for an approximate solution with an accuracy of O(ε^2) or O(Da^2). The perturbation solution is found to be the same as the exact solution to β =1, as shown in Eq. [20].

Figure 3 plots the oxygen profiles in an air cathode, showing that under Da of 0.04, oxygen variation is small <5%; and the oxygen profiles are almost identical for the three β values. There is appreciable discrepancy among the three under Da of 0.2, but less than 3%.

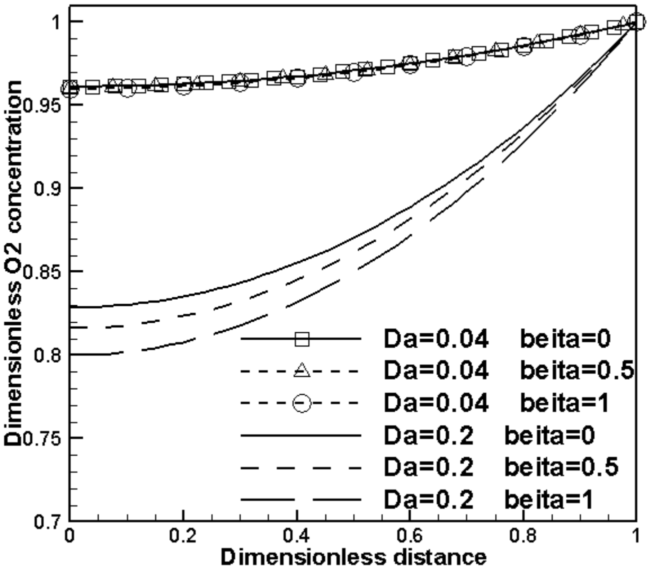

Figure 3: Oxygen profiles in an air cathode under different Da and β.

Local oxygen consumption and discharge product generation are determined by the local electrochemical reaction, which in turn depends on local oxygen content and discharge product volume fraction. Li oxides precipitate in the pore network and narrow down the passage, reducing the effective oxygen diffusivity. Assuming the film is firmly packed without any pore structure, the effective diffusivity can be modified following the Bruggeman correlation:

$$D_{O2}^{eff} = \varepsilon^{\tau_d} D_{O2}^{0} = \left(\varepsilon_0 - \varepsilon_{prod}\right)^{\tau_d} D_{O2}^{0} = \varepsilon^{\tau_d}(1-s)^{\tau_d} D_{O2}^{0} \qquad [21]$$

where τ_d represents the diffusion path’s tortuosity, ε_0 the initial porosity of an air cathode in absence of oxide precipitate, and ε_{prod} the volume fraction of oxide precipitate inside pores.

Analytically solving this electrochemically coupled transport problem is challenging, particularly when the effects of oxide precipitate on oxygen diffusivity and consumption are taken into account. One method is to evaluate the associated voltage loss by assuming the cathode consists of a number of independent reactors operated under constant current, as done in in PEM fuel cells (Wang, 2007; Wang et al., 2013). As the reaction is uniform, the local reaction rate $j_c = -\frac{I}{\delta}$; and the oxygen concentration is analytically obtained as below:

$$\bar{C}_{O2}(\bar{y}) = 1 - Da\frac{1-\bar{y}^2}{\varepsilon^{\tau_d-\tau_{d,0}}\left(1-\frac{\varepsilon_{prod}}{\varepsilon_0}\right)^{\tau_d}} = 1 - Da\frac{1-\bar{y}^2}{\varepsilon^{\tau_d-\tau_{d,0}}(1-s)^{\tau_d}} \qquad [22]$$

Figure 4 plots the oxygen profiles under various Da and oxide precipitate's volume fractions. The oxygen spatial variation is larger when oxide precipitate is present, as a result of the increased oxygen transport resistance. For Da of 0.2 and s of 0.4, the local oxygen content varies by >40%. For Da of 0.04 and s of 0.4, the variation is still small within 10%. For Da of 0.01, the precipitate's effect is about 1%.

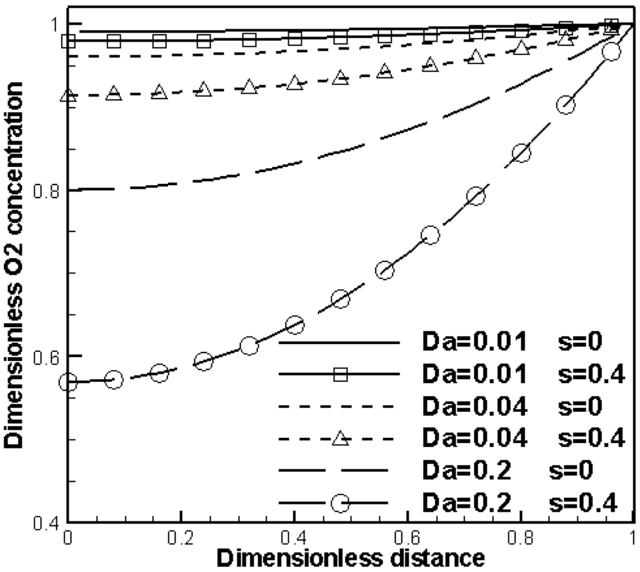

Figure 4: Oxygen profile in an air cathode under β=0.5 and two levels of the Li oxide volume fraction.

2.4 Surface Coverage Mode

During discharging, insoluble Li oxides are produced and deposited at local reaction sites. It is likely the initial precipitate nucleates heterogeneously at preferred sites, followed by thin film formation over the surface. Film formation was experimentally observed over flat electrodes, see Figure 5 (f). The deposit film has low electric conductivity, resisting electrons to react with Li^+ and oxygen. Figure 5 sketches a few typical modes of film growth. A porous electrode consists of reaction surfaces of various morphologies. Thus, the film growth is complex. The below power law is frequently adopted to describe the reaction surface reduction arising from precipitate (Wang et al., 2013):

$$a = a_0 \left(1 - \frac{\varepsilon_{prod}}{\varepsilon_0}\right)^{\tau_a} \qquad [23]$$

where $\frac{\varepsilon_{prod}}{\varepsilon_0}$ is the volume fraction of insoluble precipitates in the pore space, and τ_a denotes the coverage coefficient, measuring the degree of insoluble product effect on the reaction area. This empirical expression was also adopted to describe the impact of liquid water and ice on the electrochemical reaction area in PEM fuel cells (Wang et al., 2013). A similar expression was reported by others (LaFollette et al., 1990; Wang et al., 1998):

$$a = a_0 \left[1 - \left(\frac{\varepsilon_{prod}}{\varepsilon_0}\right)^{\tau_a}\right] \qquad [24]$$

The volume of precipitate ε_{prod} is calculated through the reaction rate via the Faraday's law (Andrei et al., 2010):

$$\varepsilon_{prod} = \int_0^t -\frac{j_c M_{prod}}{nF\rho_{prod}} dt = \varepsilon_{prod,0} + \frac{IM_{prod}}{n\delta\, F\rho_{prod}} t \qquad [25]$$

where n denotes the moles of electrons transferred per mole of the product.

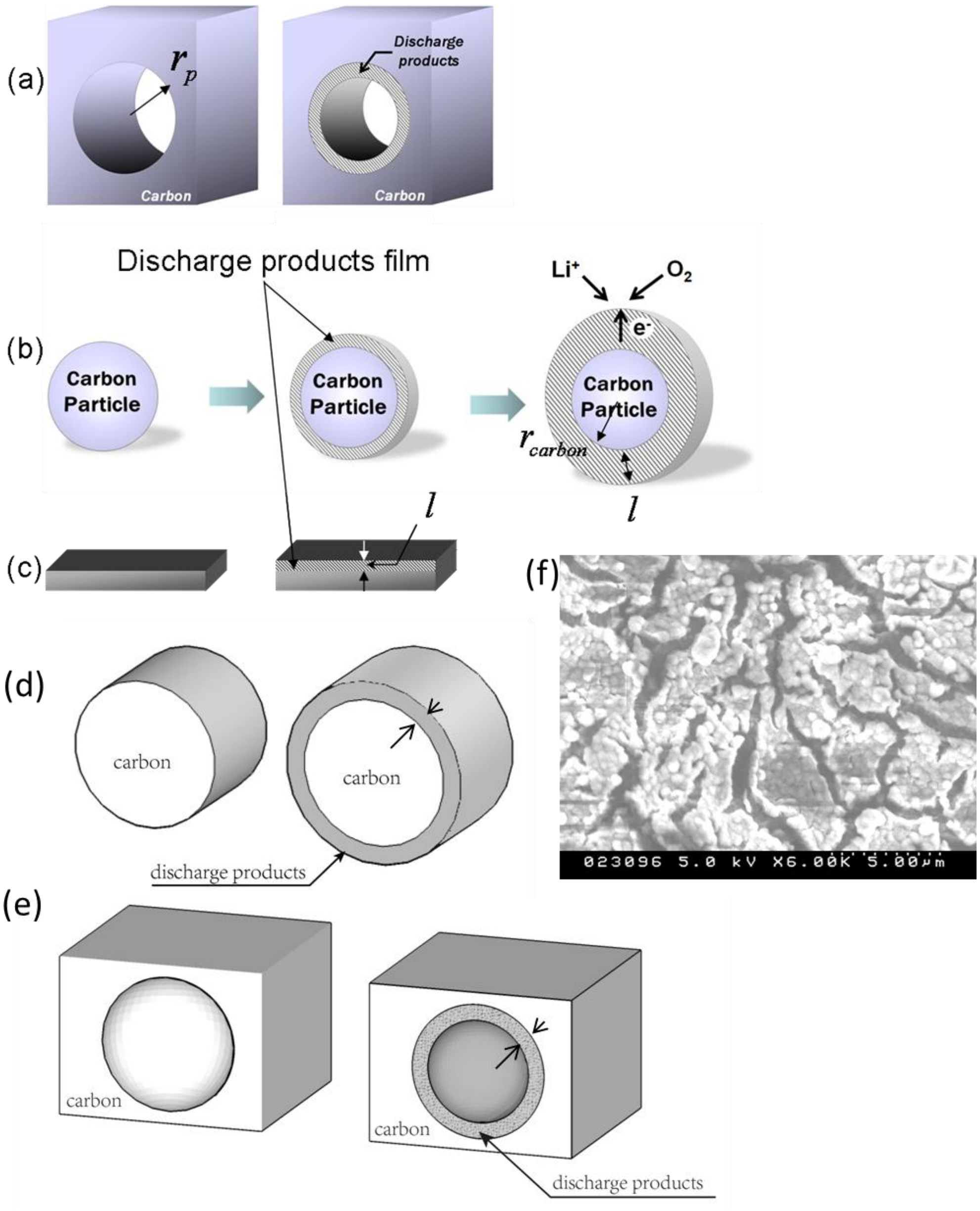

Figure 5: Typical growth modes of the oxide precipitate film in air cathodes: a.) the inward cylindrical-film growth mode; b.) the outward spherical-film growth mode; c.) the planar-film growth mode; d.) the outward cylindrical-film mode; e.) the inward spherical-film mode; f.) the SEM image of precipitate on highly ordered pyrolytic graphite (HOPG) at 10 $\mu A/cm^2$ for 1M LiTriflate in DOL:DME (1:1 w/w).

The above coverage model is more general, encompassing the film resistor model. For the spherical-film growth mode, the exponent coefficient τ_a is given by (Wang, 2012):

$$\tau_a = -\frac{I(1-\beta)F}{a_0 RT ln\left(1-\frac{\varepsilon_{prod}}{\varepsilon_0}\right)}\left\{A_0\left[\left(1+\frac{\varepsilon_{prod}}{\varepsilon_{carbon}}\right)^{\frac{1}{3}}-1\right]r_{carbon} + R_0\right\} \qquad [26]$$

where A_0 is the proportional coefficient between the film resistance and the film thickness (Albertus et al., 2011), and R_0 is the contact resistance between the carbon particle and deposit shell (Wang, 2012). The above indicates that τ_a is proportional to the current density I and a function of ε_{prod}. In actual porous electrodes, various growth modes of insoluble products are encountered. The following correlation was proposed to account for the effects of current density and insoluble product volume fraction by Wang (2012):

$$\tau_a = \begin{cases} B_1\frac{I}{I_0} & s < s_0 \;\; where \;\; s = \frac{\varepsilon_{prod}}{\varepsilon_0} \\ \frac{I}{I_0}[B_1 + B_2(s-s_0)] & otherwise \end{cases} \qquad [27]$$

For the spherical-film growth mode and R_0=0, the parameters are given by:

$$\frac{B_1}{I_0} = \frac{(1-\beta)FA_0 r_{carbon}\varepsilon_0}{3a_0 RT\varepsilon_{carbon}}$$

$$\frac{B_2}{I_0} = \frac{(1-\beta)FA_0 r_{carbon}}{a_0 RT}\left(\frac{\varepsilon_0/\varepsilon_{carbon}}{3\ln(1-s_0)\left(\frac{s_0\varepsilon_0}{\varepsilon_{carbon}}+1\right)^{2/3}} + \frac{(s_0\varepsilon_0/\varepsilon_{carbon}+1)^{1/3}-1}{(1-s_0)(\ln(1-s_0))^2}\right) \qquad [28]$$

2.5 Discharge Voltage Loss

The oxygen profile of Eq. [22] is substituted into Eq. [11], yielding the below overpotential change (Wang, 2007):

$$\Delta\eta = \frac{\mathrm{RT}}{(1-\beta)\mathrm{F}}\left[\tau_a \ln(1-s) + (1-\beta)\ln\left(1 - \mathrm{Da}\frac{1-(\bar{y})^2}{\varepsilon^{\tau_d-\tau_{d,0}}(1-s)^{\tau_d}}\right)\right] = \Delta\eta_a + \Delta\eta_{O2}$$

$$\Delta\eta_a = \frac{RT\tau_a ln(1-s)}{(1-\beta)F} \qquad [29]$$

$$\Delta\eta_{O2} = \frac{RT}{F} ln\left(1 - Da\frac{1-(\bar{y})^2}{\varepsilon^{\tau_d-\tau_{d,0}}(1-s)^{\tau_d}}\right)$$

Note that $\Delta\eta_{O2}$ contains the oxygen transport voltage loss prior to formation of any precipitates in the cathode. In some work, one needs to extract the voltage loss caused by discharge deposit only, which can be achieved by eliminating the portion of the oxygen transport voltage loss prior to formation of any precipitates:

$$\Delta\eta = \frac{\mathrm{RT}}{(1-\beta)\mathrm{F}}\left[\tau_a \ln(1-s) + (1-\beta)\ln\left(\frac{1 - \mathrm{Da}\frac{1-(\bar{y})^2}{\varepsilon^{\tau_d-\tau_{d,0}}(1-s)^{\tau_d}}}{1 - \mathrm{Da}\frac{1-(\bar{y})^2}{\varepsilon^{\tau_d-\tau_{d,0}}}}\right)\right] = \Delta\eta_a + \Delta\eta_d$$

$$\Delta\eta_a = \frac{RT\tau_a ln(1-s)}{(1-\beta)F} \qquad [30]$$

$$\Delta\eta_d = \frac{\mathrm{RT}}{\mathrm{F}}\ln\left(\frac{1 - \mathrm{Da}\frac{1-(\bar{y})^2}{\varepsilon^{\tau_d-\tau_{d,0}}(1-s)^{\tau_d}}}{1 - \mathrm{Da}\frac{1-(\bar{y})^2}{\varepsilon^{\tau_d-\tau_{d,0}}}}\right)$$

$\Delta\eta_a$ represents the voltage loss caused by electrode passivation and surface reduction, and $\Delta\eta_d$ denotes the voltage loss associated with the oxygen transport resistance and precipitates. The voltage loss due to the oxygen transport resistance raised by oxide precipitate can be assessed through the overpotential at the middle thickness, i.e.

$$\Delta\eta_d(\bar{y} = 0.5) = \frac{RT}{F} ln\left(\frac{1 - \frac{3\mathrm{Da}}{4\varepsilon^{\tau_d-\tau_{d,0}}(1-s)^{\tau_d}}}{1 - \frac{3\mathrm{Da}}{4\varepsilon^{\tau_d-\tau_{d,0}}}}\right) \qquad [31]$$

For evaluation, the total voltage loss associated with oxide precipitate, i.e. the raised oxygen transport polarization and electric passivation, can be approximated by:

$$\Delta\eta = \Delta\eta_a + \Delta\eta_d(\bar{y} = 0.5) \qquad [32]$$

In the below comparison with experimental data, a similar set of model parameters were used for all the cases, listed in Table 3. Figure 6 and Figure 7 present comparison with experimental data from Zhang and Read (2011) (case 1) and Sahapatsombut et al. (2014) (case 2), respetively, showing acceptable agreements: the first stage of gradual decrease arises primarily from electrode passivation due to oxide precipitation at the reaction surface; the latter precipitous drop is mainly caused by the oxygen transport resistance due to Li oxides occupying the cathode's pore space. In Figure 7, the initial rapid drop observed in the experiment was likely due to other mechanisms, not raised by oxide precipitation.

Table 3. Physical, electrochemical, and model parameters.

Description	Unit	Value
Temperature	℃	25
Transfer coefficient β	-	0.5
Faraday constant	C/mol	96,487
Electrical conductivity of cathode electrode	S/m	~10
O_2 diffusivity in electrolyte	m^2/s	9×10^{-10}
Equilibrium oxygen concentration (case 1/case 2)	$mol/\,m^3$	2.30/4.33
Cathode thermal conductivity	$W/m \cdot K$	~1.0
Tortuosity τ	-	1.8
Electrode porosity ε_0	-	0.75
Electrode thickness δ	mm	0.5/0.75
Density of discharge product (Li_2O_2/ Li_2CO_3)	kg/m^3	2227/2310
Molecular weight of discharge product (Li_2O_2/Li_2CO_3)	kg/mol	0.04044/0.04588
A_0	$\Omega \cdot m^2$	8.5×10^7
I_0	A/m	0.5
B_1 in Eq. [27] (Wang, 2012)	-	2.5
B_2 in Eq. [27] (case 1, Wang, 2012/case 2, Wang & Cho, 2013)	-	8/12
s_0 in Eq. [27] (Wang & Cho, 2013)	-	0.2

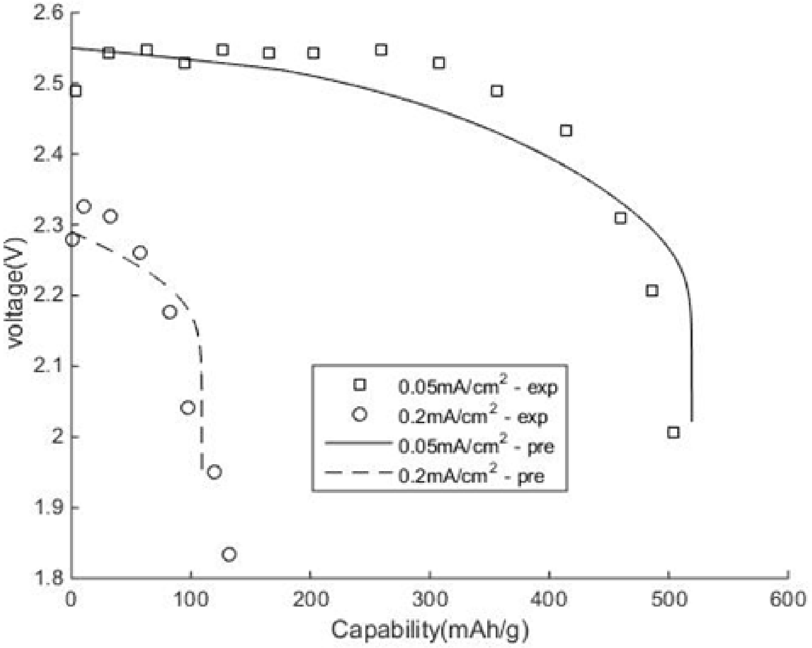

Figure 6: Comparison of the model prediction with experimental data (Zhang & Read, 2011). (Wang et al., 2015)

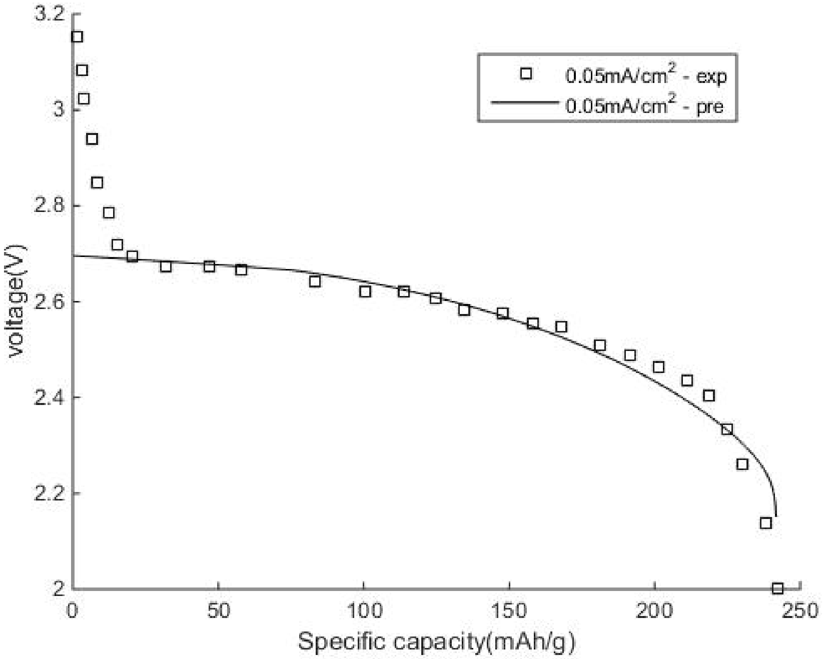

Figure 7: Comparison of the model prediction with experimental data (Sahapatsombut et al., 2014). (Wang et al., 2015)

Figure 8 compares the model prediction with experimental data under two current densities, 0.08 $\mathrm{mA/cm^2}$ and 0.24 $\mathrm{mA/cm^2}$. The physical properties and model parameters are listed in Table 4. Acceptable agreements are achieved for the two current densities. It can be seen the discharge voltage evolution experiences a first slow decrease, followed by a fast drop in the latter stage. The first stage of slow decrease is primarily caused by the electrode passivation and surface reduction due to the insoluble discharge precipitates in the cathode. As to the latter stage, the fast drop is primarily due to the pore network clogging due to precipitates, which hampers oxygen access to the reaction site.

Table 4. Physical properties and model parameters. (Albertus el al., 2011; Yuan & Wang, 2015)

Parameter	Unit	Value
Temperature	K	298
Transfer Coefficient β	-	0.5
Faraday Constant	C/mol	96485
O_2 Diffusivity in Electrolyte	m^2/s	1.83×10^{-9}
O_2 Concentration	Mol/m^3	3.98
Tortuosity τ	-	1.8
Electrode Porosity	-	0.878
Electrode Thickness	mm	1.17
Product Molar Fraction	-	$Li_2O_2: Li_2O = 66: 34$
Product Density	Kg/m^3	2227
Product Molecular Weight	Kg/mol	0.04044
I_0	A/m^2	0.6
B_1	-	2.5
B_2	-	8
s_0	-	0.2

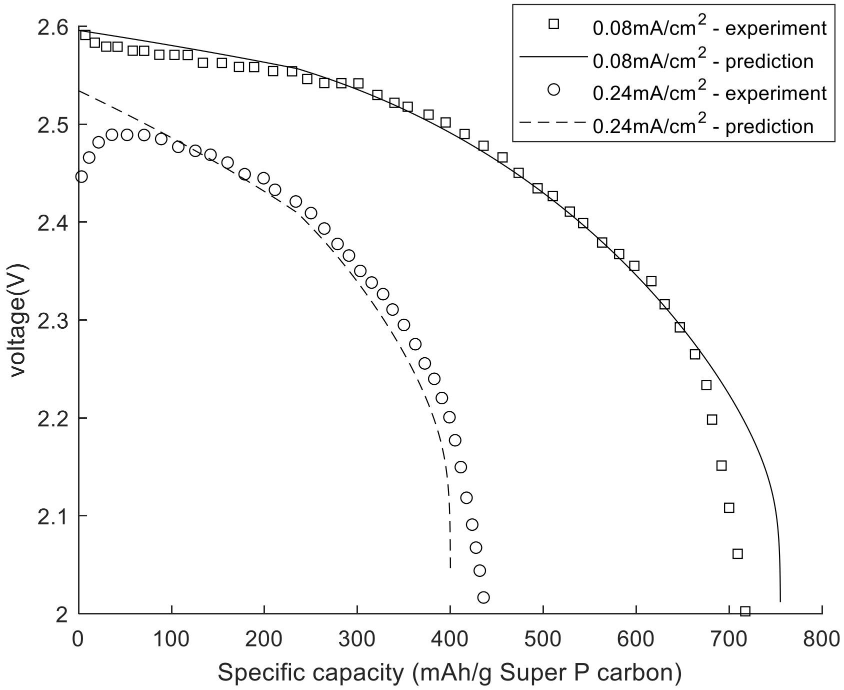

Figure 8: Comparison of the predicted voltage with the experimental data (Albertus el al., 2011). The experiment was operated on Li-air battery using a PVDF/super P/NMP air cathode.

Figure 9 plots the $\Delta\eta_a$ and $\Delta\eta_d$ as a function of the deposit volume fraction in the validation of Figure 8. Their physical meanings are the voltage losses caused by the two mechanisms, respectively: $\Delta\eta_a$ arises from the electrode passivation and surface reduction, while $\Delta\eta_d$ is caused by the oxygen transport clogging. It can be seen in the most duration of discharging, electrode passivation and surface reduction are responsible for the main voltage loss. Only in the very small duration near the cutoff voltage, the voltage loss associated with the oxygen transport becomes significant.

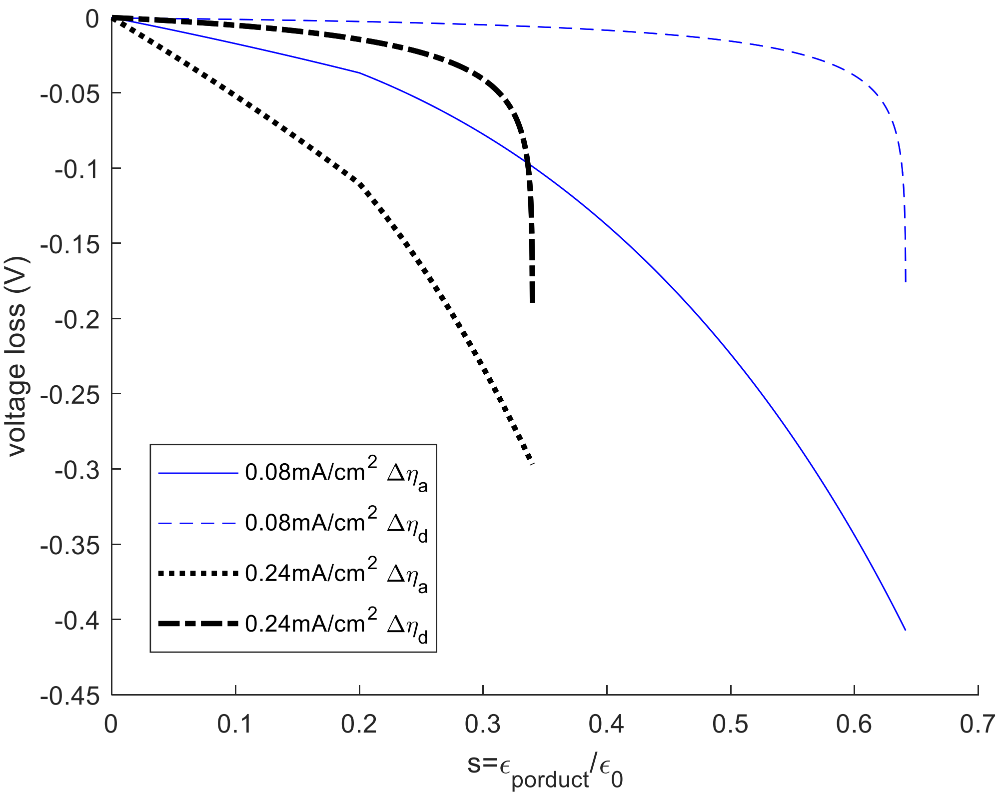

Figure 9: $\Delta\eta_a$ and $\Delta\eta_d$ as a function of the precipitate volume fraction for the current densities in the validation of Figure 8. η_a arises from electrode passivation and surface reduction. $\Delta\eta_d$ is caused by oxygen transport clogging.

A few parameters, including *Da*, tortuosity τ_d, and surface coverage factor τ_a, greatly impact the voltage evolution and capacity loss. As discharge proceeds, the volume fraction of oxide precipitate, *s*, increases until reaching the cut-off voltage V_{cut}. Thus, s_{max} occurs at the cut-off voltage, and is closely linked to the battery's energy density providing that the extra space $1-s_{max}$ cannot be used for storing the oxide. By reducing $1-s_{max}$ or increasing s_{max}, the battery's energy density will be improved.

From Eq. [32], one can develop a formula for s_{max} by assuming the voltage loss is caused by oxide precipitate:

$$\mathrm{V_{cut}} - \mathrm{V_0} = \frac{RT}{(1-\beta)F}\left[\tau_a ln(1-s_{max}) + (1-\beta)ln\left(\frac{1-\frac{3}{4}\frac{Da}{(1-s_{max})^{\tau_d}}}{1-\frac{3Da}{4}}\right)\right] \qquad [33]$$

where V_0 and V_{cut} denote the voltages at s=0 and s=s_{max}, respectively. By rearrangement, one will reach:

$$(1-s_{max})^{\tau_a}\left(\frac{1-\mathrm{Da}\frac{3}{4(1-\mathrm{s_{max}})^{\tau_d}}}{1-\frac{3}{4}\mathrm{Da}}\right)^{1-\beta} = \exp\left(\frac{(1-\beta)F(V_{cut}-V_0)}{RT}\right) \qquad [34]$$

For any given operation, i.e. V_0 and V_{cut} are constant, the above formula directly shows s_{max} as a function of a few key parameters.

But it requires numerical iterative methods to solve. To obtain approximate analytic solutions, two regimes are defined though the below two asymptotes, $s_{max,a}$ and $s_{max,d}$:

$$s_{max,a} = 1 - \exp\left(\frac{(1-\beta)F(V_{cut}-V_0)}{RT\tau_a}\right) \qquad [35]$$

$$\mathrm{s_{max,d}} = 1 - \left[\frac{3}{4}\frac{\mathrm{Da}}{1-\left(1-\frac{3}{4}\mathrm{Da}\right)\mathrm{e}^{\frac{\mathrm{F(V_{cut}-V_0)}}{\mathrm{RT}}}}\right]^{\frac{1}{\tau_d}} \qquad [36]$$

In the regime #1, the exact $\mathrm{s_{max}}$ is approximated by $\mathrm{s_{max,a}}$, i.e. the electrode passivation voltage loss will solely fulfill the cut-off voltage loss. It can be seen that $\mathrm{s_{max,a}}$ is determined by the coverage factor, τ_a. In this regime, $\mathrm{s_{max,a}} < \mathrm{s_{max,d}}$. In the regime #2, the exact $\mathrm{s_{max}}$ is approximated by $\mathrm{s_{max,d}}$, i.e. the oxygen transport polarization voltage loss alone will reach the cut-off voltage loss. It can be seen that $\mathrm{s_{max,d}}$ is closely related to the tortuosity, τ_d. In this regime, $\mathrm{s_{max,a}} > \mathrm{s_{max,d}}$. To determine the above two regimes, one can investigate the relationship between τ_a and τ_d. For regime #1, by using $\mathrm{s_{max,a}} \leq \mathrm{s_{max,d}}$, one will obtain,

$$\frac{\tau_d}{\tau_a} \geq \frac{RT}{(1-\beta)F(V_{cut}-V_0)} \ln\left(\frac{3}{4}\frac{Da}{1-e^{\frac{F(V_{cut}-V_0)}{RT}}}\right) \qquad [37]$$

and vice versa for the regime #2.

Figure 10 plots the exact solution of s_{max}, solved by Eq. [34] numerically from an iterative method, and the two asymptotes $s_{max,a}$ and $s_{max,d}$ by Eq. [35] and Eq. [36]. It can be seen that asymptotes provide fairly accurate predictions for both Regime #1 and Regime #2. The maximum difference from the exact one is 6.88% near the across point of the two asymptotes. Note that $s_{max,d}$ is independent of τ_a, thus a horizontal line is plotted in comparison with the other two curves.

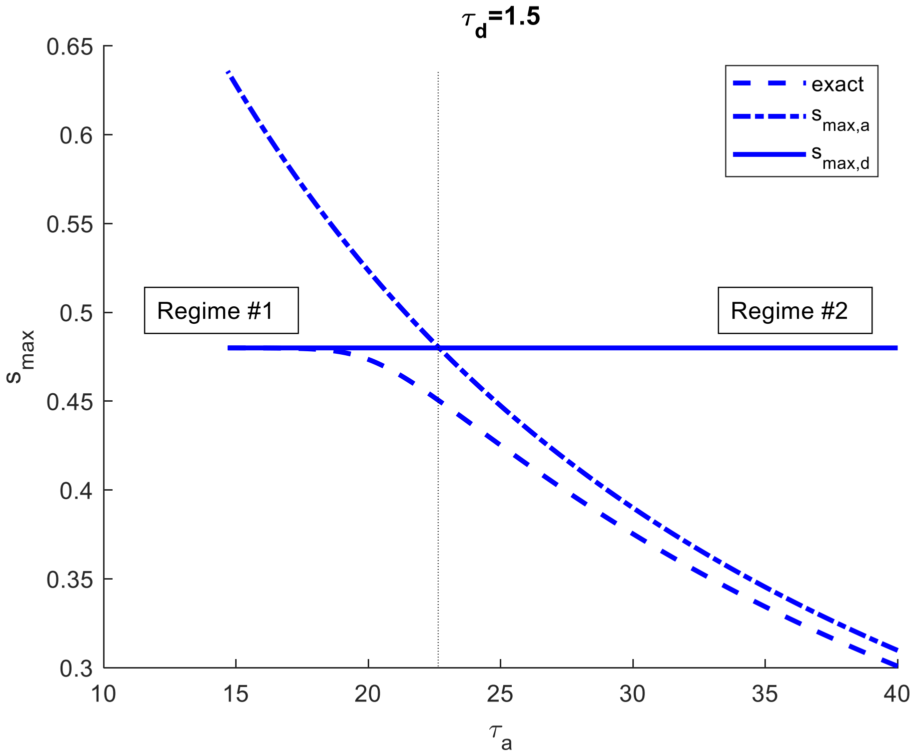

Figure 10: Comparison of s_{max} from Eq. [34], $s_{max,a}$ from Eq. [35], and $s_{max,d}$ from Eq. [36] as a function of the surface coverage factor. Regime #1 is defined for $s_{max,a} \geq s_{max,d}$. Regime #2 is defined for $s_{max,d} > s_{max,a}$. The maximum error is 6.88%.

Figure 11 shows the same result but with $\tau_d = 2.5$, also indicative of a good approximate. Regime #1 is drawn for $s_{max,a} \geq s_{max,d}$, while Regime #2 for $s_{max,d} > s_{max,a}$. The maximum error is 7.63%. In summary, in the range of parameters the two asymptotes provide good approximates to the exact solution. Because $s_{max,a}$ and $s_{max,d}$ can be analytically expressed, approximate solutions can be obtained for charge capacity and energy capacities by replacing s_{max} with one asymptote.

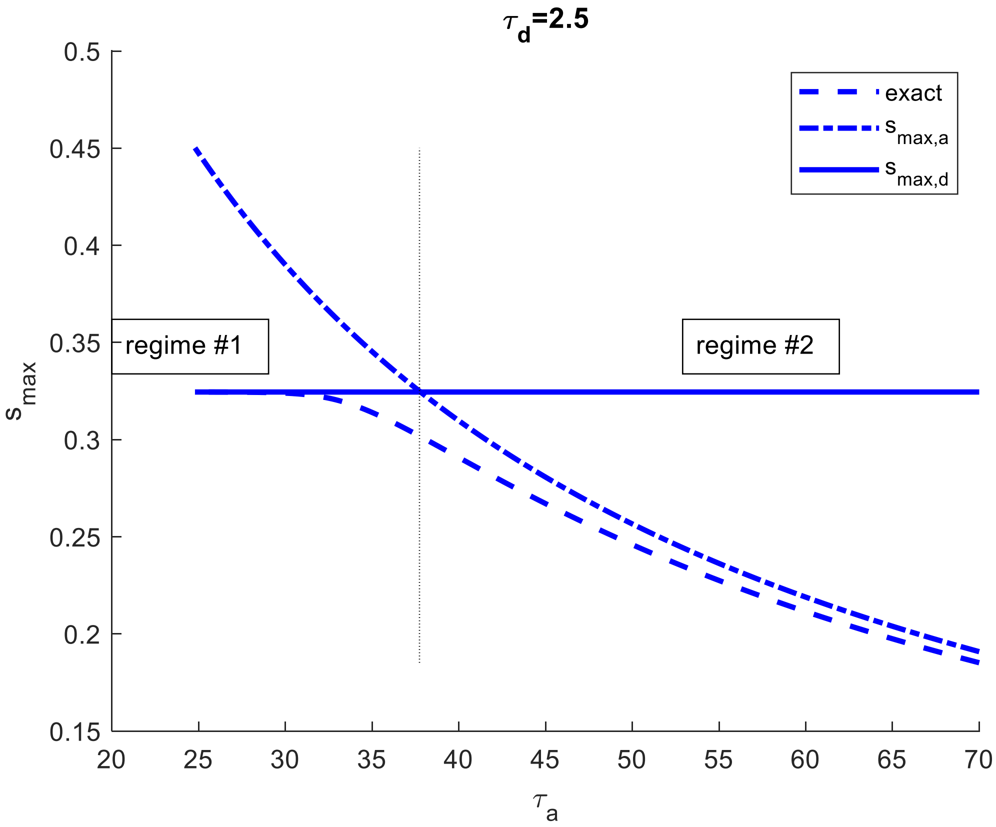

Figure 11: Comparison of s_{max}, $s_{max,a}$, and $s_{max,d}$ under τ_d of 2.5. Regime #1 is defined for $s_{max,a} \geq s_{max,d}$. Regime #2 is defined for $s_{max,d} > s_{max,a}$. The maximum error is 7.63%.

The Eq. [34] can be rearranged to inversely relate s_{max} to those parameters as below:

$$\tau_a = \frac{-\frac{(1-\beta)F(V_0 - V_{cut})}{RT} - (1-\beta)\ln\left(1 - Da\frac{3}{4(1-s_{max})^{\tau_d}}\right)}{\ln(1-s_{max})}$$

$$\tau_d = \frac{\ln\left\{\frac{3}{4}\frac{Da}{1-\left[\frac{\exp\left(-\frac{(1-\beta)F(V_0-V_{cut})}{RT}\right)}{(1-s_{max})^{\tau_a}}\right]^{1/(1-\beta)}}\right\}}{\ln(1-s_{max})} \qquad [38]$$

$$Da = \frac{4}{3}(1-s_{max})^{\tau_a}\left\{1-\left[\frac{\exp\left(-\frac{(1-\beta)F(V_0-V_{cut})}{RT}\right)}{(1-s_{max})^{\tau_a}}\right]^{1/(1-\beta)}\right\}$$

Figure 12 plots the relationship between s_{max} and τ_a under two *Da* numbers, β of 0.5, τ_d of 1.5, V_0 of 2.75 V and V_{cut} of 2.0 V. In PEM fuel cells, the parameter τ_a measures the degree of the produced ice precipitate's impact on the active reaction surface. Local ice morphology at the reaction site likely changes as ice volume increase: from the initial heterogeneous growth to latter film growth. As a result, τ_a may vary with the volume fraction of precipitate (Mishler et al., 2012). In Li-air battery, the parameter τ_a is defined to account for the resistance of oxide precipitate to electron transport, i.e. passivation. It varies with the current density, the volume fraction of oxide precipitate, oxide's electric resistance, and a few other factors such as the reaction surface's area and morphology. In this figure, we consider τ_a as an independent variable, representing the value of τ_a at s_{max}. It is seen that s_{max} is reduced as τ_a increases. The difference between the two Da is small when τ_a is over 7. As τ_a becomes smaller than 6, the difference is evident, with the Da of 0.04 reaching a limit of s_{max} around 0.9 and the Da of 0.01 exhibiting a continuing increase as τ_a further decreases.

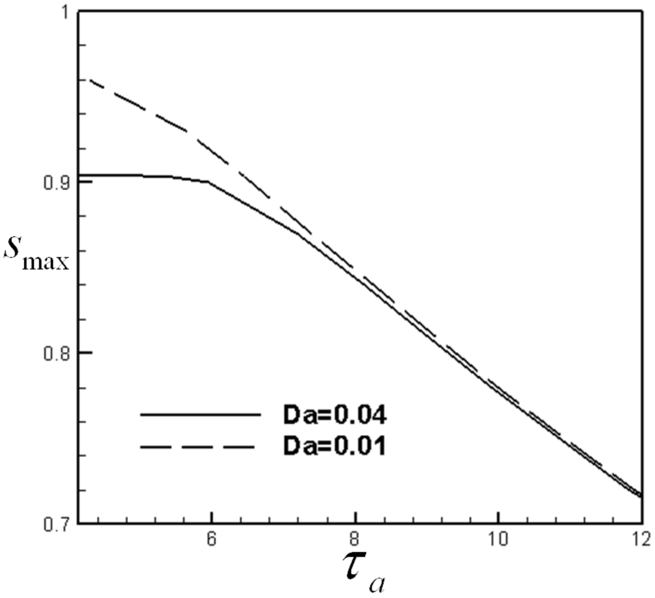

Figure 12: s_{max} as a function of τ_a under β of 0.5, τ_d of 1.5, V_0 of 2.75 V and V_{cut} of 2.0 V.

Figure 13 plots the relationship between s_{max} and τ_d under the two Da numbers, β of 0.5, τ_a of 2.5, V_0 of 2.75 V and V_{cut} of 2.0 V. In porous media, tortuosity τ_d measures the actual length of diffusion passage in a porous medium. In addition, the MacMullin number (N_M), defined as the ratio of resistance of porous media saturated with an electrolyte to the bulk resistance of the same electrolyte:

$$N_m = \frac{D_k}{D_k^{eff}} = \frac{1}{f(\varepsilon, \tau_d)} \qquad [39]$$

In Eq. [4], the MacMullin number is implicitly defined as $\varepsilon^{-\tau}$. Table 5 lists the expression of N_M for various porous media as a function of ε. In general, $f(\varepsilon, \tau_d)$ is determined by the pore structure such as its morphology and arrangement. In some structures, e.g. the fiber matrix in carbon papers, the tortuosity of electron passage can be over 10. Figure 13 shows that as τ_d increases, the effective transport resistance enlarges, thus s_{max} is reduced. The difference between the two Da numbers is evident as shown by the two curves. s_{max} reaches over 90% as

τ_d is below 2.0. A large τ_d, though benefiting the reaction surface area due to the highly torturous structure, yields a big resistance to oxygen transport as the oxide precipitate accumulates.

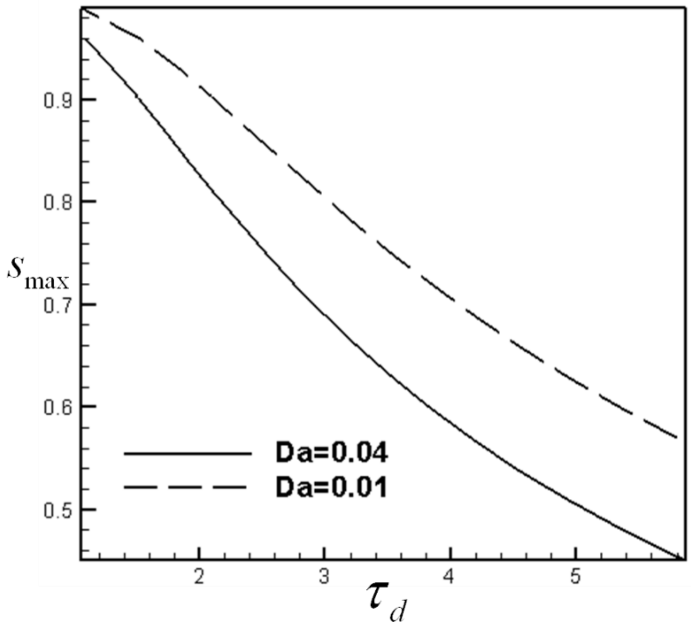

Figure 13: s_{max} as a function of τ_d under β of 0.5, τ_a of 2.5, V_0 of 2.75 V and V_{cut} of 2.0 V.

Table 5. MacMullin number (N_M) of a system consisting of a dispersed non-conducting phase in a conductive medium. (Wang et al., 2013; Martínez et al., 2009)

Label	Geometry	Arrangement	Size	Expression
I	Spheres	Random	Uniform	$N_M = \frac{(5-\varepsilon)(3+\varepsilon)}{8(1+\varepsilon)\varepsilon}$
II	Spheres	Cubic lattice	Uniform	$N_M = \left\{(3-\varepsilon)\left[\frac{4}{3}+0.409(1-\varepsilon)^{7/3}\right] - 1.315(1-\varepsilon)^{10/3}\right\} / \left\{2\varepsilon\left[\frac{4}{3}+0.409(1-\varepsilon)^{7/3}\right] - 1.315(1-\varepsilon)^{10/3}\right\}$
III	Spheres	Random and ordered	Range	$N_M = \varepsilon^{-1.5}$

IV	Cylinders	Parallel (square array)	Uniform	$N_M = [2 - \varepsilon - 0.3058(1-\varepsilon)^4 - 1.334(1-\varepsilon)^8] / [\varepsilon - 0.3058(1-\varepsilon)^4 - 1.334(1-\varepsilon)^8]$
V	Fibrous material (Cylinders)	Random	-	$N_M = \frac{0.9126}{\varepsilon(\varepsilon - 0.11)^{0.785}}$

Figure 14 plots the relationship between s_{max} and Da under β of 0.5, τ_a of 2.5, V_0 of 2.75 V, and V_{cut} of 2.0 V. As defined by Eq. [18], Da represents the ratio of the reaction rate to oxygen transport rate, characterizing the operation of a chemical reactor. To fully utilize the pore space in cathode, Da should be kept low in order to avoid considerable spatial variations in the reaction rate and hence in the oxide precipitate's content. This figure shows as Da increases (i.e. the transport resistance relative to the reaction rate enlarges), s_{max} is reduced, as expected. The difference between two τ_d is evident as shown by the two curves. s_{max} is rapidly reduced to below 50% as Da approaches 0.2 under τ_d of 3.0. Solid oxide precipitate accumulates inside the pore network, narrowing down the diffusive passage. A larger τ_d will yield a bigger influence of oxide precipitate, and consequently a smaller oxide storage capability of air cathode.

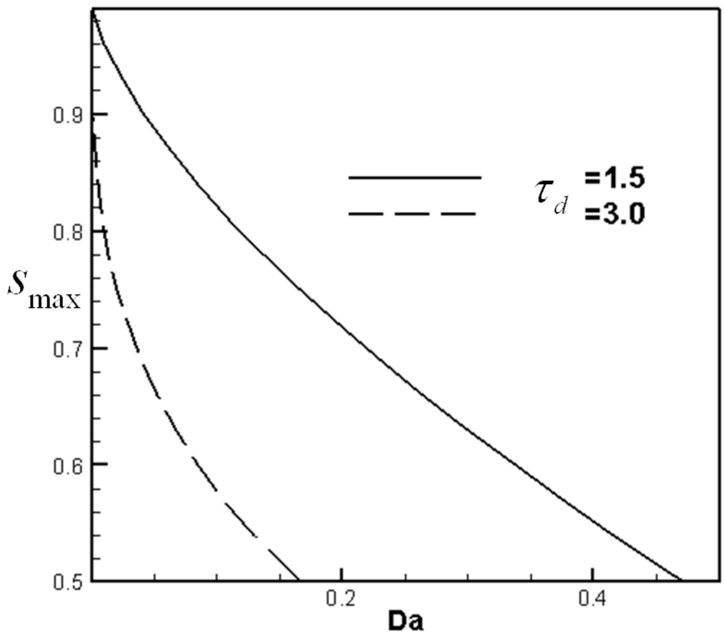

Figure 14: s_{max} as a function of Da under β of 0.5, τ_d of 1.5, τ_a of 2.5, V_0 of 2.75 V and V_{cut} of 2.0 V.

2.6 Charge Capacity

Charge capacity is an important parameter that characterizes battery performance. For a constant discharge current density, one can have

$$\mathrm{Q} = \int_0^{\mathrm{t_{max}}} \mathrm{I\ dt} = \mathrm{It_{max}} \qquad [40]$$

where $\mathrm{t_{max}}$ is the discharge duration of the battery till the cut-off voltage, given by Eq. [25],

$$t_{max} = \frac{n\delta F\rho_{prod}}{\mathrm{IM_{prod}}} \mathrm{s_{max}\varepsilon_0} \qquad [41]$$

Then,

$$Q = \frac{n\delta F \rho_{prod}}{\mathrm{M_{prod}}} \mathrm{s_{max}} \varepsilon_0 \qquad [42]$$

Figure 15 shows the comparison of discharge capacity between the prediction and the experimental. The ACRF002 case includes ACRF002-1123K and ACRF002-1273K. The ACRF003 case includes ACRF003-1073K and ACRF003-1123K. In KC and CKC experiments, the discharge current densities are 0.2 $\mathrm{mA/cm^2}$ and 0.05 $\mathrm{mA/cm^2}$. The carbon case includes 40% carbon and 60% carbon. More details are shown in Table 6. Another set of comparison is also showed in Table 7 and Figure 16.

Table 6. Battery cell information. (Mirzaeian & Hall, 2009; Ren et al., 2011; Younesi et al., 2011)

Cathode carbon	Porosity	Active carbon (Wt%)	Measured Capacity (mAh/g)	Rate	Binder	Electrolyte
ACRF002-1123K	1.320 cm^3/g	-	630	20 mA/g	Kynar	1 M LiPF6 PC
ACRF002-1273K	1.282 cm^3/g	-	740	20 mA/g	Kynar	1 M LiPF6 PC
ACRF003-1073K	1.200 cm^3/g	-	528	20 mA/g	Kynar	1 M LiPF6 PC
ACRF003-1123K	1.336 cm^3/g	-	880	20 mA/g	Kynar	1 M LiPF6 PC
KC	91%	90%	761 430	0.2 mA/cm^2 0.5 mA/cm^2	PTFE	0.2 M LiTriflate PC:TFP (7:3)
CKC	87%	90%	817 597	0.2 mA/cm^2 0.5 mA/cm^2	PTFE	0.2 M LiTriflate PC:TFP (7:3)
40% C	0.121 cm^3/g	40%	306	80mA/g	Kynar	1 M LiPF6 PC
60% C	0.140 cm^3/g	60%	615	80mA/g	Kynar	1 M LiPF6 PC

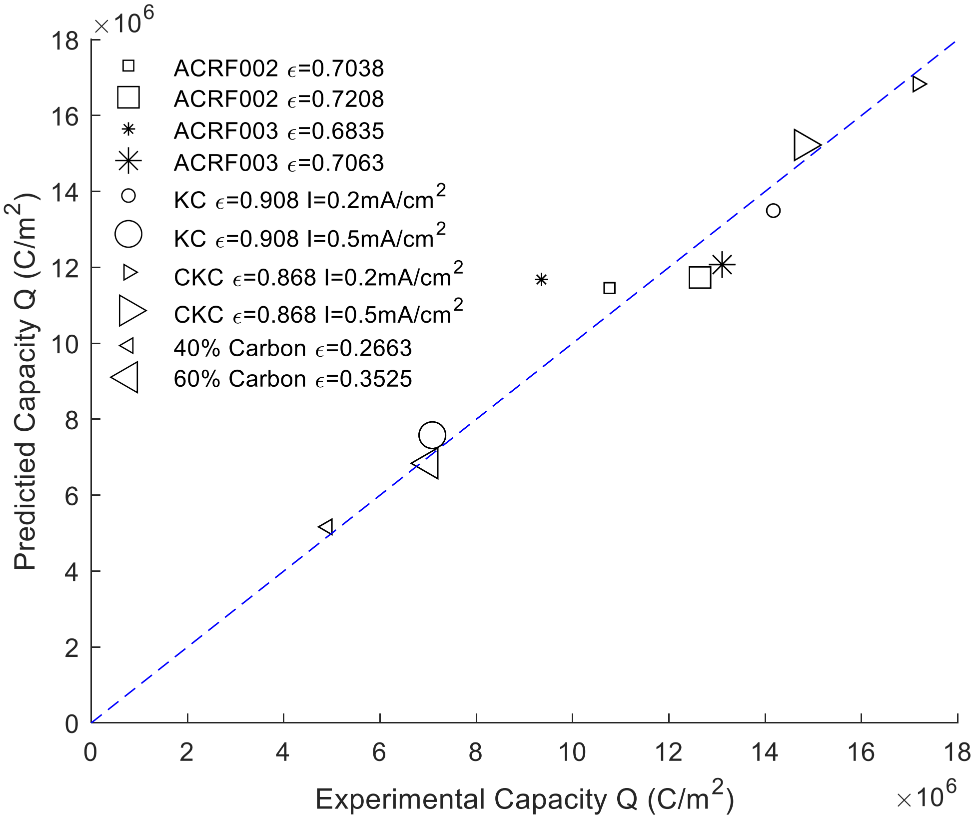

Figure 15: Comparison between the predicted and experimental capacities. Battery information are listed in Table 6.

Table 7. Battery cell information.

Cathode carbon	Cathode density (g/cm^3)	Porosity	Active carbon (Wt%)	Measured Capacity (mAh/g)	Rate (mA/cm^2)	Binder	Electrolyte
Raven 760	0.848	56%	50%	412	0.05	Kynar	1M LiPF6 PC:DME (1:1)
Raven 890	0.811	58%	50%	466	0.05	Kynar	1M LiPF6 PC:DME (1:1)
Raven 22	0.822	58%	50%	405	0.05	Kynar	1M LiPF6 PC:DME (1:1)
ABG1010	0.987	49%	50%	300	0.05	Kynar	1M LiPF6 PC:DME (1:1)

Super P	0.401	79%	50%	1944	0.05	Kynar	1M LiPF6 PC:DME (1:1)
SAB standard	0.380	81%	80%	1950	0.05	PTFE	1m LiTriflate DOL:DME (1:1)
SAB low density	0.213	90%	80%	3300	0.05	PTFE	1m LiTriflate DOL:DME (1:1)
MCMB	1.268	39%	76%	12.2 66.7	0.02 0.01	Kynar	1m LiTriflate DOL:DME (1:1)

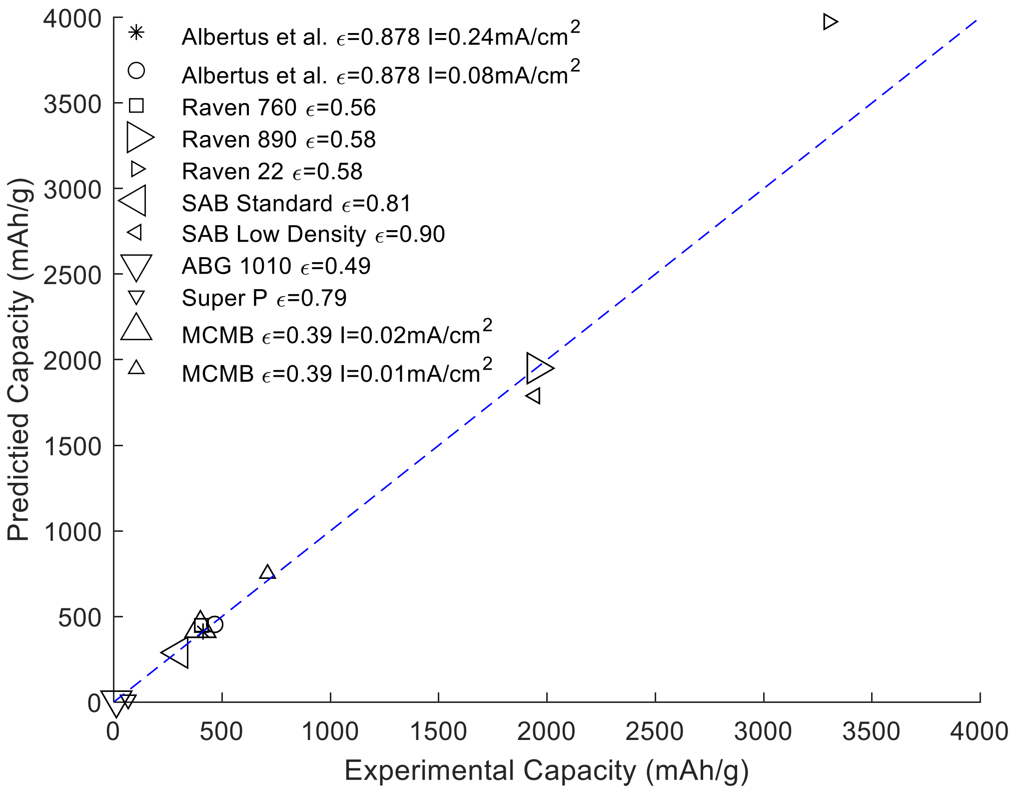

Figure 16: Comparison between the predicted and experimental capacities. The details of the cells are shown in Table 7.

2.7 Energy Capacity

Energy capacity is defined as the energy produced during discharging and can be obtained by integrating the power over time. For a constant current density, one will obtain,

$$u = IV_0\, t_{max} + I\int_0^{t_{max}} \Delta\eta\, dt \tag{43}$$

Substituting t_{max} in Eq. [43] will yield,

$$u = V_0 \frac{n\delta F\rho_{prod}}{M_{prod}} S_{max}\varepsilon_0 + I\int_0^{t_{max}} \Delta\eta\ dt \tag{44}$$

The integral term on the right can be rewritten as,

$$I\int_0^{t_{max}} \Delta\eta\, dt = I\int_0^{t_{max}} \frac{RT}{(1-\beta)F}\left[\tau_a \ln(1-s) + (1-\beta)\ln(1 - Da\frac{3}{4}\frac{1}{(1-s)^{\tau_d}})\right] dt \tag{45}$$

Given that

$$dt = \frac{n\delta F\rho_{prod}\varepsilon_0}{IM_{prod}} ds \tag{46}$$

One will further obtain

$$I\int_0^{t_{max}} \Delta\eta\, dt = \frac{RTn\delta\rho_{prod}\varepsilon_0}{M_{prod}(1-\beta)}\int_0^{s_{max}} \tau_a \ln(1-s) + (1-\beta)\ln(1 - Da\frac{3}{4}\frac{1}{(1-s)^{\tau_d}})\ ds \tag{47}$$

Because the voltage loss leads to capacity decrease, one can express the energy capacity as below,

$$u = u_0 - \Delta u_a - \Delta u_{O2} \tag{48}$$

where $u_0 = V_0 \frac{n\delta F\rho_{prod}}{M_{prod}} s_{max}\varepsilon_0$, $\Delta u_a = -\frac{RTn\delta\rho_{prod}\varepsilon_0}{M_{prod}(1-\beta)}\int_0^{s_{max}} \tau_a \ln(1-s)ds = \frac{RTn\delta\rho_{prod}\varepsilon_0}{M_{prod}(1-\beta)}[s_{max} + (1-s_{max})\ln(1-s_{max})]$, and $\Delta u_{O2} = -\frac{RTn\delta\rho_{prod}\varepsilon_0}{M_{prod}(1-\beta)}\int_0^{s_{max}}(1-\beta)\ln(1-Da\frac{3}{4}\frac{1}{(1-s)^{\tau_d}})\ ds$.

It will be extremely difficult to extract analytic solution from the above integral for Δu_d. However, experimental data show the voltage loss associated with oxygen transport and precipitates is only important in the very short time near the cut-off voltage. Thus, approximate solution can be achieved by neglecting Δu_{O2}, to be presented in the next section.

Figure 17 plots the two energy losses in Eq. [48] for 0.08 mA/cm^2 and 0.24 mA/cm^2 in the validation of Figure 8. The dash line denotes the loss due to the electrode passivation and surface loss. The dash-dot line represents the loss due to the oxygen transport resistance. It can be seen that Δu_d is much smaller than Δu_a in the cases of study, in which one can neglect the former loss in energy analysis.

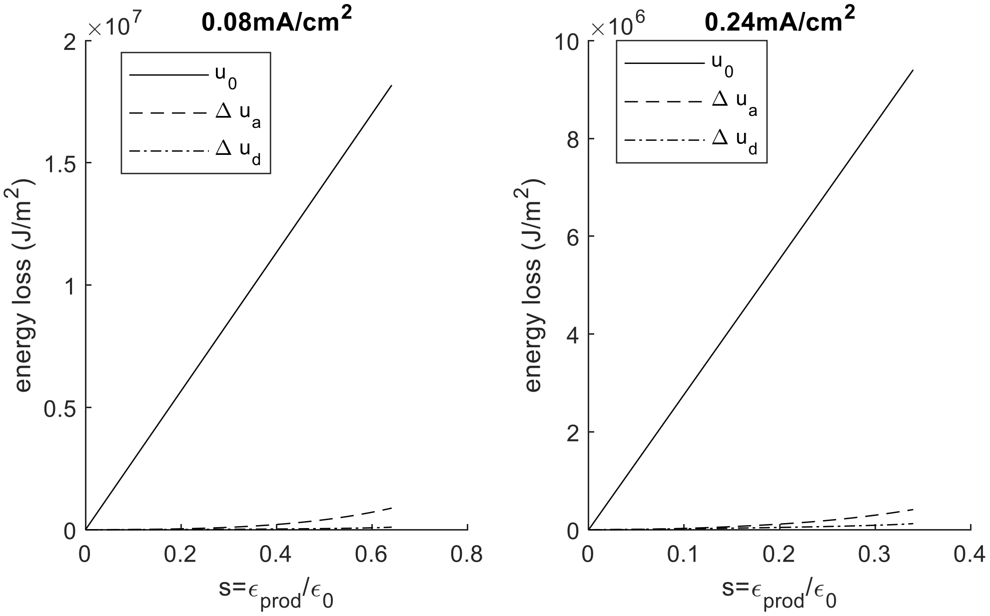

Figure 17: Two energy losses as a function of s in Eq. [48] in the validation of Figure 8. The solid line represents u_0 as a reference. The u_a arises from electrode passivation and surface reduction. Δu_d is caused by oxygen transport clogging.

2.8 Summary

In this chapter, we analyzed the oxygen transport, oxide precipitate growth mode, discharge voltage loss, and a few capacity-related parameters in the air cathode of Li-air batteries. The spatial variations of important quantities including temperature, species concentrations, and phase potentials were formulated and related to a dimensionless parameter, Da. Specially, the oxygen concentration variation is found equal to Da; and a small Da can be designed to achieve nearly uniform distributions of these quantities. The 1-D oxygen transport in cathodes was discussed, along with its profiles obtained and compared under various conditions. A model was proposed to evaluate the voltage loss due to the oxygen transport resistance arising from oxide accumulation, indicating that the precipitate can greatly influence the oxygen profile under a large Da, e.g. Da>0.04. An approximation model was formulated to evaluate the discharge voltage loss due to oxide precipitation, showing acceptable agreement with experimental data. Furthermore, analytical formula were developed to explicitly express the maximum volume fraction of oxide precipitate s_{max}, which is closely related to the battery energy density, as a function of a few parameters including τ_a, τ_d, and Da. Plots were presented to display the relationships. Approximate solutions were obtained to estimate the discharge voltage, the maximum volume fraction of insoluble precipitates, charge capacity, and energy capacity. Two regimes were defined to identify the dominant mechanisms of the voltage loss. It was found that the approximate solutions of s_{max} are in a close agreement with the numerical solution from iterative methods with errors less than 8% for Regimes 1 and 2. Further, the approximate solutions of energy capacity loss were obtained. The model analyses were extensively validated against experimental data. The derived analytical formula can be applied for electrode optimization through designing pore structure (porosity and tortuosity), surface area, electrolyte composition, and operation condition.

Chapter 3: Surface Coverage Model: Experimental Validation

This chapter presents a fundamental study on the precipitate formation/morphology and impact of discharge precipitates in Li-air batteries and compares the voltage loss with two Li-air battery models, namely a film-resistor model and surface coverage model.

3.1 Introduction

Lithium compounds Li_2O, Li_2O_2, and Li_2CO_3 are typical discharge products, and extremely low in electric conductivity as indicated by their bandgaps (Li_2O: 7.44eV, Li_2O_2: 5.12eV, and Li_2CO_3: 8.83eV; materials of bandgap >3eV are good insulator) (Albertus et al., 2011). Because of their low solubility in most nonaqueous electrolytes, discharge products precipitate at local reaction sites. Albertus et al. indicated that precipitate exists in thin film that covers the reaction surface, resisting electron transport for electrochemical reactions. Viswanathan et al. (2011) designed a reversible redox couple to investigate the precipitate's resistance and proposed a metal-insulator-metal charge transport model to predict the electrical conductivity of the precipitate film. Discharge operation was shut down as the film thickness reaches approximately 5 nm to 10 nm. Wang and coworkers indicated that the insoluble product precipitation is similar to ice formation in the fuel cell's cathode during subfreezing operation (Wang, 2012; Mishler et al., 2012; Wang 2015), in which ice first nucleates at selected sites, followed by film formation. They elucidated several precipitate growth modes and proposed a coverage model for electrode passivation. Two major mechanisms of voltage loss due to surface coverage and oxygen transport resistance, respectively, were analyzed and compared (Wang, 2013; Wang 2007). Because the precipitates are physically deposited inside the cathode electrode, the electrode structure, including porosity, carbon particle morphology, and tortuosity, greatly influence the voltage loss due to the precipitate accumulation (Wang et al., 2015). Xiao et al. (2010) investigated the impacts of carbon microstructure and loading, and found that the cathode capacity increases with the carbon material's mesopore volume. Zhang et al. (2010) employed galvanostatic discharge, polarization, and AC-impedance techniques, showing that the discharge performance is determined mainly by air cathodes. Mirzaeian and Hall (2009) studied the porosity, pore structure, carbon's morphology and surface area of the cathodes, and found that the battery performance is influenced by these parameters. Yang et al. (2009) fabricated bimodal-mesopore cathodes using nanocasting technique, and achieved about 40% capacity increase comparing with commercial carbon black electrodes. Mitchell et al. used hollow carbon fibers of 30 nm diameters in the cathodes (Mitchell, 2011), and indicated that Li oxides grew as nodules first and later developed into toroid. Griffith et al. (2015) observed Li oxides form typical 'toroidal' particles at low discharge rates, and exhibit needle-like shapes for high rates, instead of the nano-sheets or compact films. Popular reported morphologies of insoluble precipitates include toroid shape (Black et al., 2012; Zhai et al., 2013), film formation (Albertus, 2011; Viswanathan et al., 2011), and amorphous morphology (Fan et al., 2013; Yilmaz et al., 2013). Studies showed precipitate deposits may reach 1-10 μm in their size (Yang et al., 2014; Zhai et al., 2014).

In physical modeling, precipitate's impacts need to be accounted for as one major mechanism of voltage loss. Direct observation of film formation at planar surfaces indicated a film resistor model is suitable to describe associated voltage loss (Albertus et al., 2011; Wang, 2012). Wang proposed a surface coverage model for general electrodes including porous cathodes, following the approach in subfreezing operation of PEM fuel cell (Wang, 2012; Mishler et al., 2012). In addition, Wang and Cho (2015) indicated that discharge precipitates likely alter the oxygen transport network's tortuosity in the cathode. In this paper, an experimental study was carried out to compare with the model prediction and to investigate the precipitate's morphology. To exclude the voltage loss associated with oxygen transport and precipitate formation (Wang & Cho, 2015), Toray® carbon cloth, which contains approximately planar reaction surface with large pore's size and volume, was selected as the battery cathode. SEM and XRD were employed to analyze the precipitate's morphology and composite for comparison with model prediction. Both film-resistor model and coverage model were used to predict the discharge voltage behaviors.

3.2 Experimental

The experimental Li-air batteries were self-designed to integrate a carbon-cloth cathode and operate with ambient oxygen, see Figure 18. The cell consists of two aluminum plates as the outer case, two plastic plates as the inner case, and O-ring in the middle to build an enclosure for the anode, membrane separator, and cathode. The upper aluminum and plastic plates have oxygen window in the center, permitting ambient oxygen to diffuse and dissolve into electrolyte. The working components include a Lithium (99.9% trace metals basis, Aldrich) anode, PTFE membrane separator (047022B, MS), and a single piece of carbon cloth (ELAT-H, FuelCellsEtc) as the cathode with an active area of 1 cm x 1 cm. The anode and cathode were placed on a copper wire and Nickel mesh, respectively, which connect to the out-circuit. The electrolyte used

DME (anhydrous, 99.5%, Sigma-Aldrich) as the solvent and 1 M Lithium bistrifluoromethanesulfonimidate ($CF_3SO_2NLiSO_2CF_3$, 99.95% trace metals basis, ALDRICH) as conducting salt. The cells were assembled in an argon-filled glove box.

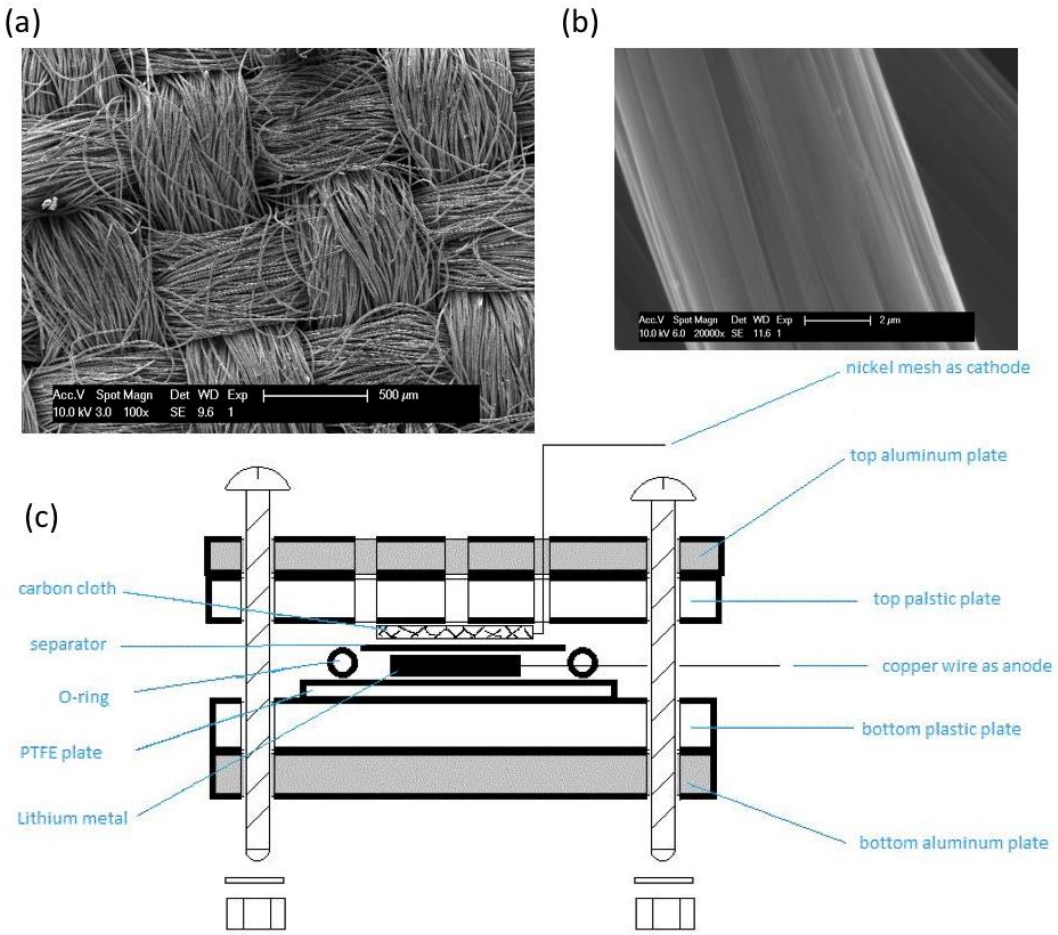

Figure 18: (a) Carbon cloth cathode; (b) Fiber morphology; and (c) Experimental setup for the Li-air battery. (Wang et al., 2017)

The cathode solid structure is plain carbon cloth (ELAT-H, FuelCellsEtc) and the fibers are woven together without any catalyst and binder, see Figure 18. It has a thickness around 400 μm and overall density of 13 mg/cm^2 with a porosity of around 80%, a carbon content of 99.5% in fibers, and a mean pore size around 20 μm. The morphology of the constituent fibers can be assumed cylindrical with a diameter around 7 μm, see Figure 18 (b). The through-plane electric conductivity is 0.1 $m\Omega \cdot cm^2$. The pore network's tortuosity is about 1.11 through experimental fitting (Wang et al., 2013). Table 8 documents the physical properties of carbon cloth cathode and experimental parameters.

Table 8. Experimental and modeling parameters.

Experimental Parameter	Value/description
The active area of Li-air battery	$1 \times 1\ cm^2$
PTFE membrane separator/cathode thickness	150/406 μm
Electrolyte	DME+1M $CF_3SO_2NLiSO_2CF_3$
Fiber radius of cathode, r_f (Wang et al., 2013)	3.5 μm
Cathode mean pore size (Wang et al., 2013)	~20 μm
Cathode porosity, ε_0	0.8
Cathode tortuosity (Wang et al., 2013)	1.11
Cathode through-plane conductivity	0.1 $m\Omega \cdot cm^2$
Current density I	0.03, 0.06 and 0.1 mA/cm^2
Operating temperature	25 ℃
Operating pressure	1 atm
Model Parameter	
The specific area ratio, A^*	30
Oxygen diffusivity and solubility in electrolyte (Wang, 2012)	$4 \times 10^{-5}\ cm^2/s$ and 0.00876 in DME with of 1 M Li^+
Discharge product (Li_2CO_3) molecular weight, M_{prod}	0.07389 kg/mol
Discharge product(Li_2CO_3) density, ρ_{prod}	2,110 kg/m^3
a_0 in the film-resistor model (Wang, 2012)	$1.0 \times 10^{15}\ \Omega \cdot m$
c_1 and c_2 in the film-resistor model	$4.7 \times 10^7\ m^{-1}$ and $3.6 \times 10^{-7}\ m$

B_1, B_2, and s_0 in the coverage model	2.5, 8, and 0.2
$\varepsilon_{prod,max}$ in the coverage model	0.0035, 0.009, and 0.0425 for 0.1, 0.06, and 0.03 A/cm^2, respectively

*Estimate

Battery testing was performed galvanostatically under room temperature using an electrochemical testing platform (Princeton Applied Research, PARSTAT MC, PMC 500/HI). Before measurement, the assembled cell was rested in dry ambient oxygen for at least 120 minutes. Each measurement started with a 30 min recording of the open circuit potential to ensure equilibrium in the cell, followed by applying a constant discharge current. Three current densities were chosen for experiment, including 0.03, 0.06 and 0.10 mA/cm^2. These current densities are similar to those operated on planar electrodes (Albertus et al., 2011). For example, given the specific area of 30 for carbon cloth electrode, the current density of 0.1 mA/cm^2 in the present study is equivalent to ~3.33 $\mu A/cm^2$ for a planar electrode, which is similar to that of 3.76 $\mu A/cm^2$ in the study (Albertus et al., 2011). Discharge products were characterized by the Rigaku SmartLab X-ray Diffractometer (Cu-Kβ source, 40kV, 44 mA) and SEM (Philips XL-30 FEG SEM). All the SEM images were taken at the side of cathode and current collector.

3.3 Film-Resistor Model

Assuming the precipitates form thin film covering the reaction surface, the film becomes a resistor hampering electron transport and causing voltage loss, see Figure 19. The precipitate film grows usually around 10-100 nm in thickness before shutting down discharge operation.

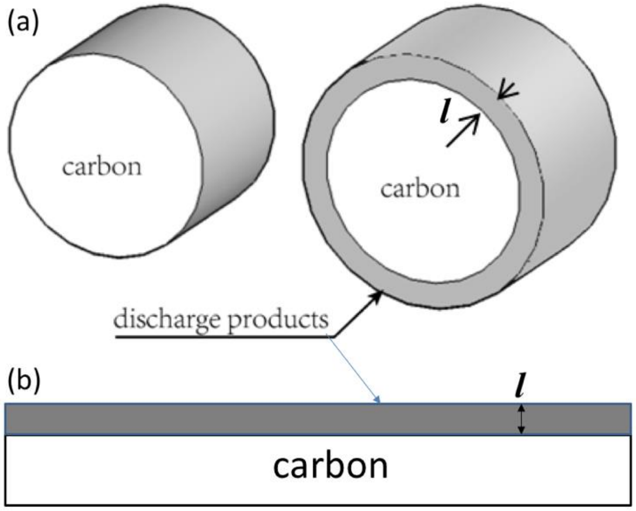

Figure 19: Thin film growth mode of precipitates on: 1.) cylindrical fiber; and 2.) planar surface

For the carbon cloth cathode, the film grows at the cylindrical surface of fibers with its thickness l given by (Wang, 2012):

$$l = \left(1 - \sqrt{\frac{\varepsilon_f + \varepsilon_{prod}}{\varepsilon_f}}\right) r_f \qquad [49]$$

As the discharge operation proceeds, both the volume fraction of discharge product ε_{prod} and film thickness l increase, raising the reaction resistance and voltage loss. The method of formulating film thickness was employed for a spherical reaction surface (Albertus, 2011). For the carbon cloth cathode, its fiber radius r_f is around 3.5 μm ($\gg l$), thus the deposit film can be approximated by the planar-film growth mode (Wang, 2012), in which the film thickness is directly determined by the discharge product volume:

$$Al = \frac{QM_{prod}}{nF\rho_{prod}} \qquad [50]$$

Where A denotes the specific area ratio. The coulomb of discharge Q per active reaction area (mAh/cm^2) is given by:

$$Q = \int_0^t I\,dt \xrightarrow{I=constant} Q = I \times t \qquad [51]$$

The above equation assumes that the film is firmly packed without any pores and all the discharge products were precipitated in the film. The electric resistance R_{prod} is determined by the thickness l, empirically given by (Albertus, 2011; Wang, 2012):

$$R_{prod} = A_0 l \exp[c_1(l - c_2)] \qquad [52]$$

where c_1 and c_2 are constant. The voltage loss associated with the film formation is then given by:

$$\Delta\eta = -i_n R_{prod} = -\frac{I}{A} R_{prod} \qquad [53]$$

where I represents the average current density and i_n denotes the current density across the discharge film in the direction normal to the reaction surface. The film-resistor model was compared with experimental data and showed acceptable agreement (Albertus, 2011; Wang, 2012).

3.4 Surface Coverage Model

The resistance of electron access to electrochemical reaction caused by insoluble discharge products can be evaluated through reduction in the active reaction surface area, a. For porous electrodes, the following power law is frequently adopted to describe the reduced surface area (Wang, 2012; Wang et al., 2013):

$$a = a_0(1 - s)^{\tau_a}$$
$$s = \frac{\varepsilon_{prod}}{\varepsilon} \qquad [54]$$

where s represents the volume fraction of insoluble discharge products in the pore space, and τ_a is the exponent coefficient that measures the degree of insoluble products' effect on the active surface area. The semi-empirical relationships were proposed to describe the coverage coefficient (Wang et al., 2015) as Eq. [27]. In this equation, the maximum value of s is assumed to be unity, i.e. the precipitates occupy the entire pore space. In the present study, the porosity and pore size are large, and the reaction surface area is small. As a result, the maximum of s is much smaller than 100%. We then modify the reduced surface area and the coverage coefficient in the above two equations by defining the volume fraction of insoluble discharge product, *s*, as below (instead of that in Eq. [54]):

$$s = \frac{\varepsilon_{prod}}{\varepsilon_{prod,max}} \qquad [55]$$

where $\varepsilon_{prod,max}$ represents the maximum volume fraction that discharge product may occupy under the operating condition. It is determined by multi-factors including the number of activation sites, surface area, and discharge product morphology. In design of high energy density battery, it is desirable that $\varepsilon_{prod,max}$ is close to porosity ε.

As discharge proceeds, precipitate accumulates, narrowing the pore network and thus increasing oxygen transport resistance and associated voltage loss. In the present cathode, this voltage loss is anticipated to be unimportant, which can be justified by evaluating the Damköhler number (Da) (Wang et al., 2015) as Eq. [8]. A current density of 0.1 mA/cm^2 or 1 A/m^2, δ of 0.4 mm, ε_0

of 0.8, $\tau_{d,0}$ of 1.1, and D_{O2} of $4 \times 10^{-9}\ m^2/s$ yield Da~0.03 for $C_{O2,\delta}$ of 5 mol/m^3 (5 mM), clearly indicative of sufficiently fast mass diffusion relative to the reaction kinetics under the discharging current. Even precipitate occupies 75% of the pore space, i.e. the effective porosity becomes 0.2, Da is around 0.14 under the same tortuosity, indicating oxygen supply is sufficient for the reaction. For the lowest current in this experiment, i.e. 0.03 mA/cm^2, Da is around 0.042 for a porosity of 0.2.

To evaluate the voltage loss due to oxygen transport and precipitates, one can adopt Eq. [29] to assess the surface overpotential at the middle depth of the cathode:

$$\Delta\eta_{O2}(y = \frac{\delta}{2}) = \frac{RT}{F}\ln\left(1 - \frac{3Da}{4\varepsilon^{\tau_d - \tau_{d,0}}\left(1 - \frac{\varepsilon_{prod}}{\varepsilon}\right)^{\tau_d}}\right) \qquad [56]$$

An approximate model can then be developed by combining the two voltage losses raised by the surface coverage and oxygen transport when precipitates are present (Wang & Cho, 2013):

$$\Delta\eta = \frac{RT}{(1-\beta)F}\left[\tau_a \ln(1-s) + (1-\beta)\ln\left(1 - \frac{3Da}{4\varepsilon^{\tau_d - \tau_{d,0}}\left(1 - \frac{\varepsilon_{prod}}{\varepsilon}\right)^{\tau_d}}\right)\right] = \Delta\eta_a + \Delta\eta_{O2} \qquad [57]$$

where $\Delta\eta_a$ and $\Delta\eta_{O2}$ represent the voltage loss associated with precipitates due to surface coverage and oxygen transport, respectively.

3.5 Comparison of Model Prediction and Experiment Data

Figure 20 plots the experimental discharging voltage evolution under 0.03, 0.06, and 0.1 mA/cm^2, along with model prediction. The battery output voltage experienced a decreasing trend in general as discharging proceeds, which is typical as observed by other studies (Albertus et al., 2011; Zhang & Read, 2011). In the model prediction, the film-resistor model adopted the parameters similar to Albertus et al. (2011) and Wang (2012), and the coverage model used the same parameters as Wang and coworker. The coverage model prediction shows acceptable agreement with all the experimental data. The voltage loss due to oxygen transport associated with precipitates $\Delta\eta_{O2}$ is plotted in Figure 21, showing that its contribution is small relative to the overall voltage loss and thus is negligible, which is consistent with the Da analysis in Eq. [8]. In addition, the film-resistor model predicts the voltage loss under the highest current density (0.1 mA/cm^2) but fails to match with the other two lower current operations (significantly under-predicts the battery capacities). To explore the reasons for the observed deviation, both SEM and XRD were carried out to disclose the morphology and composition of deposits in the cathode electrodes.

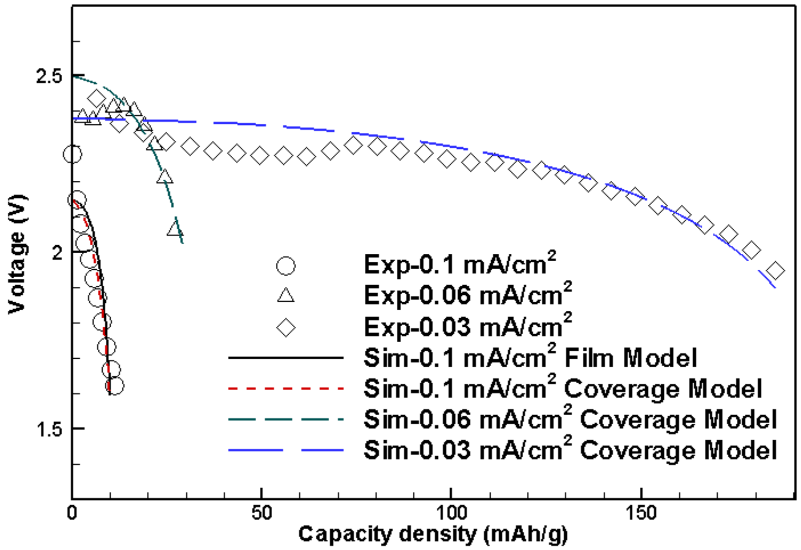

Figure 20: Discharge voltage evolution of Li-air battery and comparison with model predictions. The film-resistor model's prediction considerably deviates from the experimental data under the two low currents, which is not plotted in the figure

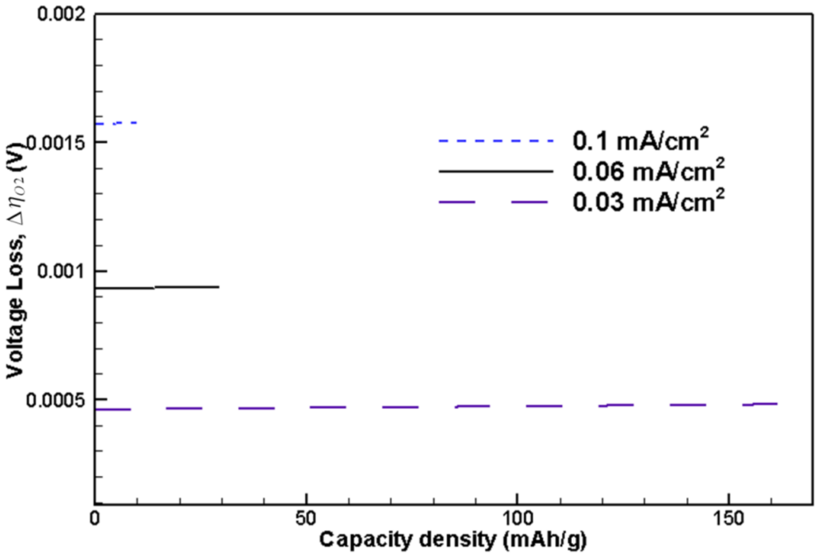

Figure 21: Numerically Predicted $\Delta\eta_{O2}$ in Eq. [57] for the three current densities.

In the imaging, the carbon-cloth cathode was taken out at the end of the discharging operation, gently washed by fresh solvent, and dried in a sealed space. The samples were then imaged using SEM, as shown in Figure 22 (a) for 0.03 mA/cm^2. XRD was performed after the SEM imaging, as shown in Figure 22 (b), and indicated that the white deposit is primarily Li_2CO_3. Some studies indicated that electrolyte decomposition may result in Li_2CO_3 formation (Albertus et al., 2011; Shui et al., 2013). It is also possible that that the direct discharge products in the battery are lithium oxides, which then react with ambient CO_2 to form Li_2CO_3 during testing or imaging. Because both Li oxides and Li_2CO_3 are intrinsic insulator with extremely low conductance to electron transport, their formation at the reaction surface hampers electron transport for the electrochemical reaction, leading to passivation.

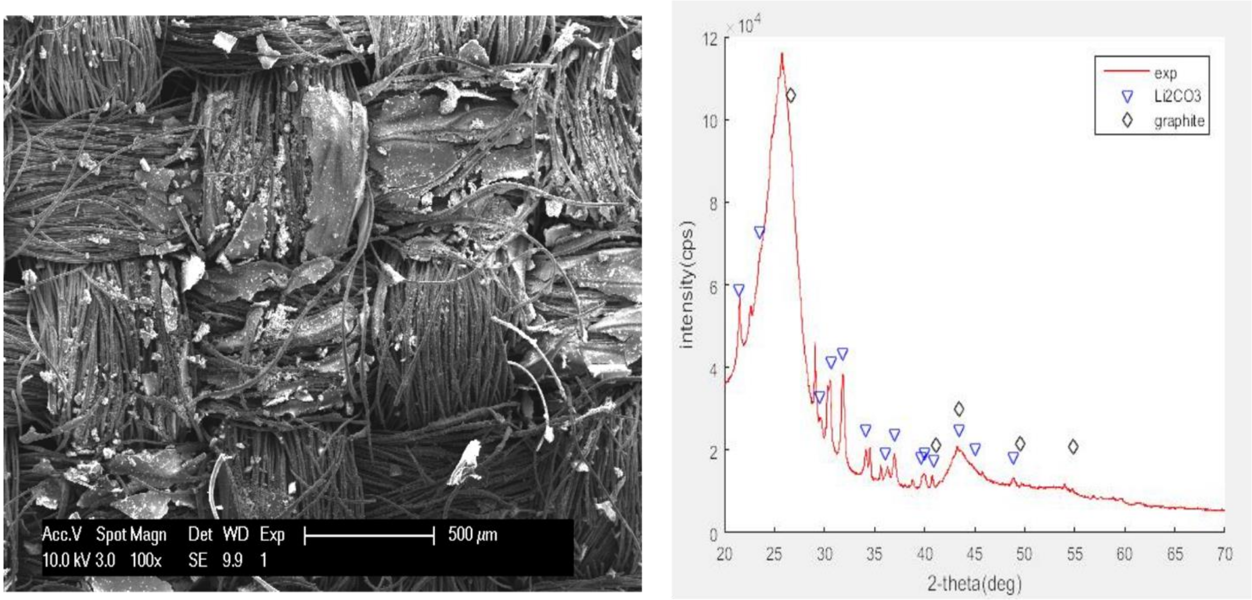

(a) (b)

Figure 22: SEM images and XRD analysis of the cathode with discharge precipitate under 0.03 mA/cm^2

Three morphologies of discharge precipitates are evident in Figure 22 (a): 1) film formation over the fiber's cylindrical surface, see Figure 23; 2.) large aggregates attaching to fibers, see Figure 24; and 3.) small aggregates, see Figure 25. It is clear that the majority of the pore space in the cathode is not clogged by the precipitate and most pores remain open for reactant transport via electrolyte. The precipitate occupied a small fraction of the void space, thus the voltage loss due to the oxygen transport resistance raised by the precipitate formation is unimportant, as shown in the preceding analysis on the Da number and Figure 21. In Figure 23, a thin film clearly develops at the carbon fiber surface, which introduces a barrier to electron transport and yields a voltage drop in the operation. Electron tunneling is one possible mechanism enabling electrons to across the thin insulation layer for the electrochemical reaction. The thin film usually grows about tens of nanometers in thickness depending on operation condition. Similar film formation was observed by Albertus et al. (2011), Viswanathan et al. (2011), Black et al. (2012), Yang et al. (2014), and Yu et al. (2013).

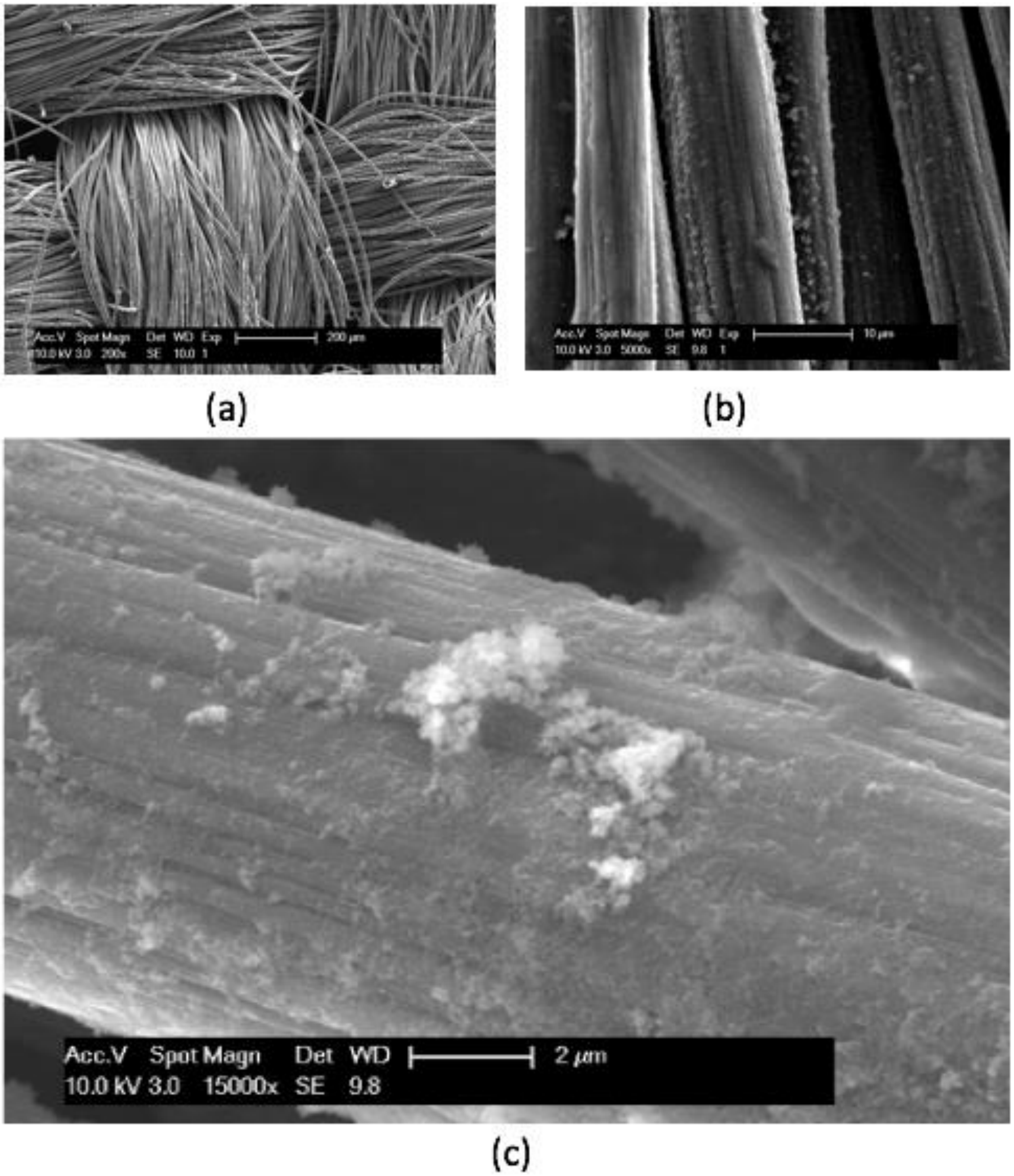

(a) (b) (c)

Figure 23: Film formation of discharge precipitate under 0.03 mA/cm^2

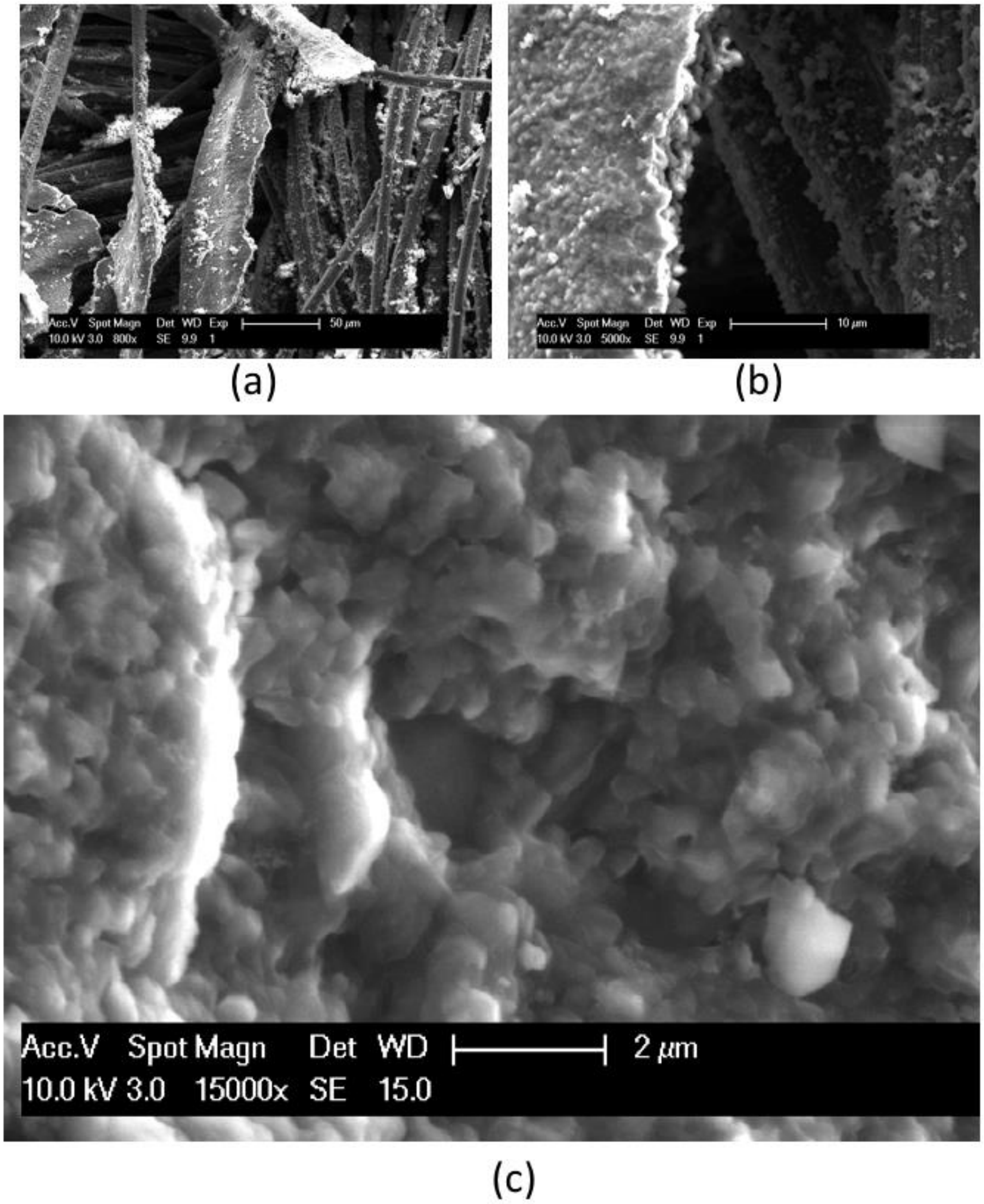

Figure 24: Large aggregate formation of discharge precipitate under 0.03 mA/cm^2

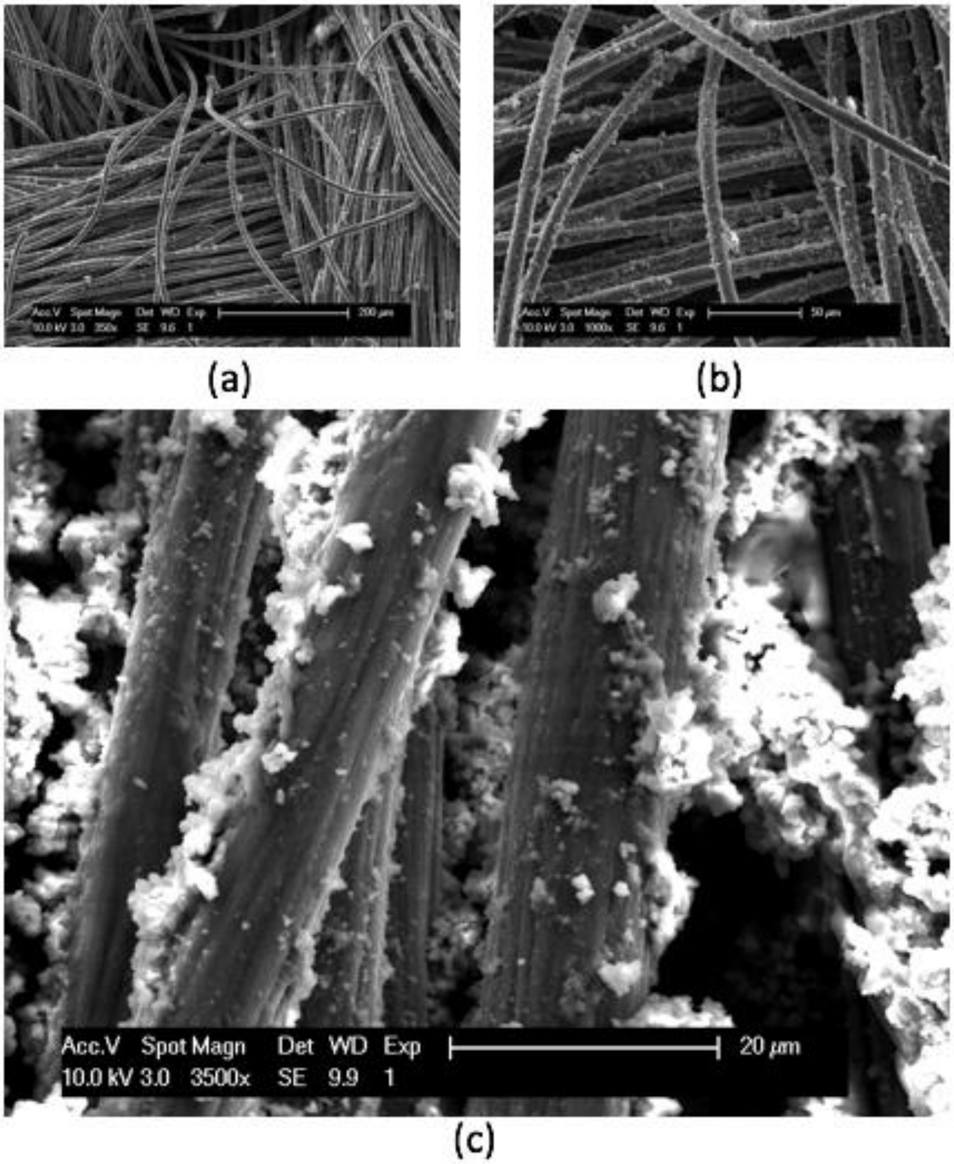

Figure 25: Small aggregate formation of discharge precipitate under 0.03 mA/cm^2

Figure 24 shows formation of large precipitate aggregates which are present near the air side of the cathode. The agglomerates grow around fibers with their size even beyond 10 µm. It is seen that the aggregates consist of many small particles of a dimension around 200-500 nm with grain boundaries. It is difficult to see the morphology of all the small particles, but some exhibit the spherical or toroidal shape. The actual mechanism is unclear for the observed aggregation of the dimension. It is possibly due to the presence of grain boundaries which permit the reactant transport for the electrochemical reaction. The aggregates appear to cover a small area of the cathode, which raise oxygen transport resistance only at local for the present cathode. However, aggregates of the dimension may effectively block oxygen transport in cathodes of small pores, raising voltage loss. Yang et al. (2014), Zhai et al. (2014) and Wang et al. (2015) observed discharge deposits of similar dimension in their studies.

In several locations of cathode, the white discharge deposit exists in relatively small aggregates of approximately 1 μm in size, distributed randomly on the fiber surface, as shown in Figure 25. Similarly, the aggregates appear to consist of small particles with a dimension around 200-500 nm. Different with the large aggregates, these aggregates are small and unable to surround the fiber perimeter. Similar morphology was observed by Adams et al. (2013), Xia et al. (2014) and Johnson et al. (2014). Their presence appears to have little impacts on oxygen diffusion for the present cathode; but could be significant for cathode pores at nano- or mesoscale.

For the above two morphologies of deposit aggregates, their impacts on voltage loss are not fully understood yet. It is clear that their impacts deviate from the film resistor approach which assumes the precipitate form a thin film which is a resistive layer hampering electron transport. This may be the major reason that the film-resistor model prediction failed to match with the experimental data for 0.03 mA/cm^2 in Figure 20. As to the coverage model, the precipitates' impact is converted to loss of the electrochemical reaction area, following the approach of the ice's effect on PEM fuel cell's voltage loss. The precipitates, in either film or aggregate form, covers certain area of fibers and reaction sites, reducing the electrochemical activity. Therefore, the coverage model shows acceptable match with the experimental data. In addition, it appears that the presence of these aggregates may increase the storage capacity of Li discharge deposit and hence battery capacity. Their presence will affect bulk oxygen transport inside micro- or nano-scale pores.

Figure 26 displays the precipitate of discharge products under 0.06 mA/cm^2, showing that both thin film and toroidal (or partially toroidal) precipitates are present at the fiber surface. The toroidal deposits are small around 1 μm in size. Similar morphology was observed. The amount of the toroidal deposit appears much smaller than the pore space, thus its effect on the oxygen transport polarization is negligible. Similarly, this morphology’s impact on electrode passivation deviates from the film-resistor model, which explains the mismatch with the experimental data in Figure 20. The toroidal deposits on the fiber surface covers the reaction surface and reduces the electrochemical activity, which is accounted by the coverage model. Thus, the coverage model predicts the experimentally observed voltage loss.

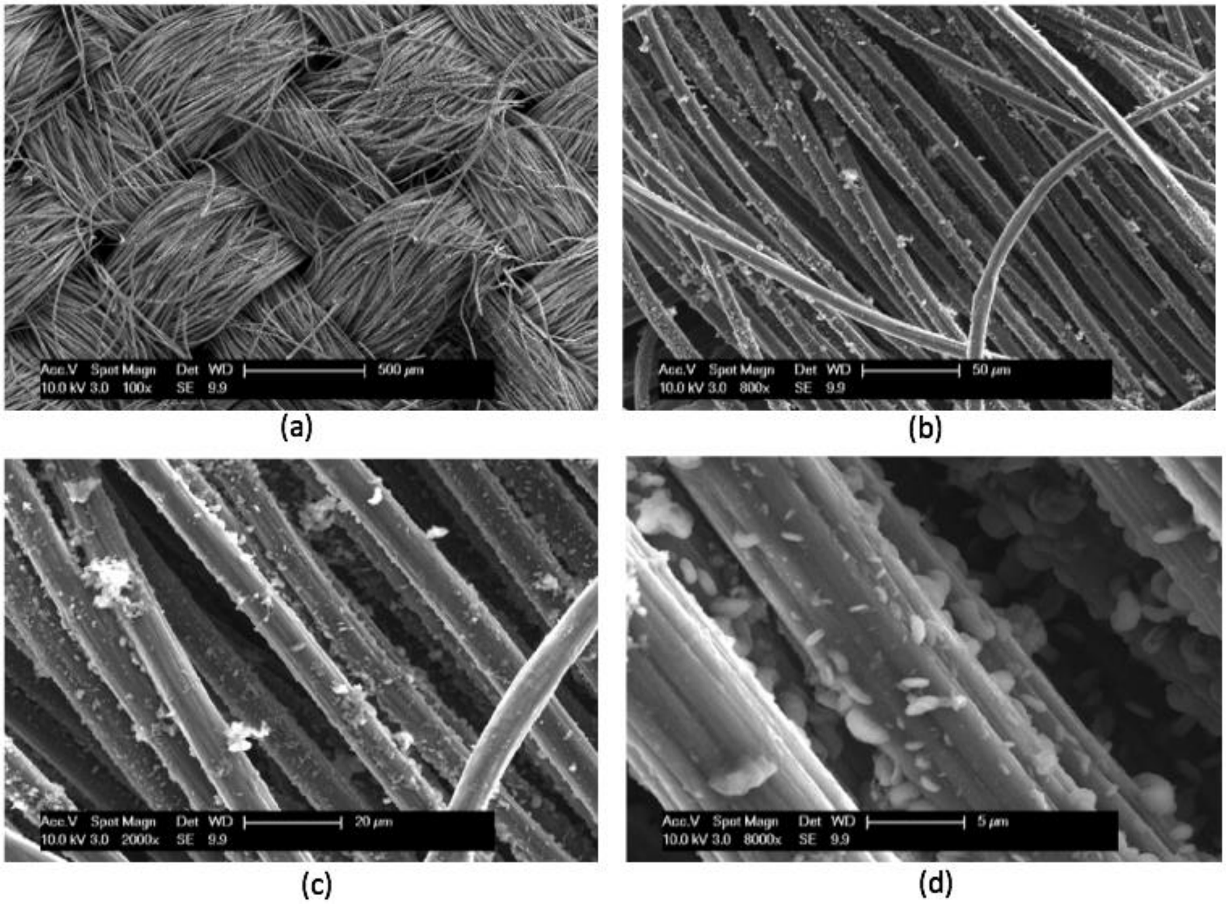

(a) (b) (c) (d)

Figure 26: Film and toroid formation of discharge precipitate under 0.06 mA/cm^2

Figure 27 presents the precipitate under 0.1 mA/cm^2, showing that film formation dominates the morphology of the precipitate. The film appears very thin, tightly covering the fiber surface. The film resists electron transport for the electrochemical reaction, causing electrode passivation. The film-resistor model describes this type of deposit morphology, and thus predicts the voltage evolution under this current. The maximum thickness of the thin film is predicted to be around 40 nm from the model prediction, which is in line with the work of Albertus et al. (2011) and Wang (2012) (~40 nm under the current of 3.76 µA/cm^2 on a planar electrode; in the present work, the current of 0.1 mA/cm^2 is converted to ~3.33 µA/cm^2 equivalent current for a planar surface). For the coverage model, the thin-film formation imposes a surface coverage on the electrochemical reaction sites, reducing the electrochemical reactivity. Thus, the impact of this growth mode of precipitates was captured by the coverage model as well. Similar conclusion was drawn by Wang (2012).

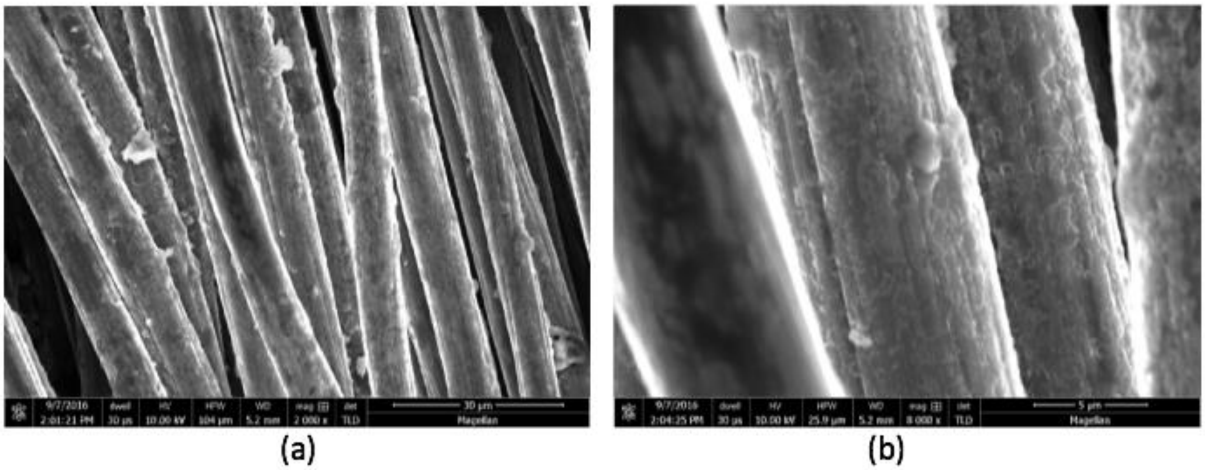

(a) (b)

Figure 27: Film formation of discharge precipitate under 0.1 mA/cm^2

3.6 Summary

In this work, the predictions of two models, namely the film-resistor model and surface coverage model, were compared with experimental data to study voltage loss and elucidated the precipitate morphology's impacts in Li-air battery discharge operation. Acceptable agreement was achieved for the coverage model, while the film-resistor model failed to match with the experimental data for the two low current densities, i.e. 0.03 and 0.06 mA/cm^2. SEM and XRD were employed to explore the observed discrepancy. Several morphologies of discharge deposit were disclosed for the two lower currents, including film formation, large aggregates, small aggregates, and toroidal shapes. The aggregate precipitates were found to be present at a length scale of micrometer and to consist of small nanoparticles around 200-500 nm. Presence of grain boundaries was a possible mechanism for observed aggregation. The impacts of the aggregate and toroidal morphologies on voltage loss deviated from that of film formation, and were attributed as the major reason that the film-resistor model prediction failed to match with the experimental data. For the highest current 0.1 mA/cm^2, thin film formation dominated and the film-resistor model prediction agreed well with the experimental data using the model parameters reported in the literature. The coverage model predicted the experimental data for all the cases because the model accounts for the effects of various morphologies on the electrochemical activity. In addition, it indicated that the voltage loss associated oxygen transport and precipitates was small and negligible in the cases of study.

Chapter 4: Spatial Variations of Discharge Oxides

This chapter will present a study on the spatial variation of discharge precipitate and reaction rate in Li-air battery both theoretically and experimentally: 1.) the reaction variation of local oxygen reduction reaction (ORR) rate is theoretically analyzed, with analytical solutions related to a dimensionless number; 2.) an experimental method is proposed to probe local ORR rate by designing multi-layer cathode. The morphology of insoluble Li compounds at different thickness locations is uncovered by SEM images.

4.1 Introduction

In air cathode, lithium oxides Li_2O, Li_2O_2, and Li_2CO_3 are typical discharge products, and extremely low in electric conductivity. They precipitate at local reaction sites due to their low solubility in major nonaqueous electrolytes. The oxygen reduction reaction (ORR) rate determines the production rate of the Li oxides precipitates and hence their volume fraction at the end of the discharge. Because the pore space that is not utilized to store the final oxides can be reduced to maximize the specific energy, understanding the ORR spatial variation is of practical importance to the cathode design and development.

The current literature is mostly focused on the material and fabrication aspects of cathodes. A few works have been proposed to indicate the spatial variation of reactant concentrations, which influence the local ORR rate. Wang (2012) presented theoretical evaluation on the spatial variations of oxygen, temperature, Li ion, and phase potentials, and demonstrated that a sufficiently thin cathode would yield a uniform ORR rate across the cathode. Wang et al. (2015)

further explored the spatial variation of oxygen as a function of the Da number and obtained the analytical solutions for the oxygen concentration. In addition, Albertus et al. indicated that precipitate exists in thin film that covers the reaction surface, resisting electron transport for electrochemical reactions. They proposed a 1D model following the Li-ion battery approach and predicted spatially varying quantities across the cathode. Williford and Zhang (2009) proposed an interconnected dual pore system (one catalyzed and one non-catalyzed) to improve oxygen transport of the air electrode. The system was analyzed by numerical simulations of finite difference method. Li and Faghri (2012) developed a two-dimensional, transient, and non-isothermal model to investigate on spatial distributions of oxygen, lithium ion, lithium peroxide, and temperature in the carbon electrode. Andrei et al. (2012) presented a model for Li-Air batteries with dual electrolyte using the mass transport and drift-diffusion equations of the electrolyte. They analyzed two regimes of operation: (1) concentration of the electrolyte is smaller than the concentration of saturation of Li+OH in water, and (2) when the electrolyte concentration is more than saturation concentration, considering deposition of reaction product. Sahapatsombut et al. (2013) developed a micro-macro homogeneous mathematical model to determine spatial variation of battery capacity and discharge potential by considering lithium peroxide (Li_2O_2) layer inside the cathode and active surface morphology changing with the Li_2O_2 growth as well as concentrations of oxygen and lithium ion. Yoo et al. (2014) developed a mathematical model in consideration of volume change in Li-Air cell due to metal oxidation in anode and solubility of reaction product in cathode. Moving boundary technique was used to perform their study. The results of this model were validated with experimental results. Sergeev et al. (2015) conducted a numerical study to evaluate pore filling at 100% depth of discharge and cell-level specific energy by considering oxygen diffusion and non-uniform product precipitation at different discharge current densities in different electrolytes. Mayur and Bessler (2017) proposed a two-dimensional model to investigate a lithium-air button cell cathode for five different electrolytes including water, ionic liquid, carbonate, ether, and sulfoxide. They predicted the spatial distributions of oxygen, Li ion, and reaction rate in the cathode with respect to electrode saturation. Wang and Cho (2013) analyzed the spatial variations of major quantities in the cathode, the oxygen concentration profile across the cathode, and the voltage loss caused by the electrode passivation and oxygen transport. They further proposed a 2D model to examine the spatial variations of the ORR reaction across the cathode and along an oxygen supply channel. The mode consists of conservations of species, charges, and energy. The results indicated a large variation in the ORR rate across the cathode, and the variation in the other direction could be significant for thin oxygen supply channels. Nanda at al. (2012) employed neutron tomographic imaging to disclose the three-dimensional spatial distribution of lithium products in lithium-air cathodes. They found a nonuniform lithium product distribution across the electrode thickness, with the lithium species concentration being higher near the edges of the Li-air electrode and relatively uniform in the center of the electrode. They claimed that anomalous behavior is due to the competition between the transport of lithium and oxygen and the accompanying electrochemical kinetics.

In the general context of the ORR, the reaction spatial variation can be raised by the phase potential variation. Wang and Feng (2008) presented analysis on the ORR spatial variation for PEM fuel cell cathode, and identified a dimensionless parameter h, which measures the degree of the ORR spatial variation. They also indicated that high current density, thick electrode, and large ionic resistance will increase the spatial variation. To design more uniform ORR, they proposed the dual-layer and multi-layer configurations with each sublayer of specific composition (Wang & Feng, 2009, 2010). Similar studies were also proposed by Kulikovsky et al. (2012) and Chen et al. (2016).

Though many studies have been proposed to understand the spatial variations of the reaction rate in the cathode, fundamental analysis, analytical solutions and experimental validation are still needed to identify the governing parameters and the correlations to guide cathode design and control. In this paper, we first presented analysis of local reaction rate, and then proposed a novel three-layer cathode battery to experimentally study the spatial variation of discharge Li compound precipitate. Three Toray® carbon cloths were selected as the battery cathode. SEM discloses the precipitate's morphology at different locations. High-precision weight scale was employed to evaluate the mass of precipitates and hence the average local reaction rate in each sublayer of the cathode.

4.2 Experimental

The experimental Li-air batteries were self-designed to integrate the three-layer carbon-cloth as the cathode and operate with ambient oxygen, see Figure 28. The cell consists of two aluminum plates as the outer case, two plastic plates as the inner case, and O-ring in the middle to build an enclosure for the anode, membrane separator, and cathode. The upper aluminum and plastic plates have oxygen window in the center, permitting ambient oxygen to diffuse and dissolve into electrolyte. The working components include a Lithium (99.9% trace metals basis, Aldrich) anode, PTFE membrane separator (047022B, MS), and a single piece of carbon cloth (ELAT-H, FuelCellsEtc) as the cathode with an active area of 1 cm x 1 cm. The anode and cathode were placed on a copper wire and Nickel mesh, respectively, which connect to the out-circuit. The electrolyte used DME (anhydrous, 99.5%, Sigma-Aldrich) as the solvent and 1 M Lithium bistrifluoromethanesulfonimidate ($CF_3SO_2NLiSO_2CF_3$, 99.95% trace metals basis, ALDRICH) as conducting salt. The cells were assembled in an argon-filled glove box.

The cathode solid structure is plain carbon cloth (ELAT-H, FuelCellsEtc) and the fibers are woven together without any catalyst and binder, see Figure 28 (a). It has a thickness around 400 μm and overall density of 13 mg /cm^2 with a porosity of around 80%, a carbon content of 99.5% in fibers, and a mean pore size around 20 μm. The morphology of the constituent fibers can be assumed cylindrical with a diameter around 7 μm. The through-plane electric conductivity is 0.1 mΩ cm^2. The pore network's tortuosity is about 1.11 through experimental fitting.

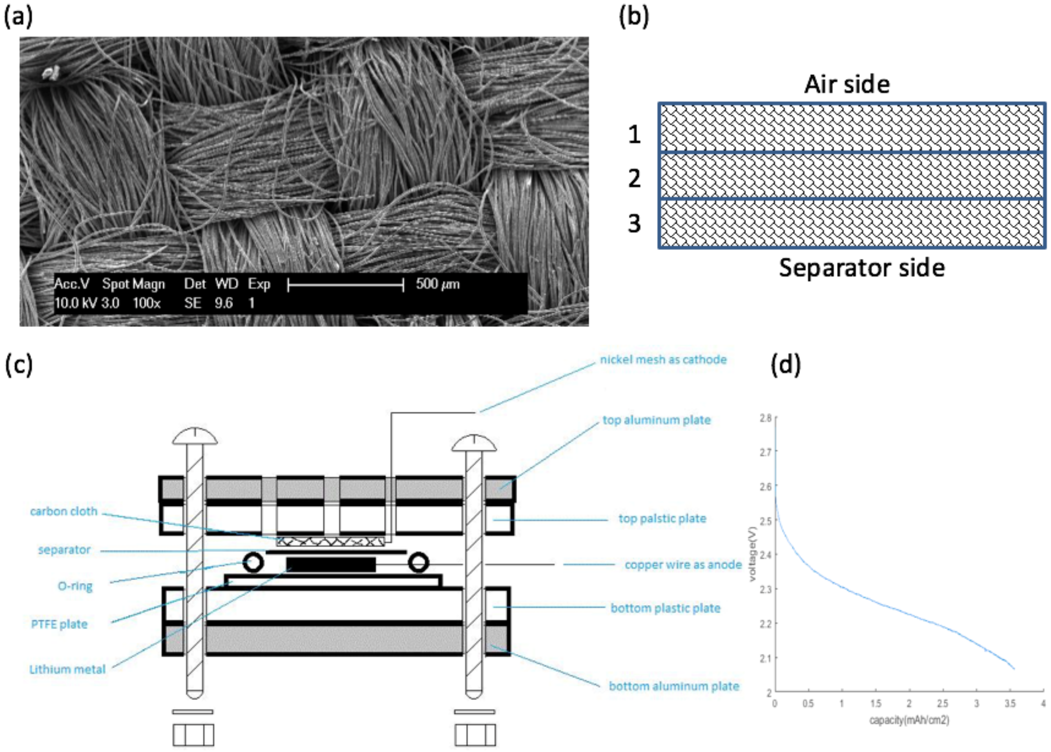

Figure 28: (a) Carbon cloth cathode, (b) three-layered cathode, (c) experimental setup for the Li-air battery, and (d) the discharge voltage under 0.01 mA/cm^2.

Battery testing was performed galvanostatically under room temperature using an electrochemical testing platform (Princeton Applied Research, PARSTAT MC, PMC 500/HI). Before measurement, the assembled cell was rested in dry ambient oxygen for at least 120 minutes. Each measurement started with a 30 min recording of the open circuit potential to ensure equilibrium in the cell, followed by applying a constant discharge current of 0.10 mA/cm^2. The cathode was dissembled at the end of the operation when the cut off voltage was reached. The samples of each layer were then taken out, and exposed to dry ambient air for sufficient time and analyzed for their weight addition and the precipitate morphology. Philips XL-30 FEG SEM was employed take the precipitate's images at the surface of Layer 1 and the Layer 1-2 and Layer 2-3 interfaces, see Fig. 1 (b). A high-resolution weight scale (Denver Instrument TB-215D) of a resolution 0.01 mg was used to evaluate the mass of precipitate in each sublayer.

Figure 28 (d) plots the experimental discharging voltage evolution. The battery output voltage experienced a decreasing trend in general as discharging proceeds, which is typical as observed by other studies. In general, the first gradual decrease arose from the surface coverage of the discharge precipitate, as a result of reaction surface reduction and electrode passivation; the second stage of rapid drop is due to the oxygen transport polarization, caused by the oxygen diffusive passage blockage by precipitate. The cathode substrate is the carbon cloth of a large porosity (~0.88), thus the second stage is not evident.

4.3 Analysis of Spatial Variation

The discharge reaction rate can be approximated expressed by the Tafel equation as Eq. [11]. In the equation, the surface overpotential η is determined by the local phase potentials and equilibrium potential U_0 as Eq. [12]. It considers no precipitates deposited at the reaction surface. For a sufficiently small Da, the spatial variations of temperature, phase potentials, oxygen concentration, and C_e are negligibly small, thus the exchange current density j_c can be treated uniform across the entire thickness of the air cathode. To evaluate local reaction rate, one can adopt the oxygen transport equation Eq. [14] and the boundary conditions as Eq. [15]. Oxygen diffusivity in liquid electrolytes can be evaluated using a hydrodynamic model, which assumes that the resistance of solute molecule movement arises from the viscous force, similar to the particle movement in viscous fluids. In a dilute liquid, the hydrodynamic approach results in the famous Stokes–Einstein equation as Eq. [16]. Using the Stokes-Einstein equation, the oxygen diffusivity ranges from 10^{-11} to 10^{-8} m^2/s. For general cases, the above problem of oxygen transport is written in the dimensionless form as Eq. [17] and the boundary conditions as Eq. [19]. For β=0, one can solve directly the problem:

$$\bar{C}_{O2} = \frac{\cosh(\sqrt{2Da}\bar{y})}{\cosh(\sqrt{2Da})} \qquad [58]$$

For β=0.5, the problem becomes nonlinear, and can be solved by regular perturbation methods for a small Da:

$$\bar{C}_{O2} = 1 - Da(1 - \bar{y}^2) + O(Da^2) \qquad [59]$$

Combining with Eq. [11], the above will yield the local reaction rate as:

$$j_c = -a i_{0,c}^{ref} C_\infty C_e \exp\left(-\frac{1-\beta}{RT} F\eta\right) \frac{cosh\left(\sqrt{2Da}\bar{y}\right)}{cosh\left(\sqrt{2Da}\right)} \quad for\ \beta = 0$$

$$j_c = -a i_{0,c}^{ref} \sqrt{C_\infty}\sqrt{C_e} \exp\left(-\frac{1-\beta}{RT} F\eta\right) \left[1 - \frac{1}{2}(1-\bar{y}^2)Da\right] \quad for\ \beta = 0.5 \qquad [60]$$

For β =0.5, a Taylor expansion is applied for approximate expression with accuracy $O(Da^2)$. By integrating from 0 to 1, one will obtain the average current density:

$$\mathrm{I} = \int_0^1 j_c d\bar{y} = -a i_{0,c}^{ref} C_\infty C_e \exp\left(-\frac{1-\beta}{RT} F\eta\right) \frac{sinh\left(\sqrt{2Da}\right)}{\sqrt{2Da} cosh\left(\sqrt{2Da}\right)} \quad for\ \beta = 0$$

$$\mathrm{I} = \int_0^1 j_c d\bar{y} = -a i_{0,c}^{ref} \sqrt{C_\infty}\sqrt{C_e} \exp\left(-\frac{1-\beta}{RT} F\eta\right) \left[1 - \frac{1}{3}Da\right] \quad for\ \beta = 0.5 \qquad [61]$$

One can further define a dimensionless reaction current as below:

$$\frac{\delta j_c}{I} = \frac{\delta\sqrt{2Da} cosh\left(\sqrt{2Da}\bar{y}\right)}{sinh\left(\sqrt{2Da}\right)} \quad for\ \beta = 0$$

$$\frac{\delta j_c}{I} = \frac{\delta\left[1 - \frac{1}{2}(1-\bar{y}^2)Da\right]}{1 - \frac{1}{3}Da} \quad for\ \beta = 0.5 \qquad [62]$$

4.4 Morphology of Li Oxides

Figure 29 - Figure 32 present the SEM images of discharge deposit at the three locations of cathode: the layer 1’s surface on the air side, the layer 1-2 interface, and layer 2-3 interface. XRD was performed, showing that the deposit is primarily Li_2CO_3 as observed by our previous study. Figure 30 and Figure 31 show the precipitate at the layer 1 surface, i.e. the cathode surface on the air side. First, it is seen that precipices are present in the pore network of the cathode, as a result of the discharge Li oxides production. The precipitates are also regarded as one major

reason for battery voltage loss in discharge through electrode passivation, surface coverage, and oxygen clogging. The image also clearly shows only a small portion of the pore space is occupied by the precipitates, leaving sufficient space for oxygen diffusion. In addition, precipitate aggregates of a size over a few µm were identified in several locations. It is unclear what mechanism causes the formation of these large aggregates. Aggregates of the dimension were observed in Yang et al. (2014), Zhai et al. (2014) and Wang et al. (2015) as well. In addition, at a few locations precipitates aggregate in form of films covering fibers with grain boundaries on the film surface, as shown in Figure 31. Film formation was observed by Albertus et al. (2011), Viswanathan et al. (2011), Black et al. (2012), Yang et al. (2014), and Yu et al. (2013).

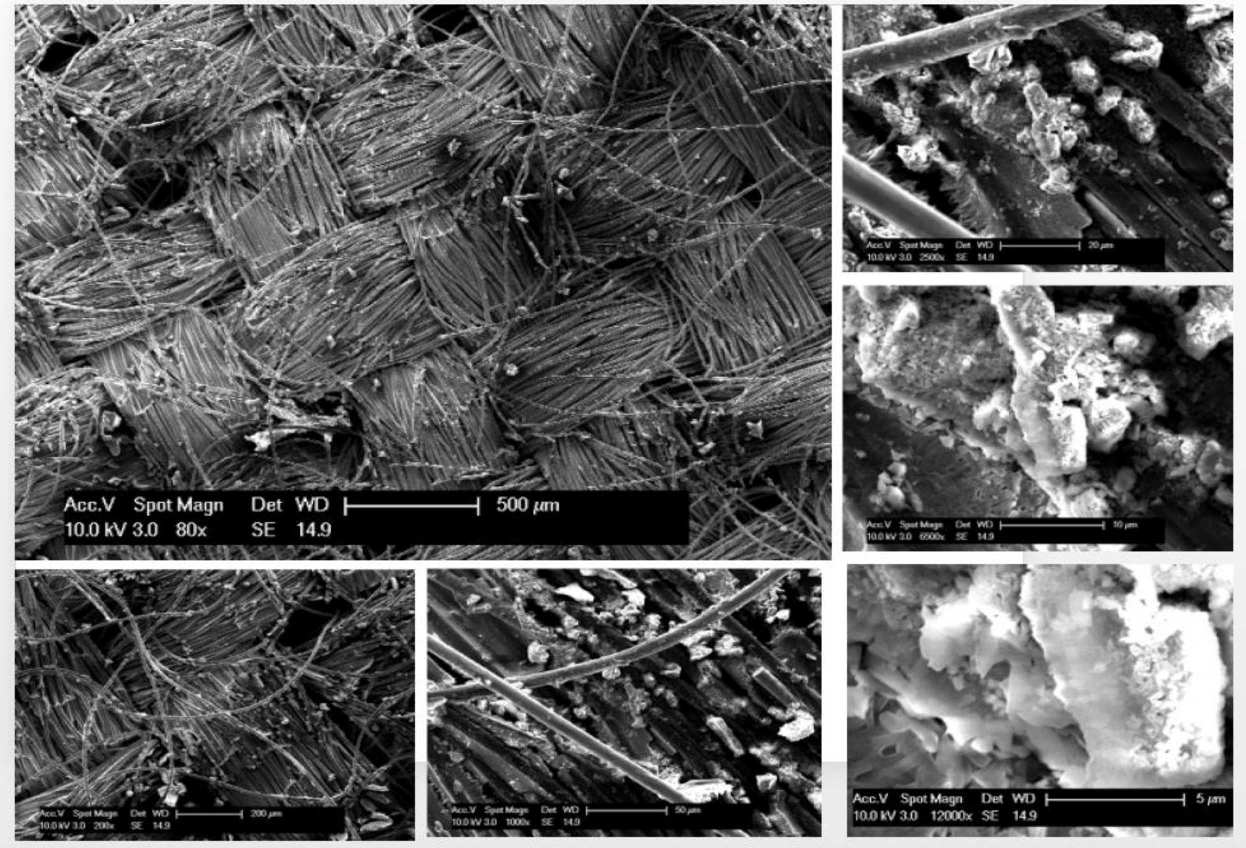

Figure 29: SEM images of precipitates at the layer 1 surface on the air side.

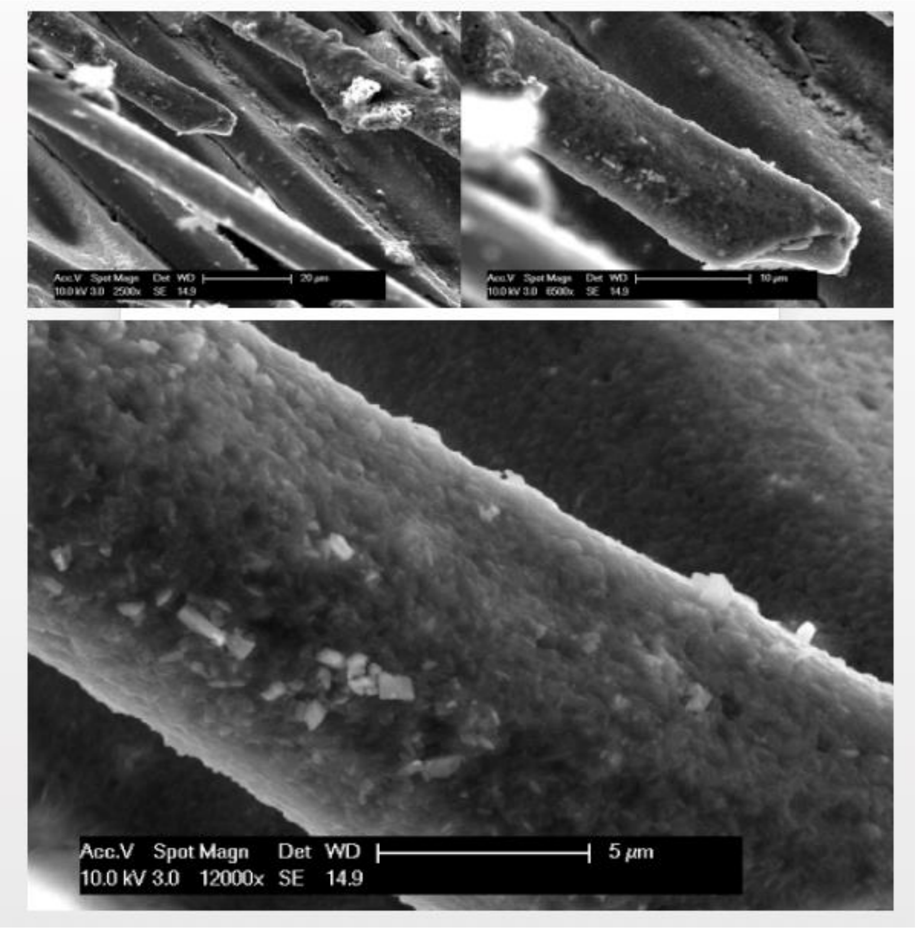

Figure 30: SEM images of the thin film of precipitates at the fiber surface at the layer 1 surface on the air side.

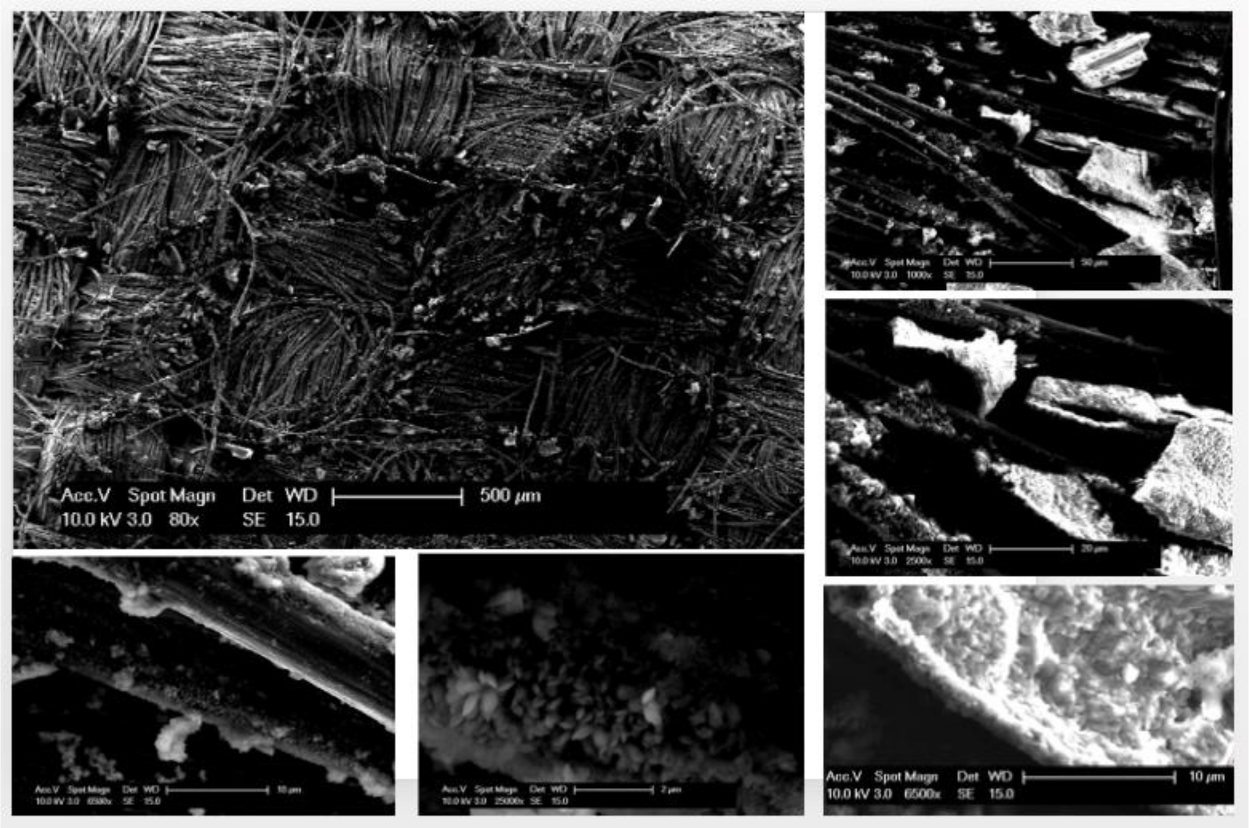

Figure 31: SEM images of the precipitates at the layer 1-2 interface.

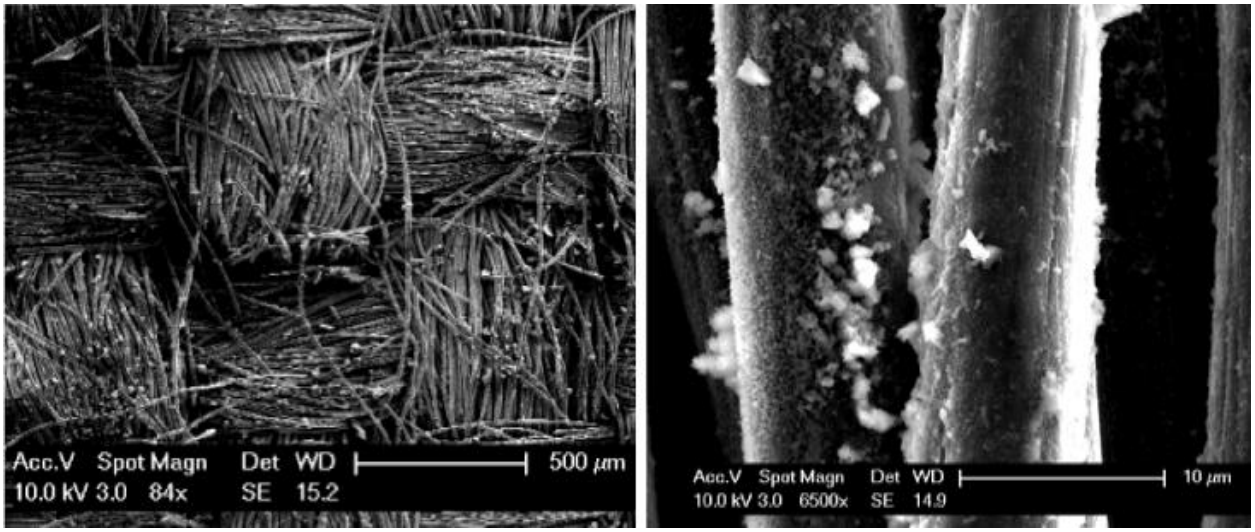

Figure 32: SEM images of the precipitates at the layer 3-separator interface.

Figure 31 shows the cathode at the layer 1-2 interface. Precipitates agglomerate in a few locations as well, consisting of a number of small particles around 200-500 nm in size. In addition, at the surface of fibers in several locations, precipitates in the toroidal or partly toroidal shape around 200-300 nm are also presented. Figure 32 presents the precipitates the layer 3-separator interface, showing that film formation dominates the deposit morphology. The precipitate film attaches the fiber surface without changing the pore space. It is very different with the film at the layer 1 surface, as shown in Figure 31, which is much denser. No aggregates are identified at this location.

4.5 Model Prediction and Experimental Validation

Figure 33 presents the oxygen profiles predicted by Eq. [58] and Eq. [59], assuming the precipitates have negligible impacts on the effective diffusivity of oxygen in the cathode. Similarly, Figure 34 shows the spatial variation of the local reaction rate predicted by Eq.[62]. The SEM images in Figure 29 - Figure 32 show that the precipitates are present in a very small fraction relative to the pore space, thus its effect on hampering oxygen diffusion is small and negligible. It can be seen that the oxygen reduces its content when diffusing into the cathode, as a result of the oxygen consumption by the ORR. The Da number, which evaluates the importance of the reaction rate relative to the oxygen diffusion rate, determines the degree of the oxygen spatial variation. The value of β, the reaction order, measures the dependence of the reaction rate on the oxygen content, thus influences the degree of variation. In addition, both the cathode structure and the type of electrolyte influence the spatial variation through the effective diffusivity.

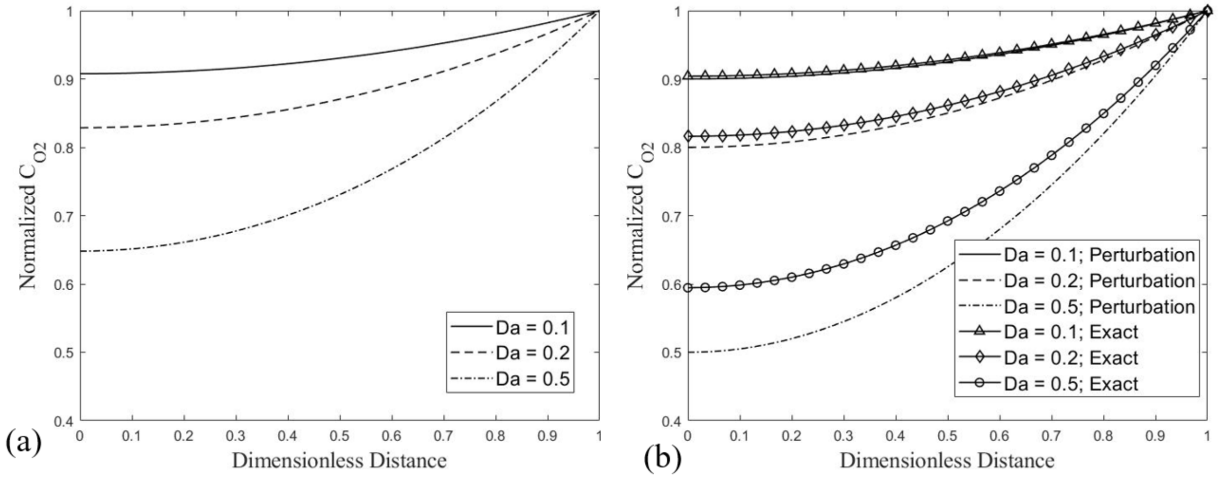

Figure 33: Spatial variation of the oxygen content predicted by Eq. [58] in (a). Compare Eq. [59] with the exact solution.

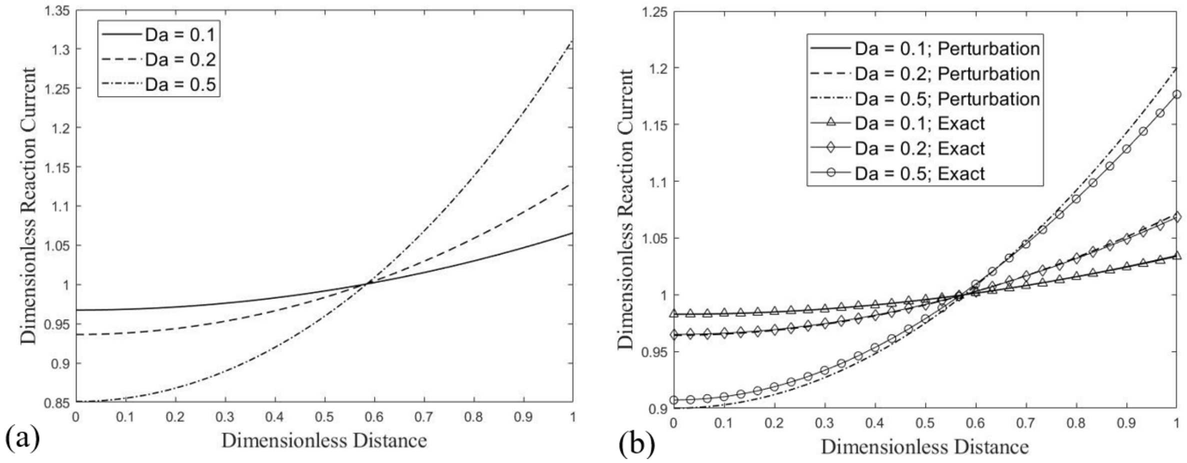

Figure 34: Spatial variation of the local reaction rate predicted by Eq.[62] with β=0 in (a) and β=0.5 in (b). The exact solution is also shown in (b).

Figure 35 presents the spatial variation of the dimensionless reaction rate (or the dimensionless discharge deposit mass scaled by the average mass over the three layers), along with the reaction rate variation predicted by Eq. [60] for β=0. It is shown that the reaction rate decreases when moving from the air side to the separator side, as a result of the decreasing oxygen content. The variation is around 20% between the layer 1 and 3, which is due to the small Da operation in the experiment. The prediction shows an acceptable agreement with the experimental measurement. It is also worth to note that the experimental reaction rate was obtained by averaging the reaction rate within each sublayer over the entire discharge period. Figure 36 presents the comparison with the prediction from Eq. [60], which is obtained for β=0.5. Again, the agreement is acceptable.

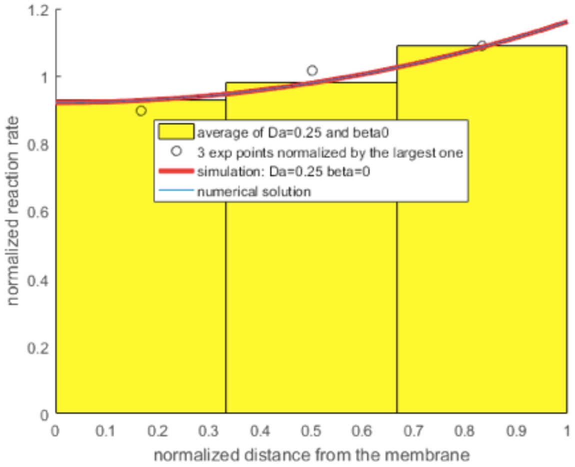

Figure 35: Spatial variation of reaction rate: comparison between experimental data and model prediction for $\beta = 0$.

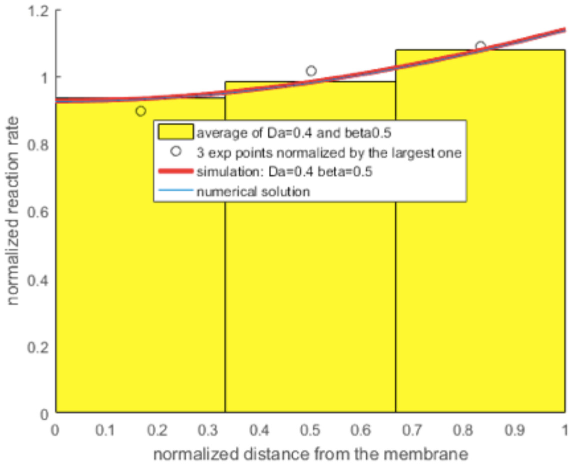

Figure 36: Spatial variation of reaction rate: comparison between experimental data and model prediction for $\beta = 0.5$.

4.6 Summary

In this chapter, the spatial variation of the local ORR reaction rate in the cathode in Li-air batteries was studied both theoretically and experimentally. In experiment, the three-layer cathode was operated till the cut-off voltage, and the morphology and mass were characterized using SEM and a high-resolution scale, respectively. Precipitate morphologies were found to vary at different depth locations of the cathode. Precipitate aggregates were present at both the layer 1 air side surface and the layer 1-2 interface, consisting of small nanoparticles around 200-500 nm. Precipitates in form of thin film were identified at the layer 1 air side surface and the layer 3-separator interface. In addition, precipitates in the toroidal shape attaching carbon fibers were identified at the layer 1-2 interface. In all the locations, the precipitates present a small volume fraction in the pore space, showing a small impact on oxygen clogging. In addition, the mass of discharge precipitates within each layer was measured to obtain the average reaction rate. In the theoretical analysis, the spatial variations of oxygen concentration and ORR rate were obtained for the reaction order of both 0.5 and 1. The solutions showed that the oxygen content decreases from the air side to the separator as a result of the ORR reaction, and the degree of variation is determined by the Da number and reaction order. The spatial variations of the reaction rate predicted from the analytical solutions also agree well with the experimental data.

Chapter 5: Conclusions and Future Works

5.1 Conclusion

In this thesis, a modeling analysis on nonaqueous Li-air batteries was conducted to obtain theoretical solutions for the loss of the output voltage, discharge capacity, and energy capacity caused by insoluble precipitates. Two main voltage losses due to insoluble discharge precipitates, i.e. increased oxygen transport resistance and electrode passivation/surface loss, were distinguished and compared. Approximate solutions were obtained to estimate the discharge voltage, the maximum volume fraction of insoluble precipitates, charge capacity, and energy capacity. Three regimes were defined to identify the dominant mechanisms of the voltage loss. It was found that the approximate solutions of s_{max} are in a close agreement with the numerical solution from iterative methods with errors less than 8% for 2 Regimes. Further, the approximate solutions of energy capacity loss were obtained. The model analyses were extensively validated against experimental data. The developed analytical solutions can be directly applied to optimize electrode design, such as pore structure, porosity, and tortuosity and battery control.

In addition, the predictions of two models, namely the film-resistor model and surface coverage model, were compared with experimental data to study voltage loss and elucidated the precipitate morphology's impacts in Li-air battery discharge operation. Acceptable agreement was achieved for the coverage model, while the film-resistor model failed to match with the experimental data for the two low current densities, i.e. 0.03 and 0.06 mA/cm^2. Several morphologies of discharge deposit were disclosed for the two lower currents, including film formation, large aggregates, small aggregates, and toroidal shapes. The aggregate precipitates were found to be present at a length scale of micrometer and to consist of small nanoparticles around 200-500 nm. Presence of grain boundaries was a possible mechanism for observed aggregation. The impacts of the aggregate and toroidal morphologies on voltage loss deviated from that of film formation, and were attributed as the major reason that the film-resistor model prediction failed to match with the experimental data. For the highest current 0.1 mA/cm^2, thin film formation dominated and the film-resistor model prediction agreed well with the experimental data using the model parameters reported in the literature. The coverage model predicted the experimental data for all the cases because the model accounts for the effects of various morphologies on the electrochemical activity. In addition, it indicated that the voltage loss associated oxygen transport and precipitates was small and negligible in the cases of study.

Furthermore, the spatial variation of the local ORR reaction rate in the cathode in Li-air batteries was studied both theoretically and experimentally. Precipitate morphologies were found to vary at different depth locations of the cathode. Precipitate aggregates were present at both the layer 1 air side surface and the layer 1-2 interface, consisting of small nanoparticles around 200-500 nm. Precipitates in form of thin film were identified at the layer 1 air side surface and the layer 3-separator interface. In addition, precipitates in the toroidal shape attaching carbon fibers were identified at the layer 1-2 interface. In all the locations, the precipitates present a small volume fraction in the pore space, showing a small impact on oxygen clogging. In addition, the mass of discharge precipitates within each layer was measured to obtain the average reaction rate. In the theoretical analysis, the spatial variations of oxygen concentration and ORR rate were obtained for the reaction order of both 0.5 and 1. The solutions showed that the oxygen content decreases from the air side to the separator as a result of the ORR reaction, and the degree of variation is determined by the Da number and reaction order. The spatial variations of the reaction rate predicted from the analytical solutions also agree well with the experimental data.

5.2 Future work

In the experimental, electrolyte evaporation was found to be an issue. It will affect the experiment since it will change the concentration of the electrolyte. And it will also have an influence on the oxygen partial pressure as the experiment goes on. What's more, it is also a safety concern of performing the experimental work. It is important to understand how fast the evaporation goes on will have a damage to the equipment, lead health issue or other safety concerns.

In the current modeling, a simple assumption of the interface between electrode and electrolyte was made, which raises uncertainty in prediction. Solid electrolyte interfaces (SEI) layers are known to form due to side reactions caused mainly by reduction or oxidation of solvents at the surface of anodes and cathodes. Depending on the type of electrode and electrolyte, a composite inorganic-organic SEI layer may exert a more or less protective role on the electrode structure. It can determine the battery cycling and have an effect on capacity fading. To have a better prediction and study, a more accurate SEI model is in need.

In the current work, a 1-D model was employed to simplify the analysis, which is one cause for the difference between the prediction and experimental data. To get a more accurate prediction, a multi-dimensional model is required to take into account all the important processes in the physical dimensions. For example, the cathode usually opens up a few holes for oxygen access, which will lead to a three-dimensional (3D) problem, i.e. a 3D distribution of oxygen concentration will develop in the cathode. The effort in this direction needs numerical implementation of the multi-dimensional model, thus proper numerical methods are important to effective simulation.

BLIOGRAPHY

International Energy Agency, Key World Energy Statistics, https://www.oecd-ilibrary.org/energy/key-world-energy-statistics-2014_key_energ_stat-2014-en, 2014.

X.-P. Gao and H.-X. Yang, 2010, Energy Environ. Sci., 3, 174.

H.-G. Jung, J. Hassoun, J.-B. Park, Y.-K. Sun, B. Scrosati, 2012, Nature Chemistry, 4, 579.

J.-S. Lee, S. T. Kim, R. Cao, N.-S. Choi, M. Liu, K. T. Lee, J. Cho, 2011, Advanced Energy Materials, 1, 34.

G. Girishkumar, B. McCloskey, A. Luntz, S. Swanson, W. Wilcke, 2010, J. Phys. Chem. Lett., 1 (14), 2193.

Z. Wen, C. Shen, Y. Lu, ChemPlusChem, 2015, 80 (2), 270.

S. J. Visco, V. Y. Nimon, A. Petrov, K. Pridatko, N. Goncharenko, E. Nimon, L. D. Jonghe, Y. M. Volfkovich, D. A. Bograchev, 2014, J. Solid State Electrochem, 18, 1443.

Y. Wang and S. C. Cho, 2013, J. Electrochem. Soc. 160 (10), A1847.

H. Yuan and Y. Wang, 2015, Paper No. FUELCELL2015-49434, pp. V001T02A004, ASME 2015 13th International Conference on Fuel Cell Science, Engineering and Technology.

F. Cheng and J. Chen, 2012, Chem Soc Rev., 41 (6), 2172.

X. Liu, B. Cui, S. Liu, Y. Chen, 2015, Journal of Materials Science and Chemical Engineering, 3 (5), 1.

J. Yuan, J.-S. Yu, B. Sunden, 2015, J. Power Sources, 278, 352.

K. Yoo, S. Banerjee, P. Dutta, 2014, J. Power Sources, 258, 340.

V. Viswanathan, K. S. Thygesen, J. S. Hummelshøj, J. K. Nørskov, G. Girishkumar, B. D. McCloskey, A. C. Luntz, 2011, J. Chem. Phys., 135, 214704.

U. Sahapatsombut, H. Cheng, K. Scott, 2014, J. Power Sources, 249, 418.

S. S. Sandhu, J. P. Fellner, G. W. Brutchen, 2007, J. Power Sources, 164, 365.

J. J. Wang, Y. L. Li, X. L. Sun, 2013, Nano Energy, 2, 443.

R. E. Williford and J. G. Zhang, 2009, J. Power Sources, 194, 1164.

Y. Inaguma and M. Nakashima, 2013, J. Power Sources, 228, 250.

F. Ghamouss, M. Mallouki, B. Bertolotti, L. Chikh, C. Vancaeyzeele, S. Alfonsi, O. Fichet, 2012, J. Power Sources, 197, 267.

L. Puech, C. Cantau, P. Vinatier, G. Toussaint, P. Stevens, 2012, J. Power Sources, 214, 330.

X. J. Chen, V. V. Bevara, P. Andrei, M. Hendrickson, E. J. Plichta, J. P. Zheng, 2014, J. Electrochem. Soc., 161, A1877.

J. Christensen, P. Albertus, R. S. Sanchez-Carrera, T. Lohmann, B. Kozinsky, R. Liedtke, J. Ahmed, A. Kojic, 2012, J. Electrochem. Soc., 159, R1.

E. J. Nemanick, 2014, J. Power Sources, 247, 26.

M. Yuasa, T. Matsuyoshi, T. Kida, K. Shimanoe, 2013, J. Power Sources, 242, 216.

P. Andrei, J. P. Zheng, M. Hendrickson, E. J. Plichta, 2010, J. Electrochem. Soc., 157, A1287.

P. G. Bruce, S. A. Frauberger, L. J. Hardwick, J.-M. Tarascon, 2012, Nat. Mater., 11, 19.

K. M. Abraham and Z. Jiang, 1996, J. Electrochem. Soc., 143, 1.

Y. Wang, Z. Wang, H. Yuan, T. Li, 2015, Electrochimica Acta, 180, 382.

Y. Gao, C. Wang, W. Pu, Z. Liu, C. Deng, P. Zhang, Z. Mao, 2012, Int. J. of Hydrogen Energy, 37 (17), 12725.

C. O. Laoire, S. Mukerjee, K. M. Abraham, 2009, J. Phys. Chem. C, 113, 20127.

Y. Li, J. Wang, X. Li, D. Geng, R. Li, X. Sun, 2011, Chem. Comm., 47, 9438.

A. Debart, J. Bao, G. Armstrong, P. G. Bruce, 2007, J. Power Sources, 174,1177.

Y. Lu, Z. Xu, H. A. Gasteiger, S. Chen, K. Hamad-Schifferli, Y. Shao-Horn, 2010, J. Am. Chem. Soc., 132, 12170.

Y. Lu, H. A. Gasteiger, M. C. Parent, V. Chiloyan, Y. Shao-Horn, 2010, Electrochem. Solid-State Lett., 13, A69.

Y.-C. Lu, D. G. Kwabi, K. P. C. Yao, J. R. Harding, J. Zhou, L. Zuin, Y. Shao-Horn, 2011, Energy & Environmental Science, 4, 2999.

M. Mirzaeian and P. J. Hall, 2009, Electrochim. Acta, 54, 7444.

X. Yang, P. He, Y. Xia, 2009, Electrochem. Comm., 11 (6), 1127.

R. R. Mitchell, B. M. Gallant, C. V. Thompson, S. H. Yang, 2011, Energy Environ. Sci., 4, 2952.

L. D. Griffith, A. Sleightholme, J. F. Mansfield, D. J. Siegel, C. W. Monroe, 2015, ACS Appl. Mater. Interfaces, 7 (14), 7670.

J. Xiao, D. Wang, W. Xu, R. E. Williford, J. Liu, J. Zhang, 2010, J. Electrochem. Soc., 157 (4), A487.

S. S. Zhang, D. Foster, J. Read, 2010, J. Power Sources, 195, 1235.

A. A. Franc and K.-H. Xue, 2013, ECS J. Solid State Sci. Technol., 2 (10), M3084.

P. Albertus, G. Girishkumar, B. McCloskey, R. S. Sanchez-Carrera, B. Kozinsky, J. Christensen, A.C. Luntz, 2011, J. Electrochem. Soc., 158, A343.

J. Nanda, H. Bilheux, S. Voisin, G. M. Veith, R. Archibald, L. Walker, S. Allu, N. J. Dudney, S. Pannala, 2012, J. Phys. Chem. C, 116 (15), 8401.

Y. Wang and S. C. Cho, 2015, J. Electrochem. Soc., 162 (1), A114.

Y. Wang, 2012, Electrochimica Acta, 75, 239.

J. Mishler, Y. Wang, P. P. Mukherjee, R. Mukundan, R. L. Borup, 2012, Electrochimica Acta, 65, 127.

Y. Wang, P. P. Mukherjee, J. Mishler, R. Mukundan, R. L. Borup, 2010, Electrochimica Acta 55, 2636.

Y. Wang, 2007, J. Electrochem. Soc., 154, B1041.

C. O'Laoire, S. Mukerjee, K. M. Abraham, E. J. Plichta, M. A. Hendrickson, 2010, J. Phys. Chem. C, 114, 9178.

Y. Wang, K. S. Chen, S. C. Cho, 2013, PEM Fuel Cells: Thermal and Water Management Fundamentals, Momentum Press.

S. S. Zhang and J. Read, 2011, Journal of Power Sources, 196 (5), 2867.

H. A. Every, F. Zhou, M. Forsyth, D. R. MacFarlane, 1998, Electrochimica Acta, 43, 1465.

N. Nithya, S. Selvasekarapandian, P. C. Selvin, D. A. Kumar, J. Kawamura, 2012, Electrochimica Acta, 66 (1), 110.

S. Rajendran, M. Sivakumar, R. Subadevi, 2004, Materials Letters, 58, 641.

K. M. Abraham and S. B. Brummer, 1983, J.P. Gabano (Ed.), Lithium Batteries, Academic Press, New York.

H. J. Rhoo, H. T. Kim, J. K. Park, T. S. Hwang, 1997, Electrochimica Acta, 42 (10), 1571.

S. Rajendran, T. Mahalingam, R. Kannan, 2000, Solid State Ionics, 130, 143.

K. M. Abraham, M. Alamgir, 1990, J. Electrochem. Soc., 137 (5), 1657.

M. Watanabe, M. Kanba, K. Nagaoka, I. Shinohara, 1983, Journal of Polymer Science: Polymer Physics Edition 2, 939.

N. Munichandraiah, G. Sivasankar, L. G. Scanlon, R. A. Marsh, 1998, J. Appl. Polym. Sci., 65 (11), 2191.

W. Xu and C. A. Angell, 2003, Electrochimica Acta 48, 2029.

W. V. Schalkwijk and B. Scrosati, 2002, Advances in Lithium-Ion Batteries.

P. Birke, S. Doring, S. Scharner, W. Weppner, 1996, Ionics, 2, 329.

X. Sun, X. Q. Yang, H. S. Lee, J. McBreen, 1998, Proc. of the 194th Electrochemical Society Meeting, BNL-66142, CONF-981108, Boston.

J. Read, K. Mutolo, M. Ervin, W. Behl, J. Wolfenstine,A. Driedger, D. Foster, 2003, J. Electrochem. Soc., 150, A1351.

X. Z. Wu, T. Morikawa, K. Uchiyama, T. Hobo, 1997, J. Phys. Chem. B, 101, 1520.

S.-Y. Kishioka, 2001, Electroanalysis, 13, 1161.

M. Tsushima, K. Tokuda, T. Ohsaka, 1994, Anal. Chem., 66, 4551.

M. J. Martínez, S. Shimpalee, J. W. V. Zee, 2009, Journal of The Electrochemical Society, 156 (1), B80.

R. Black, S. H. Oh, J.-H. Lee, T. Yim, B. Adams, L. F. Nazar, 2012, J. Am. Chem. Soc., 134, 2902.

Z.-L. Wang, D. Xu, J.-J. Xu, L.-L. Zhang, X.-B. Zhang, 2012, Adv. Funct. Mater., 22, 3699.

W. Fan, Z. Cui, X. Guo, 2013, J. Phys. Chem. C, 117, 2623.

R. R. Mitchell, B. M. Gallant, Y. Shao-Horn, C. V. Thompson, 2013, J. Phys. Chem. Lett., 4, 1060.

B. Horstmann, B. Gallant, R. Mitchell, W. G. Bessler, Y. Shao-Horn, M. Z. Bazant, 2013, J. Phys. Chem. Lett., 4,4217.

E. Yilmaz, C. Yogi, K. Yamanaka, T. Ohta, H. R. Byon, 2013, Nano Lett., 13, 4679.

L. Zhong, R. R. Mitchell, Y. Liu, B. M. Gallant, C. V. Thompson, J. Y. Huang, S. X. Mao, Y. Shao-Horn, 2013, Nano Lett., 13, 2209.

B. M. Gallant, D. G. Kwabi, R. R. Mitchell, J. Zhou, C. V. Thompson, Y. Shao-Horn, 2013, Energy Environ. Sci., 6, 2518.

B. D. Adams, C. Radtke, R. Black, M. L. Trudeau, K. Zaghib, L. F. Nazar, 2013, Energy Environ. Sci., 6, 1772.

C. Xia, M. Waletzko, L. Chen, K. Peppler, P. J. Klar, J. Janek, 2014, ACS Appl. Mater. Interfaces, 6, 12083.

Y. Yang, W. Liu, Y. Wang, X. Wang, L. Xiao, J. Lu, L. Zhuang, 2014, Phys. Chem. Chem. Phys., 16, 20618.

D. Zhai, H.-H. Wang, K. C. Lau, J. Gao, P. C. Redfern, F. Kang, B. Li, E. Indacochea, U. Das, H.-H. Sun, H.-J. Sun, K. Amine, L. A. Curtiss, 2014, J. Phys. Chem. Lett., 5, 2705.

D. Zhai, H.-H. Wang, J. Yang, K. C. Lau, K. Li, K. Amine, L. A. Curtiss, 2013, J. Am. Chem. Soc., 135, 15364.

ELAT Gas Diffusion Layers, Hydrophilic ELAT. http://fuelcellsetc.com/store/DS/ELAT-Property-Sheet.pdf

J. L. Shui, H. H. Wang, D. J. Liu, 2013, 34, 45.

Y. Yu, B. Zhang, Y.-B. He, Z.-D. Huang, S.-W. Oh, J.-K. Kim, 2013, J. Mater. Chem. A, 1, 1163.

L. Johnson, C. Li, Z. Liu, Y. Chen, S. A. Freunberger, P. C. Ashok, B. B. Praveen, K. Dholakia, J.-M. Tarascon, P. G. Bruce, 2014, Nature Chemistry, 6, 1091.

N. Pereira, G. G. Amatucci, M. S. Whittingham, R. Hamlen, 2015, J. Power Sources, 280, 18.

P. G. Bruce, S. A. Freunberger, L. J. Hardwick, J. M. Tarascon, 2012, Nat. Mater., 11, 19.

T. Ogasawara, A. Débart, M. Holzapfel, P. Novák, P. G. Bruce, 2006, J. A. Chem. Soc., 128, 1390.

J. Read, 2002, J. Electrochem. Soc., 149, A1190.

T. Kuboki, T. Okuyama, T. Ohsaki, N. Takami, 2005, J. Power Sources, 146, 766.

H. Cheng and K. Scott, 2010, J. Power Sources, 195, 1370.

Y. Wang and H. Yuan, 2017, J. Electrochem. Soc., 164 (9), A2283.

Y. Wang, K. S. Chen, J. Mishler, S. C. Cho, X. C. Adroher, 2011, Applied Energy, 88, 981.

R. M. LaFollette and D. N. Bennion, 1990, J. Electrochem. Soc., 137, 3701.

C. Y. Wang, W. B. Gu, B. Y. Liaw, 1998, J. Electrochem. Soc., 145, 3407.

B. Tjaden, S. J. Cooper, D. J. Brett, D. Kramer, P. R. Shearing, 2016, Current Opinion in Chemical Engineering, 12, 44.

Y. Wang, C.-Y. Wang, K. S. Chen, 2007, Electrochimica Acta, 52 (12), 3965.

J. Newman and K. E. Thomas-Alyea, 2004, Electrochemical Systems, 3 ed., John Wiley & Sons, New York.

J. Newman and W. Tiedemann, 1975, AIChE J., 21, 25.

X. Ren, S. S. Zhang, D. T. Trana, J. Read, 2011, J. Mater. Chem., 21, 10118.

S. R. Younesi, S. Urbonaite, F. Björefors, K. Edström, 2011, J. Electrochem. Soc., 22, 9835.